Phase Relations in the $YBa_2Cu_3O_{7-x}$ - SiO_2 System and the Impact on Superconducting Fibers

Hanna Verena Heyl

Dissertation submitted to the Faculty of the
Virginia Polytechnic Institute and State University
in partial fulfillment of the requirements for the degree of

Doctor of Philosophy

in

Materials Science and Engineering

Gary R. Pickrell, Chair
David E. Clark
Anbo Wang
Daniel S. Homa

September 4, 2019

Blacksburg, VA

Keywords: $YBa_2Cu_3O_{7-x}$, YBCO-SiO_2 phase relations, ceramic core glass fibers, glass fiber drawing, dissolution of fused silica.

Phase Relations in the $YBa_2Cu_3O_{7-x}$ - SiO_2 System and the Impact on Superconducting Fibers

Hanna Verena Heyl

ABSTRACT

This dissertation presents the first reported identification and analyses of the phase relations in the $YBa_2Cu_3O_{7-x}$ (YBCO)-SiO_2 system at elevated temperatures. In this regard, a rigorous characterization study of the reaction phases within YBCO glass fibers, heat-treated YBCO+SiO_2 pellets, rapid thermally annealed YBCO+SiO_2 rods and rapid thermally annealed YBCO powder inside a fused silica tube is provided. These analyses are based on a vast set of generated novel results obtained using energy dispersive spectroscopy analyses on an environmental scanning electron microscope, X-Ray diffraction analyses, Raman spectroscopy, X-ray photoelectron spectroscopy analyses and a cross-polarized light study.

First, original drawings of YBCO into glass fibers using the molten-core approach on a fiber draw tower in air and oxygen atmospheres are presented and analyzed. The performed analyses reveal the occurrence of reactions between the YBCO core and the silica cladding in as-drawn fibers as well as after additional heat-treatments. A detailed analysis and characterization of the occurring dissolution and diffusion based reaction processes is, then, provided along with the identification of the arising phase separation. Moreover, in order to analyze drawing YBCO glass fibers at lower temperatures, the use of borosilicate as the preform material is also investigated.

This varied set of experiments and associated analyses reveal that the as-drawn YBCO fibers contain an amorphous core and that cuprite (Cu_2O) is the first phase to crystallize out of the amorphous silicate matrix upon heat-treatment. Furthermore, the obtained results demonstrate the dissolution of the fused silica cladding into Si^{4+} and O^{2-} ions and their subsequent diffusion into the molten YBCO core, leading to phase separation due to an occurring miscibility gap in the YBCO-SiO_2 system as well as to silicate formation and amorphization of the YBCO core. This, as a result, prohibits the formation of the superconductive YBCO (Y-123) phase upon annealing. In addition, heat-treatment analyses show that higher temperatures or prolonged dwelling times at lower temperatures lead to the formation of barium copper and yttrium barium silicates. The analysis focusing on the use of borosilicate as the preform material reveals that drawing at lower temperatures reduces the dissolution and diffusion based reactions, but does not prevent them.

Furthermore, the analysis on YBCO glass fibers with a fused silica cladding drawn in oxygen atmosphere shows that a higher oxygen content increases the dissolution of the fused silica cladding into its ions and their subsequent diffusion into the molten YBCO core.

In addition, the performed heat-treatments on YBCO+SiO_2 pellets in air and oxygen atmospheres demonstrate the gradual decomposition of the Y-123 phase with an increase in SiO_2 content. Moreover, the rapid thermal annealing experiments with a subsequent quenching step on YBCO+SiO_2 rods and on YBCO powder inserted inside a fused silica tube show the decomposition of the Y-123 phase and the formation of phases similar to the phases obtained in the YBCO glass fiber study, thus corroborating the results thereof.

In summary, this dissertation enables the determination of the phase relations and reaction processes within the YBCO-SiO_2 system, the identification of the direct effects of the silicon content on the Y-123 phase decomposition, as well as a rigorous characterization of the dissolution and diffusion based reactions within the YBCO-SiO_2 glass-clad fiber system. The generated results and drawn conclusions build a fundamental understanding of phase relations in the YBCO-SiO_2 system, which enables a definite assessment of the feasibility of manufacturing long-scale purely superconductive YBCO glass fibers using the molten-core approach and introduces advanced contributions to general glass-clad fiber systems manufactured using this method.

Phase Relations in the $YBa_2Cu_3O_{7-x}$ - SiO_2 System and the Impact on Superconducting Fibers

Hanna Verena Heyl

General Audience Abstract

This dissertation provides the first reported identification and analysis of the phase relations in the $YBa_2Cu_3O_{7-x}$ (YBCO)-SiO_2 system at high temperatures. In this regard, a thorough characterization study of the reaction phases within YBCO glass fibers drawn using the molten-core approach on a fiber draw tower is provided. In addition, heat-treatment analyses considering YBCO+SiO_2 pellets, rapid thermally annealed YBCO+SiO_2 rods and rapid thermally annealed YBCO powder inside a fused silica tube are performed to gain further fundamental insights. The performed analyses are based on a wide set of characterization methods including energy dispersive spectroscopy on an environmental scanning electron microscope, X-Ray diffraction analyses, Raman spectroscopy, X-ray photoelectron spectroscopy and a cross-polarized light study.

Our experimental results and performed analyses identify the phase relations and reaction processes within the YBCO-SiO_2 system at elevated temperatures, demonstrate the direct effects of the silicon content on the superconductive YBCO phase decomposition, enable drawing definite conclusions regarding the feasibility of manufacturing long-scale purely superconductive YBCO glass fibers using the molten-core approach, and, characterize the dissolution and diffusion based reactions occurring within the YBCO-SiO_2 glass-clad fiber system.

In a nutshell, this dissertation provides a fundamental understanding of phase relations in the YBCO-SiO_2 glass-clad system as well as key insights covering general glass-clad fibers drawn using the molten-core approach, paving the way for improved glass-clad fiber manufacturing using this method.

To my husband, Anibal,
my parents, Klaus and Doreen,
my late grandfather, Willi,
and to the rest of my wonderful family.

Acknowledgments

First and foremost, I am ever grateful to God for his countless blessings during my PhD time.

I would like to thank everyone who helped, supported, and encouraged me during the course of this work. I would like to sincerely thank my PhD advisor, Dr. Gary R. Pickrell, for his continuous support, guidance and motivation during the course of my PhD studies. I would also like to thank my PhD advisory committee members, Dr. David E. Clark, Dr. Anbo Wang and Dr. Daniel S. Homa, for their valuable help and guidance.

I am thankful to all the researchers and colleagues with whom I had the opportunity to collaborate and interact during my PhD studies. I would like to thank, in particular, Shuo Yang and Dr. Carla Slebodnick. I would also like to thank my research group, the Nanoscale Characterization and Fabrication Laboratory team, the Center for Photonic Technology team, as well as Dr. Carlos Suchicital, Kim Grandstaff and the entire MSE department at Virginia Tech for their help and support. My time at Virginia Tech has been truly rewarding and exceptional. I would also like to thank my friends in the US and in Germany for their motivation and encouragement during my PhD journey.

I am deeply blessed and heartily thankful to my husband, Anibal, whose help, support, continuous love, and encouragement made this achievement possible. I thank him for believing in me at every step of the way. I would also like to express my deep gratitude to my beloved parents, Klaus and Doreen. This dissertation would not have been possible without their immense support, motivation, and prayers. I am also greatly thankful to my sister, Karen, her husband, Tobias, and my cute little nephew, Lias, for their boundless love and constant support. My heartfelt thanks go to my beloved grandparents, Opa Kurt, Oma Ilse, Opa Willi and Oma Mechti. I am truly thankful for all they did for me throughout my PhD studies. I am also thankful to my parents-in-law, Jean and Afdokia, and my brother-in-law, Adon, for their continuous encouragement. Last but not least, I would like to thank my entire extended family for their support during my PhD time. I am truly blessed to have such a wonderful and loving family.

Contents

List of Figures

List of Tables

1 INTRODUCTION AND MOTIVATION

Due to the growing need for higher efficiency in electrical applications, various research efforts have focused on proposing new superconductive materials that can achieve such efficiency goals. To this end, a promising material, that has been proposed in the literature, is the high-temperature superconductor $YBa_2Cu_3O_{7-x}$ (YBCO) [1]. YBCO brings forward various advantages to many industrial applications. Indeed, possessing a critical temperature of around T_c=93 K [1], YBCO can be cooled with liquid nitrogen, as opposed to the more expensive liquid helium, making its use in superconductive applications more efficient.

In many industrial applications, such as for power transmission lines and electrical wiring, it is highly advantageous to manufacture superconductors in a wire/tape design. This has led to the introduction of the so-called second generation (2G) high-temperature superconductor wires, which are based on a complex tape structure using YBCO superconductive materials or other rare earth (Re) cuprate superconductors [2, 3]. This complexity introduces efficiency challenges in the manufacturing process, which restricts utilizing such tape structures for mass production and highlights the need for new and more efficient YBCO wire/tape designs.

To this end, this work investigates the reaction mechanisms and phase relations which would be related to manufacturing long-scale glass fibers with a superconductive YBCO core inside a fused silica cladding using a fiber draw tower. Due to its manufacturing efficiency and resulting long-scale fiber lengths, such a design would introduce various advantages in terms of mass production and applicability to various industrial domains.

Previous work by our group [4-7] showed that it is possible to draw superconductive YBCO, bismuth strontium calcium copper oxide (BSCCO) and tin (Sn) powders as well as a lead (Pb) wire into glass fibers using a glass working lathe. These studies proved the possibility of manufacturing glass fibers with a superconductive core. However, the drawn fiber lengths were restricted to a short scale due to the limited working distance of the glass working lathe, as detailed in [4]. Therefore, due to the lack of scalability, fiber manufacturing using the glass working lathe can only be used as a preliminary method of assessing the feasibility of the proposed drawing process. Hence, in order to possibly draw long-scale commercially applicable YBCO fibers, a fiber draw tower must be used. Indeed, this drawing method introduces a number of advantages

in terms of enabling economically efficient long-scale manufacturing of YBCO glass fibers. However, drawing YBCO glass fibers using the molten-core approach on a draw tower also introduces a set of new challenges. During the drawing process at the draw tower, the YBCO powder inside the fused silica preform is exposed to high temperatures over a longer period of time, as compared to the glass working lathe. A longer dwelling time at high temperatures is generally necessary to soften and draw the thicker fused silica preform into a fiber. This leads to the occurrence of dissolution and diffusion based reactions, and upon cooling, thermal stresses between YBCO, the interface layer and silica, which lead to challenges during the drawing process. Hence, analyzing and understanding these reactions is essential for determining the feasibility of drawing long-scale YBCO fibers.

In fact, reactions between YBCO and silica powders [8-12] and YBCO films on silica substrates [13-18] were reported in the literature, considering temperatures of up to 1000°C. However, there is no available work in literature, which studied the reactions within YBCO glass fibers. In addition, to the best of our knowledge, no studies are reported, to this point, in which YBCO and silica are exposed to temperatures above 1000°C. Whereas, the scope of our analyses include temperatures as high as 2000°C, which is the temperature to which the YBCO glass fiber is exposed during the fiber drawing process. Furthermore, as reported in the literature focusing on the molten-core approach [19, 20] for semiconductor core glass-clad fiber manufacturing, silicon was found to be present inside the core [21-23]. In this regard, the works in [21-24] mention possible dissolution and diffusion based processes of the fused silica cladding into the molten core, but do not provide any further insights or in-depth analyses of the reaction processes. Being able to understand and describe thermodynamically and kinetically the reasons for these reactions will enable a deeper understanding and practical improvement in vast areas of glass-clad fiber manufacturing.

This work is the first to provide an in-depth investigation and characterization of the reaction phases of YBCO and silica within a YBCO fiber structure, as well as the first to generally consider YBCO and silica reactions, and phase relations within the YBCO-SiO_2 system, at these elevated temperatures. In addition, this work is the first to perform in-depth analyses of the dissolution and diffusion based reactions inside a YBCO glass-clad system.

To this end, this work showed the feasibility of manufacturing YBCO glass fibers using a fiber draw tower. The fiber draw experiments allowed manufacturing fiber sections with core diameters between 50 to 200 microns and a length of around 1.2 meters using vacuum as well as oxygen atmospheres. In this regard, reactions between the fused silica cladding and the YBCO core were revealed by the fiber drawing process. Therefore, as-drawn fibers as well as fiber sections with additional heat-treatments were characterized using energy dispersive spectroscopy (EDS) analyses on an environmental scanning electron microscope (ESEM), X-Ray Diffraction (XRD) analyses, Raman spectroscopy, as well as using X-ray photoelectron spectroscopy (XPS) analyses and a cross-polarized light study.

The analyses on the as-drawn YBCO fibers provided a vast set of novel results. In this regard, the analyses provided a proof of complete liquefaction of the YBCO core by showing the formation of an amorphous/glassy core in the vacuum as-drawn YBCO fibers. In addition, our work showed that the molten YBCO core leads to the dissolution of the fused silica cladding at the interface region during the drawing process into its ions Si^{4+} and O^{2-} and their subsequent diffusion into the molten YBCO core. XRD analyses, combined with XPS analyses, demonstrated that upon drawing and quenching, amorphous silicate forms inside the core. Furthermore, SEM analyses revealed the occurrence of a phase separation mechanism within the as-drawn YBCO core. In fact, due to this phase separation, silica-rich precipitations were shown to form upon quenching. Indeed, our analyses revealed the formation of an interface layer of silica-rich precipitations, in vacuum drawn fibers, and a formation of silica-rich precipitations in the entire core for oxygen drawn fibers. The generated results have shown that an increase in oxygen content leads to an increase of the overall silicon content inside the core.

In addition, drawing YBCO glass fibers using a borosilicate preform was also investigated to assess the potential effects of the reduced drawing temperature on the reactions within the YBCO-SiO_2 system. In this regard, we have shown that, even though the lower drawing temperature leads to a decrease in the dissolution and diffusion based reactions, it does not lead to their elimination.

Additional heat-treatments on vacuum as-drawn YBCO fibers showed the formation of copper (I) oxide (Cu_2O), which crystallizes at the interface of the silica-rich precipitations and the silicate matrix at around 800°C. Further XRD analyses on the heat-treated as-drawn YBCO glass fibers

showed that the Y-123 phase cannot be restored and that the stable phases, which form at high temperatures or after prolonged heating at lower temperatures, are barium copper silicate and yttrium barium silicate.

In addition, heat-treatments on YBCO+SiO_2 pellets in air and oxygen atmospheres, performed in this work, demonstrated that the superconductive YBCO phase degrades with an increase in SiO_2 content. Furthermore, rapid thermal annealing with a subsequent quenching step on YBCO+SiO_2 rods using the glass working lathe showed the decomposition of the superconductive Y-123 phase and the formation of similar phases as compared to the YBCO glass fiber study. Comparable results were also found for a rapid thermal annealing study on YBCO powder inserted inside a fused silica tube with subsequent quenching to room temperature.

In summary, this work determines the reaction mechanisms and phase relations within the YBCO-SiO_2 system, identifies the effects of the silica content on the superconductive YBCO phase and characterizes the diffusion and dissolution kinetics of the reactions between YBCO and fused silica in the glass-clad fiber system. This understanding is indispensable to the derivation of definite conclusions regarding the feasibility of manufacturing long-scale superconductive YBCO fibers and to building an in-depth understanding of the dissolution and diffusion based processes of fused silica in glass-clad fiber systems manufactured using the molten-core approach.

2 THEORETICAL BACKGROUND

The following chapter introduces the theoretical background and literature review, which is indispensable to the understanding of the key aspects of this work.

2.1 Fundamentals of superconductivity

2.1.1 *History of superconductivity*

Superconductivity was discovered in 1911 by Heike Kamerlingh Onnes by cooling mercury (Hg) to liquid helium temperature. The resistance of mercury dropped suddenly to zero at liquid helium temperature, which later was described as the critical onset temperature, T_c, of mercury. The historic measurement of the resistance versus temperature curve of mercury is shown in Figure 1.

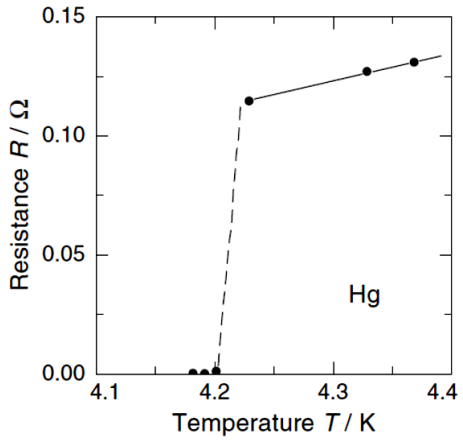

Figure 1: Resistance versus temperature curve of mercury at liquid helium temperature [25]

After this discovery an increasing volume of research was conducted focusing on identifying and developing other superconductive materials with higher critical onset temperatures, T_c. In general, the critical onset temperature of a superconductor describes the temperature below which a superconductor conducts current without any loss. The historical development of superconductors can be seen in Figure 2.

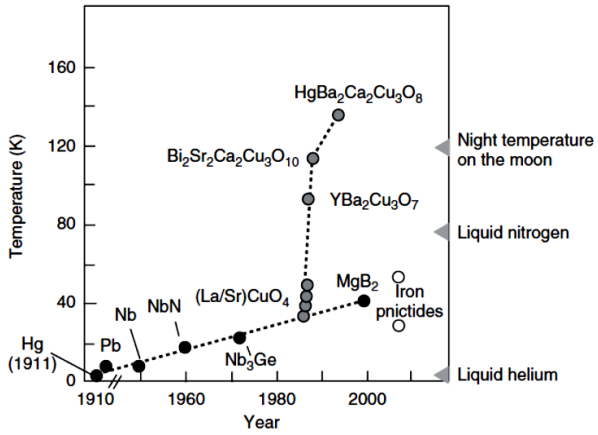

Figure 2: Plot of T_c with respect to the discovered superconductive materials [26]

Figure 2 shows the breakthrough, which was achieved in 1986 by Wu et al. [1], by discovering the high-temperature rare earth cuprate superconductor $YBa_2Cu_3O_{7-x}$ (YBCO). In fact, YBCO has a T_c of 93K, which allows cooling it with liquid nitrogen instead of the more expensive and harder to handle liquid helium. This advancement introduced a major leap forward in the field of superconductivity. The overreaching goal of research on superconductivity remains focused on finding superconductivity at room temperature. However, to this point, no established study has achieved this goal. Furthermore, due to the complex structure of high-temperature superconductors, low temperature superconductors are still used in the majority of superconductor applications.

2.1.2 *Physical properties of superconductors*

The key properties of a superconductor consist of its critical temperature T_c, its critical current density J_c, as well as its coherence length ξ. In general, the coherence length ξ can be described as the characteristic length determining the superconducting properties of a material. Indeed, ξ defines whether a superconductor is a type 1 or type 2 superconductor. In this regard, for type 1 superconductors, ξ is defined as the length of the Cooper pairs, which conduct the supercurrent. However, for type 2 superconductors, ξ is significantly smaller due to its proportionality to $\frac{1}{T_c}$. In its superconductive state, a superconductive material is an ideal conductor and an ideal diamagnet, which can expel an applied magnetic field. This latter effect is known as the Meissner-Ochsenfeld effect [27]. When applying an external magnetic field, this magnetic field can only be expelled up to a certain limit, known as the critical magnetic field B_c.

For type 1 superconductors, the superconductivity is completely destroyed above the critical magnetic field. However, for type 2 superconductors, superconductivity can still co-exist next to a magnetic field, which enters the superconductor above a critical magnetic field B_{c1} in the form of the so-called vortices lines. This is the case due to the small ξ and due to the fact that the supercurrent is so confined that it can still co-exist next to a magnetic field until a critical value B_{c2} is reached. This has made Type 2 superconductors preferred in high magnetic field applications [28]. A detailed explanation of the physical properties of superconductors can be found in the following fundamental works [25, 29, 30].

2.1.3 *State of the art of superconductive wires*

In general, superconductive wires are split in two types: low-temperature superconductive wires, like niobium tin (Nb_3Sn) and high-temperature superconductive wires. High-temperature superconductive wires exist as first generation and second generation superconductive wires. The first generation (1G) high-temperature superconductive wires are based on barium strontium calcium copper oxide (BSCCO) and the second generation (2G) high-temperature superconductive wires are based on YBCO, or other rare earth cuprate superconductors (ReBCO). As mentioned previously, due to the complexity of the cuprate superconductors, low-temperature superconductive wires are still used in applications in which high magnetic fields with high critical current densities are not a necessity.

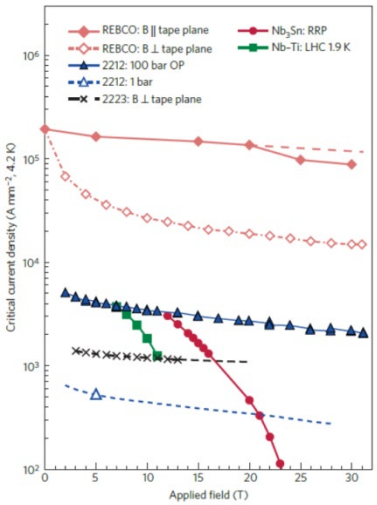

Figure 3: Critical current density with respect to the applied magnetic field for different superconductive materials [31]

Figure 3 shows the variation in the critical current density with respect to the applied magnetic field for different superconductive materials. In this regard, Figure 3 illustrates a main reason as to why 2G superconductive wires, i.e. YBCO (ReBCO)-based superconductors, have increasingly replaced 1G BSCCO (2223)-based superconductive wires. Indeed, this main reason lies in 2G wires' superior performance under high magnetic fields. In addition, 2G superconductive wires exhibit better mechanical properties at lower costs, as compared to 1G wires [32]. 2G high-temperature wires are commercially available. However, even though they are significantly cheaper than 1G wires, they still possess a high cost due to their complex manufacturing process. This, therefore, highlights the need for new methods, which enhance the efficiency of the manufacturing process and make YBCO wires more commercially attractive.

2.2 $YBa_2Cu_3O_{7-x}$

In Section 2.2, the properties and the challenges of YBCO-based superconductive wires are further discussed.

2.2.1 *Physical properties of $YBa_2Cu_3O_{7-x}$*

$YBa_2Cu_3O_{7-x}$ is a high-temperature superconductor with a critical temperature of T_c=93K [1]. YBCO exhibits a polymorphic perovskite crystal structure, which can be seen in Figure 4.

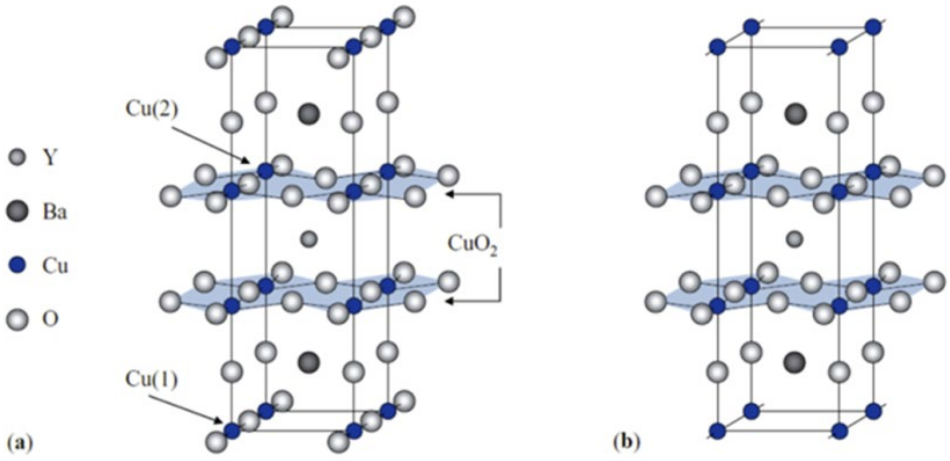

Figure 4: YBCO crystal structure of **a)** the superconductive orthorhombic $YBa_2Cu_3O_7$ and **b)** the non-superconductive tetragonal $YBa_2Cu_3O_6$ crystal structure [25]

Depending on the oxygen content, $YBa_2Cu_3O_{7-x}$ can be a superconductor in its orthorhombic crystal structure or an insulator in its tetragonal crystal structure with an oxygen content lower than around 6.3 ($x \geq 0.7$) [33] as demonstrated in Figure 5.

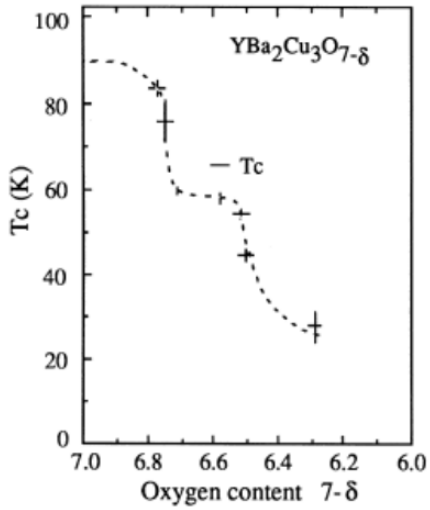

Figure 5: Oxygen doping and its effect on the superconductive properties of YBCO [33]

As can be seen in Figure 5, the critical onset temperature, T_c, of YBCO decreases with a decrease in oxygen content. In addition to the oxygen content, the alignment of the layered YBCO crystal structure is critical for the superconductive properties of YBCO. Due to its layered structure, the physical properties of YBCO are anisotropic. Figure 4 illustrates the copper oxide layers in blue, which are responsible for conducting the supercurrent. Hence, only with a well-aligned structure, YBCO can achieve the highest critical supercurrent throughput. Furthermore, another key property of YBCO is its multifaceted melting behavior. In this regard, a pseudo-binary phase diagram of the YBCO system is shown in Figure 6.

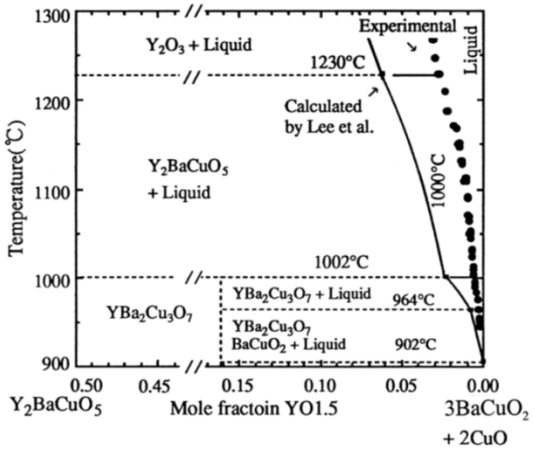

Figure 6: Pseudo binary phase diagram of Y_2O_3-BaO-CuO system at 0.21 atm oxygen pressure [34]

In order to further explain the YBCO phase diagram shown in Figure 6, a detailed description of the different reactions occurring at different temperature are shown in Table 1 [35].

Table 1: Reactions occurring in the YBCO phase system [35], e: eutectics; p: peritectics; m: incongruent melting points

Temperature [°C]	Reaction	Invariant Point
890	$YBa_2Cu_3O_{7-x} + BaCuO_2 + CuO \rightarrow$liquid	e1
920	$BaCuO_2 + CuO \rightarrow$ liquid	e2
940	$YBa_2Cu_3O_{7-x} + CuO \rightarrow Y_2BaCuO_5 +$ liquid	p1
975	$Y_2BaCuO_5 + CuO \rightarrow Y_2Cu_2O_5 +$ liquid	p2
1000	$Y_2BaCuO_5 + BaCuO_2 \rightarrow$ liquid	e3
1000	$YBa_2Cu_3O_{7-x} + BaCuO_2 \rightarrow Y_2BaCuO_5 +$ liquid	p3
1002	**$YBa_2Cu_3O_{7-x} \rightarrow Y_2BaCuO_5$ + liquid**	**m1**
1015	$BaCuO_2 \rightarrow$ liquid ($BaCuO_2$)	m2
1026	$CuO \rightarrow Cu_2O$	
1068	$Y_2BaCuO_5 + Y_2Cu_2O_5 \rightarrow Y_2O_3 +$ liquid	p4
1110	$Y_2Cu_2O_5 + Cu_2O \rightarrow$ liquid	e4
1122	$Y_2Cu_2O_5 \rightarrow Y_2O_3 +$ liquid	m3
1270	**$Y_2BaCuO_5 \rightarrow Y_2O_3$ + liquid**	**m4**
1235	$Cu_2O \rightarrow$ liquid (Cu_2O)	m5
2410	$Y_2O_3 \rightarrow$ liquid (Y_2O_3)	m6

In this respect, the peritectic reaction which transforms the $YBa_2Cu_3O_{7-x}$ (Y-123) phase into its green phase, Y_2BaCuO_5 (Y-211) and a barium- and copper-rich liquid phase is shown in bold. Also shown in bold is the peritectic melting of the Y-211 phase into yttria (Y_2O_3) and a barium- and copper-rich liquid phase. In general, the onset temperature of the peritectic melting decreases with an increase in oxygen deficiency [36, 37]. Due to the barium and copper compounds, YBCO is highly reactive with other materials. In this regard, Section 2.5 will discuss YBCO and its reaction with silica.

2.2.2 *$YBa_2Cu_3O_{7-x}$ in superconductive applications*

As described in Section 2.1.3, YBCO is used in 2G high-temperature wires. Due to its anisotropy, a well aligned YBCO layer is required to achieve high supercurrent throughput [3]. In general, this is achieved by using epitaxial substrate layers, such as a nickel-tungsten (Ni-W) substrate [38]. An image of a 2G high-temperature wire can be seen in Figure 7.

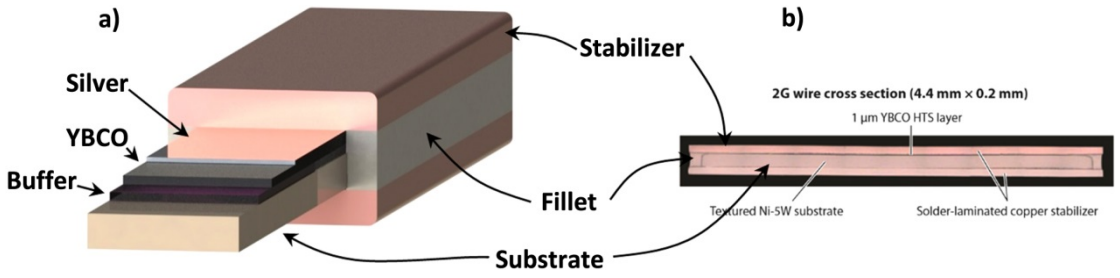

Figure 7: General structure of epitaxial layers in a rolling-assisted biaxially-textured-substrate (RABiTS)-based 2G wire made by American Superconductor Corporation (AMSC) [39]

Figure 7 highlights the complex layer design used in 2G YBCO wires. A buffer layer is used to shield the YBCO layer from possible reactions. Due to the complexity of this design, the manufacturing of high-temperature wires is currently costly and not as efficient as needed to enable a wide commercial acceptance. Moreover, long-scale manufacturing of these tapes is still an issue which also drives the need for more efficient YBCO wire/tape designs.

2.3 SiO_2

Given that one of the main goals of this dissertation is to analyze the reaction mechanisms and phase relations within the YBCO-SiO_2 system, Section 2.3 briefly describes the physical properties of silica as well as the drawing process of glass fibers using the fiber draw tower.

2.3.1 *Physical properties of SiO_2*

Silica (SiO_2) is one of the most abundant oxides on the earth surface [40]. Silica consists of silicon and oxygen covalently bonded to form a tetrahedron. Silica can occur in its amorphous unordered or in its crystalline ordered structure, as can be seen in Figure 8.

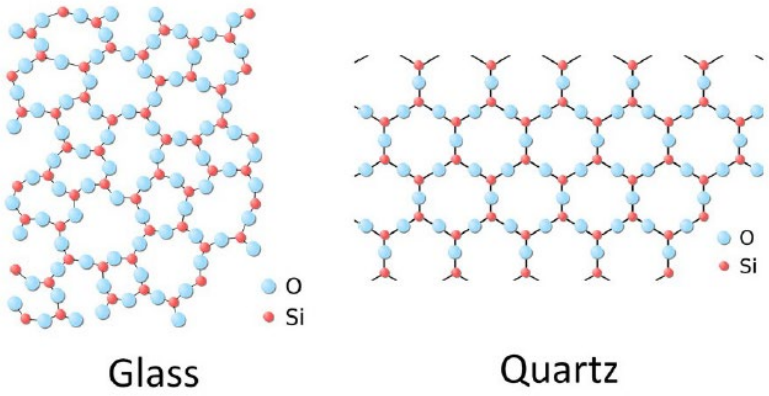

Figure 8: Molecular structure of amorphous (glass) and crystalline (quartz) silica [41]

The amorphous glass used, in general, for tubing and rods is typically referred to as fused silica and fused quartz. In the manufacturing processes of fused silica tubes and rods, there is a typical differentiation in industry between fused quartz and fused silica depending on the manufacturing process. However, throughout this work, to match the nomenclature typically used in academic research, fused silica is used to refer to fused amorphous silica glass irrespective of the underlying manufacturing process.

The crystalline silica structure can occur in seven polymorphs whose occurrences are dependent on pressure and temperature, as is demonstrated in Figure 9.

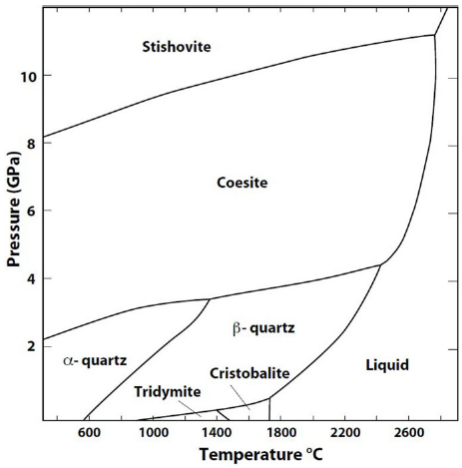

Figure 9: Phase diagram of silica polymorphs [42]

As shown in Figure 9, the thermodynamically stable low temperature phase is α-quartz. Upon annealing at normal pressure, α-quartz transforms into β-quartz, tridymite and cristobalite. In this regard, cristobalite can exhibit two displacive forms. The high temperature phase is known as β-cristobalite and the low temperature form is known as α-cristobalite. Even though cristobalite is the thermodynamically stable phase only at high-temperatures, it can still exist at lower temperatures due to the fact that it would require a reconstructive reforming of the silicon-oxygen bonds to form the quartz structure [43]. In general, cristobalite is also produced during the so-called devitrification of fused silica upon heating above 1100°C for a prolonged time.

In general, silica is widely beneficial for many applications due to its low thermal expansion coefficient, its low thermal conductivity, as well as due to being an electrical insulator. Furthermore, the softening point of fused silica is at around 1683°C. In this respect, fused silica is

used for manufacturing optical fibers by drawing fused silica preforms into a fiber using different drawing techniques. Drawing fused silica glass fibers is discussed next.

2.3.2 *Manufacturing of fused SiO_2 glass fibers*

One way of manufacturing fused SiO_2 glass fibers is using a fiber draw tower, as can be seen in Figure 10.

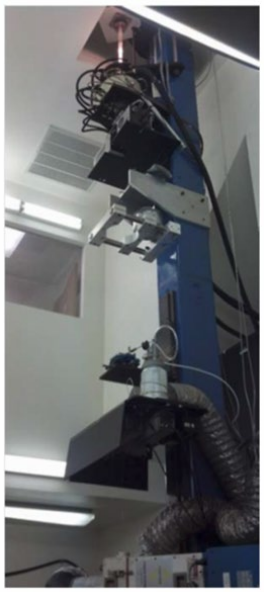

Figure 10: Fiber draw tower at Virginia Tech

Such a fiber draw tower is commercially used to manufacture long-scale optical fibers. A schematic of the drawing process is shown in Figure 11.

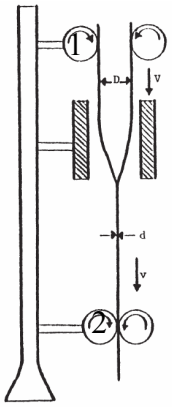

Figure 11: Schematic drawing procedure [44]

Figure 11 shows a glass preform, which is being softened inside the hot-zone of a furnace. Upon reaching the softening point of the glass, the drawing process of the fiber is initiated, which results

in a neck-down profile. In this regard, the feeding speed (1) and the drawing speed (2) in this drawing process are critical parameters.

2.3.3 *Molten-core approach and the presence of silicon inside the core*

The molten-core approach is a common method for manufacturing long lengths of glass-clad fibers, wherein a core material, which cannot be drawn on its own, is molten inside a glass preform which is then softened and drawn into a glass-clad fiber using a fiber draw tower [19, 20]. In this fiber drawing process, depending on the thermal expansion coefficient and melting point of the core material, different glass compositions can be used as cladding materials [45]. For core materials with high melting points, fused silica is typically the preferred cladding material.

In the molten-core approach, high temperatures are required during the drawing process in order to soften the glass. Under these conditions, the low viscosity of the molten core can lead to dissolution and diffusion based processes within the glass-clad molten core system causing degradation in the performance of the drawn fibers [21-24, 46-48]. In one of the first reported dissolution processes occurring during the fiber drawing process involving a silicon core glass fiber [46, 49], oxygen was found inside the core, which led to optical loss. Because of the silicon core, the possibility of dissolution and diffusion of silicon ions from the glass cladding to the core could not be studied. When investigating other semiconductor core materials in glass-clad fiber manufacturing, as in [21-23], both silicon and oxygen were present inside the core. Although the studies in [21-24], reported the dissolution and diffusion based processes of the fused silica cladding into the molten core, in-depth analyses of these processes and of the potentially occurring phase separations were not performed, as discussed in Chapter 1. In general, we have noted that, in all the glass-clad fiber work in which a high silicon content was reported inside the core [21-24, 46-48], glass modifiers were used within the core material. Hence, this is an indication that glass modifiers play a key role in the dissolution and diffusion based processes during the drawing process. As mentioned in Chapter 1, a deeper understanding of these reactions is necessary in order to improve the glass-clad fiber manufacturing.

Moreover, the presence of silica-rich precipitations inside the core of glass-clad fibers is only briefly mentioned in the literature [46]. However, in a recent ongoing work, we observed that using other core material compositions also leads to silica-rich precipitation formation in as-drawn

fibers. Hence, the silica-rich precipitations phenomenon is not solely limited to the YBCO-SiO_2 system. Due to this observation, the formation of silica-rich precipitations in glass systems and in silicon melts is discussed next. A brief overview of the immiscibility theory of liquid-liquid phase separation, which provides background information for Section 2.3.4, can be found in [50].

2.3.4 *Silica-rich precipitations due to phase separation in glass-forming systems*

The formation of silica-rich precipitations are reported in the literature for glass-forming systems with an existing miscibility gap [50]. A brief summary of the results for the BaO-SiO_2 system [51-53] and the Li_2O-SiO_2 system are presented next.

The research presented in [51-53] studied the phase separation mechanism and the resulting morphology in the BaO-SiO_2 system by using bulk glasses [51, 53] as well as vapor deposited thin films [52]. The results reported in [51] on bulk glasses considered silica melts with an addition of 2 to 40 mol-% of BaO. Three different morphologies were observed. Between 2 and 6 mol-% BaO addition, the morphology resulted in round BaO-rich amorphous precipitations inside a silica-rich matrix with a sharp interface region. At a BaO addition of 8 to 12 mol-%, an interconnected structure of the two phases formed. Furthermore, at a BaO content above 18 mol-%, silica-rich amorphous precipitation formed inside a barium-rich matrix with a less sharp interface region. Thus, the difference in the sharpness of the interface region for low and high BaO content is suggested to be due to the higher viscosity of the silica melt. The work in [51] concluded that it is not possible to draw final conclusions regarding the phase separation mechanism solely based on the morphology. The reason lies in the low melt viscosity at high temperatures, which led to a fast phase separation mechanism and to directly interconnected morphologies, which prohibited the analysis of the early stage kinetics. As such, in [51], it was not possible to determine whether the interconnected phase structure originated from weak composition fluctuations (spinodal) or from discrete particles (nucleation and growth). Therefore, studies were conducted on vapor deposited thin films [52] with 0 to 55 mol-% BaO addition and measured in-situ using a transmission electron microscope. The results in [52] confirmed the results of the previous study in [51]. Moreover, the authors in [52] were able to show that for a BaO addition of 12 to 16 mol-%, small discrete particles form inside a silicate matrix during the early stages of phase separation. As such, additional heat-treatments led to the formation of interconnected phases. In addition, it was not possible to study the nucleation and growth process for high BaO contents due to rapid crystallization processes,

which led to the consumption of the phase-separating structures. Figure 12 shows the resulting miscibility gap of the BaO-SiO_2 system obtained in [52].

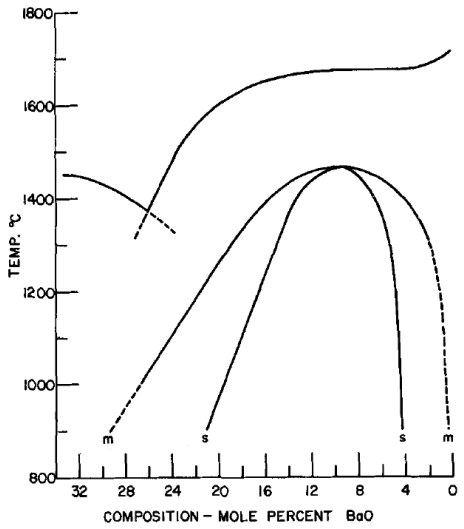

Figure 12: Miscibility gap for the BaO-SiO_2 system [52], m: miscibility gap (binodal curve), s: spinodal curve

By observing the miscibility gap shown in Figure 12, it is reasonable to assume that the nucleation and growth process dominates inside the binodal regions at low as well as high BaO contents. However, the spinodal region is more challenging to predict. In fact, the authors in [52] mentioned that it is important to recognize that cooling from high temperatures into the spinodal region requires cooling through the binodal region (nucleation and growth region) for most instances. Hence, this can be one explanation as to why the glasses inside the spinodal region show a nucleation and growth process in the first stages of the phase separation. The authors in [51, 52] assumed, therefore, that the nucleation and growth process is the dominant process. Such a process was also suggested in [54] for alkali-borosilicate melts and in [50] and the references therein, for liquid-phase separation in glass-forming systems. However, it must be mentioned that the work in [52] was performed by heating from below the glass transition temperature as opposed to cooling from high temperatures above the miscibility gap. In addition, the effect of sample dimensions for thin films versus bulk samples must be analyzed to determine the generality of the determined final kinetic process. In general, determining the phase separation mechanism solely by morphology studies is not sufficient. In fact, one important factor is the thermal history of the glass, which is not always known or hard to obtain.

In addition, the authors in [55] performed a phase separation morphology study on a Li_2O-SiO_2 system. The results showed spherical amorphous silica-rich precipitation inside a silicate matrix, which indicated a nucleation and growth process upon heating. In this respect, the morphology can be seen in Figure 13.

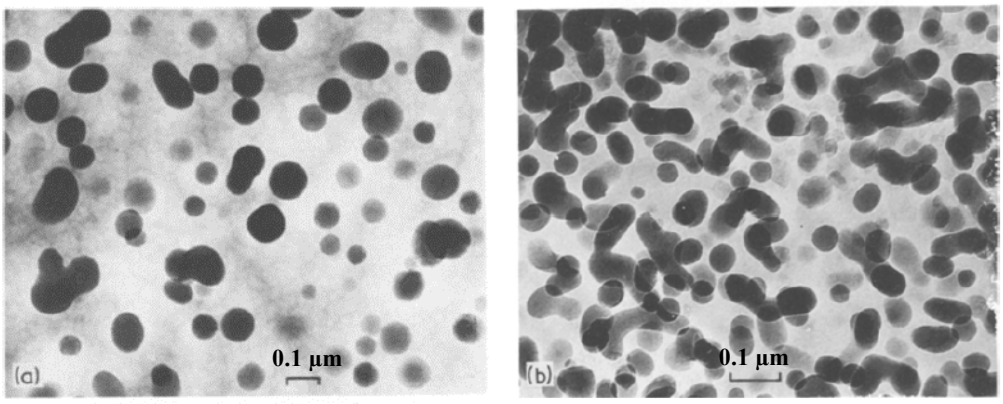

Figure 13: Thin film transmission electron microscope image of **a)** 30 mol-% Li_2O – 70 mol-% SiO_2 glass heat-treated at 550°C for 16h and **b)** 30 mol-% Li_2O – 69 mol-% SiO_2 – 1 mol-% P_2O_5 glass heat-treated at 550°C for 3h [50, 55]

Hence, literature shows that, in general, the formation of silica-rich precipitations can be attributed to a liquid-liquid phase separation mechanism in silicate melts. However, the analysis of the dominant phase separation mechanism (spinodal phase separation versus nucleation and growth) can be difficult to obtain. In this regard, miscibility gaps are mentioned for the CuO-SiO_2 system [56] and the Y_2O_3-SiO_2 [57, 58] system, but no associated in-depth phase and morphology studies were performed in literature. Moreover, no ternary or quaternary phase and morphology studies are reported for the Y_2O_3-BaO-CuO-SiO_2 system.

Furthermore, the formation of silica-rich precipitation is reported in literature also for silicon melts [59-64]. It is described in [59] that depending on the oxygen concentration and the temperature, a solid solution or phase separation into silicon and silica can occur. Furthermore, the solid solubility limit for interstitial oxygen is mentioned as a limiting factor for the precipitation formation. Hence, the formation of the silica-rich precipitations is driven by a nucleation process due to the degree of supersaturation of the solid solution, which is based on the solvent, silicon, and the solute, interstitial oxygen. Furthermore, the work in [55], suggested a nucleation and growth process of these silica-rich precipitations rather than a spinodal phase separation.

After providing a brief overview of the properties of YBCO and silica, Section 2.4 provides preliminary results on drawing superconductive YBCO fibers using a glass working lathe.

2.4 Superconductive $YBa_2Cu_3O_{7-x}$ glass fibers using a glass working lathe

Previous work by our group [4-7] showed that it is possible to draw superconductive materials into glass fibers using a glass working lathe, as described previously in Chapter 1. YBCO glass fibers were produced using a push-pull method in order to reduce the exposure time of YBCO at high temperatures. A detailed description of this method can be found in [65]. In this respect, by using an EDS analysis on a fiber cross-section, the work in [65] showed that a high silicon content is present inside the YBCO glass fiber core. However, it is reported that additional oxygen heat-treatments led to a superconductive core. The work in [65] did not provide an in-depth analysis on the composition of the core and it is, furthermore, not clear whether the EDS analysis was performed before or after the heat-treatment, which makes it difficult to compare the obtained results to our current work.

In this regard, Section 2.5 provides a literature review of relevant works which have focused on the analysis of the reactions between YBCO and silica.

2.5 Reaction of $YBa_2Cu_3O_{7-x}$ and SiO_2

In general, reports in the literature which have studied the reaction between YBCO and silica can be grouped in two categories. In the first category, the studies consider YBCO powder with the addition of SiO_2 powder. The second category of work considers YBCO thin films on silica substrates. A literature review on both categories is performed below while highlighting the aspects and results which are most relevant to the current work.

2.5.1 *Powder studies: Analyses using $YBa_2Cu_3O_{7-x}$ and SiO_2 powders*

The authors in [8] studied a superconductive YBCO powder (Y-123), which was mixed with silica powder in the mol-% of 23.1, 37.5 and 54.5. Each mixture was heat-treated at 950°C in O_2 for 5h. The work showed that when increasing the silica mol-%, the percentage of superconductive Y-123 phase decreases and more secondary phases are formed, as can be seen in Table 2. In this regard, at a silica mol-% of 54.5, the Y-123 superconductive phase was no longer present.

Table 2: Phases found in the YBCO+SiO_2 mixture with different silica mol-% [8]

Silica mol-%	Phases present	T_c
23.1	72% Y-123, 20% Y-211, 8% $Y_2Si_2O_7$	89
37.5	43% Y-123, 28% Y-211, 16% CuO, 13% $Y_2Si_2O_7$	91
54.5	43% Y-211, 32% CuO, 17% $Y_2Si_2O_7$, 8% $Cu_2Y_2O_5$	-

In Table 2, it can be seen that the study in [8] reports Y-211 formation at 950°C. In general, the peritectic melting temperature of Y-123 into the green phase, Y-211, and a liquid phase occurs at around 1015°C [66]. However, it is stated in [9] that silica addition to Y-123 decreases the peritectic temperature of Y-123. Hence, this provides an explanation of the results in [8], summarized in Table 2.

Furthermore, the authors in [10] focused on melt-quenched YBCO powder mixed with silica glass powder in the mole ratio of 1:1 at a temperature of 900°C for 48h in air. The reported reaction product, which was confirmed with XRD, was determined to be Ba_2SiO_4 in addition to the superconductive phase Y-123. The heat-treated powder mixture still exhibited superconductivity with an onset T_c of 90K.

The work in [11] provided similar results as in [10] by studying 80 vol-% Y-123 with 20 vol-% silica powder for a temperature range of 600 to 900°C for 2h. It is reported in [11] that the onset temperature of the Ba_2SiO_4 formation is 800°C.

In addition, a resistance study was performed in [12] on Y-123/silica powder samples which were heat-treated at 1000°C in air for 5h. The authors in [12] reported that, at a ratio of Y, Ba, Cu and Si of 1:2:3:0.6, a zero-resistance was no longer achievable. Hence, this result is an indication of the formation of second phases.

Various other research works [67-70] studied the interaction between Y-123 powder and silica nano-particles and nano-wires to possibly use silica as pinning centers. It was found, in these studies, that silica decreases the grain size of Y-123 and does not affect T_c for a silica addition of up to 0.2 wt-%. However, higher silica amounts led to second phases such as Y-211 and $BaCuO_2$. These works concluded that silica does not have an effect on the superconductive Y-123 phase. However, these results are specific to low wt-% of silica and to silica particles at the nanoscale. Hence, these results cannot be generalized as has been shown in [8-12].

Thus, powder studies showed that an increase in silica content degrades the superconductivity of YBCO. However, different reaction products are reported in distinct studies (as discussed in this section), which can be due to the different atmospheres and heat-treatments used.

2.5.2 *Thin film studies: Analyses using $YBa_2Cu_3O_{7-x}$ film on a SiO_2 substrate*

Studies on thin film YBCO on a Si/SiO_2 substrate are common in literature since Si/silica substrates are widely used in electrical devices.

In [13], the inter-diffusion behavior of a thin YBCO layer onto a silica substrate was studied using Rutherford Backscattering Spectroscopy (RBS). The sample was exposed to a temperature of 600°C for a three hour dwelling time in oxygen atmosphere. The study in [13] stated that molecular silica diffuses inside the YBCO film and copper diffuses inside the silica substrate. However, no further insights were provided. The diffusion coefficient was determined to be $6 \cdot 10^{-19}$ m^2s^{-1} for both processes. The barium diffusion profile is stated to be complicated in its nature.

The work in [14] focused on studying the interaction of a sputtered YBCO film onto a quartz substrate at a temperature range of 603°C to 953°C in oxygen atmosphere. The analysis technique which was used is RBS. The authors in [14] reported copper silicide formation in the interfacial region and, hence, claim silicon diffusion from the quartz to the YBCO layer and copper diffusion from YBCO to the quartz layer with diffusion coefficients of $1.2 \cdot 10^{-10}$ m^2s^{-1} and $8.1 \cdot 10^{-14}$ m^2s^{-1}, respectively. Hence, this work describes a silicon diffusion rather than a molecular silica diffusion process, which was described in [13]. However, the work in [14] presented the results only for a temperature of 953°C and did not consider lower temperature ranges. In addition, the reported copper silicide formation in [14] is unlikely due to the presence of oxides.

Auger electron spectroscopy (AES) and disappearance potential spectroscopy (DAPS) were performed in [15] on a thin film of YBCO with a deposited silica thin film in a temperature range of 70 to 361°C. The authors in [15] observed a decrease in silica features in the AES spectrum and an increase in the barium features in the DAPS spectrum with increasing temperatures. Hence, barium silicate formation is likely. Similar results can be found in [16] and [17], which reported, using AES analysis, a reaction between a YBCO thin film on a silica substrate at 477°C and the formation of Ba_2SiO_4, Y_2O_3 and Cu_2O.

Furthermore, the work in [18] performed rapid thermal annealing experiments, which were conducted on a YBCO film/SiO_2 substrate sample in the temperature range of 800°C to 1000°C. In this work, AES studies and four-point probe resistance tests were performed. The results showed that, only at temperatures between 950°C and 960°C for a dwelling time of 10 to 20s, superconductivity of the YBCO thin film was achieved (zero resistance at 79K). Furthermore, the work in [18] stated that, above 980°C, the YBCO film shows an insulating character and that silicon out-diffusion through the entire film is the major cause of the degradation of the superconductive YBCO phase.

In summary, this review shows that reactions between YBCO and silica are reported in literature. However, this review also emphasizes the complexity of the reaction mechanisms and reveals the necessity of further studying the reaction kinetics and processes to fully understand and characterize these reactions. Moreover, the available works in literature considered the interaction of YBCO and silica only at temperature up to 1000°C. Hence, with regard to the scope of the current work, it is important to investigate higher temperatures to assess the feasibility of drawing YBCO glass fibers.

2.6 Phase relations between $YBa_2Cu_3O_{7-x}$ compounds and silica

The literature survey on the reported reactions between YBCO and silica was introduced in Section 2.5. This section overviews the work in the literature which have focused on phase relations within the YBCO-SiO_2 system.

2.6.1 *Pure YBCO system*

Figure 14 shows a pseudo binary phase diagram, obtained from [71]. This diagram shows the phase transformation of the YBCO system at various temperatures. The corresponding peritectic reactions are shown in Equation 1.

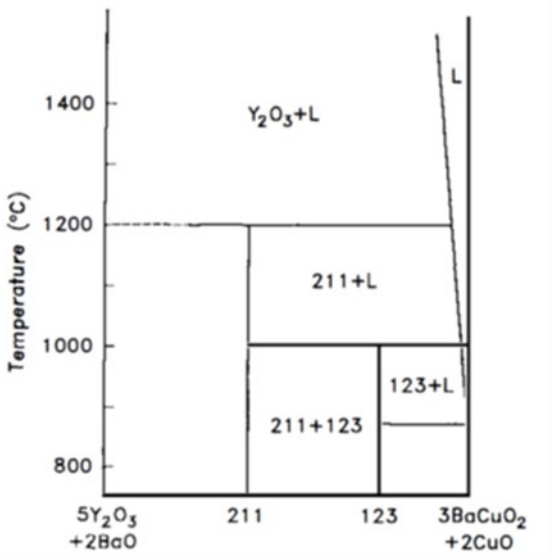

Figure 14: Pseudo-binary phase diagram of YBCO [71]

$$2\ YBa_2Cu_3O_{6.5\ (s)} \xrightarrow{\Delta} Y_2BaCuO_{5\ (s)} + \text{liquid}\ (3\ BaCuO_2 + 2\ CuO) \xrightarrow{\Delta} Y_2O_{3\ (s)} + \text{liquid}\ (4\ BaCuO_2 + 2\ CuO) \qquad (1)$$

In general, no phase equilibrium research is reported in literature, which determines whether the Y_2O_3 phase melts at its actual melting point of around 2425°C or whether it forms lower eutectics in the YBCO system causing a pure liquefaction of the YBCO system at lower temperatures. One potential reason for the lack of phase equilibrium analyses at this temperature range could lie in the high reactivity of YBCO at such high temperatures with all the existing crucible materials.

The highest well-defined temperatures at which quenched YBCO samples were studied can be found in [71, 72]. The reported study in [71, 72] performed a heat-treatment of YBCO powder in a platinum crucible at 1500°C for 20 min dwelling time with a final water quenching step. The results showed that the Y_2O_3 phase is still stable at 1500°C which, however, could be caused by a recrystallization during the quenching process. As a note, the 20 min dwelling time limit was chosen in [71, 72] to prevent complete corrosion of the platinum crucible.

Furthermore, the work in [73] described the melting of YBCO using an oxygen acetylene torch with a subsequent splat-cooling step. In this respect, the obtained product was nearly amorphous with minor microcrystalline phases. However, the superconductive YBCO phase was restored using a subsequent heat-treatment at 920°C for a dwelling time of 4h.

In addition, the work in [74] reported a heat-treatment of YBCO at 1400°C for two hours in a platinum crucible with a final quenching step with different rates. In all quenching steps, Y_2O_3 and $BaCuO_2$ were detected in the as-quenched samples.

The authors in [75] used an H_2/O_2 torch in order to melt YBCO with subsequent cooling rates of 300 Ks^{-1}, 10^4 to 10^6 Ks^{-1}, as well as 10^5 to 10^7 Ks^{-1}. In this regard, XRD analysis showed the formation of $BaCuO_2$ and an undefined cubic phase for the first two cooling rates, whereas the latter cooling rate showed only an undefined cubic phase and an amorphous phase formation.

These studies provide first insights into the complexity of phase formation during quenching processes of pure YBCO at high temperatures. In the majority of these works, it was possible to restore the superconductive Y-123 phase.

With regard to YBCO and silica, only few equilibrium phase relation works are reported in literature [56, 76-80]. The reported results can provide a preliminary understanding of possible phase formations in the YBCO-SiO_2 system. In the following three sections, the different phase relations studied in literature are discussed.

2.6.2 *Y_2O_3 - SiO_2*

The work in [76] reported that Y_2O_3 can form different yttrium silicates with SiO_2. In this respect, the phase diagram of Y_2O_3 and SiO_2 from [76] can be seen in Figure 15.

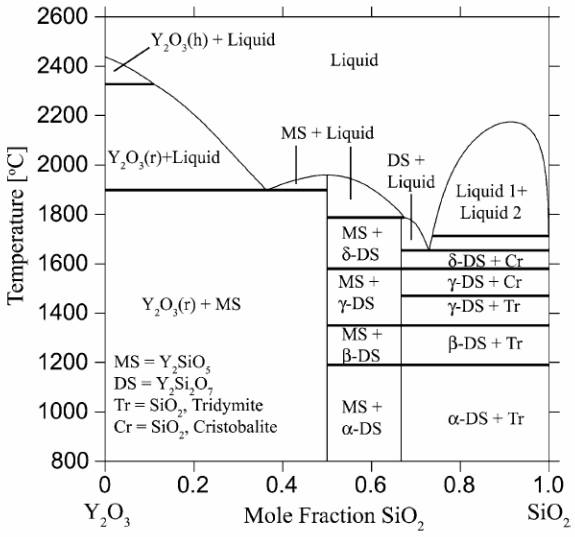

Figure 15: Phase Diagram of Y_2O_3-SiO_2 system [76]

In addition, as can be seen in Figure 15, silica can form lower eutectics with yttria. This aspect is of particular importance to our current work, with regard to the drawing process of YBCO in a fused silica cladding at high temperatures, as this process could lead to the formation of such low eutectics. Furthermore, it is important to note that also cristobalite can be a reaction product in the Y_2O_3-SiO_2 system, which is of relevance to our analysis in Section 3.1.6.

2.6.3 *YBCO compounds - Si/SiO_2*

The authors in [77] investigated the chemical compatibility of yttria, barium oxide, copper oxide and silicon/silica at 800°C. The resulting ternary phase diagrams can be seen in Figure 16. As a note, the question mark in the BaO-$YO_{1.5}$-SiO_2 phase diagram was used in [77] to symbolize that the authors have no data available on phase relations between the three components.

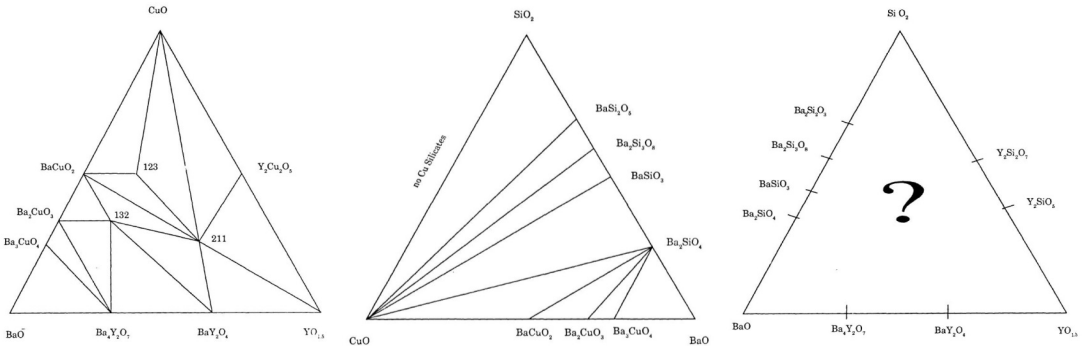

Figure 16: Ternary phase diagrams of CuO, BaO, $YO_{1.5}$ and SiO_2 at 800°C [77]

It can be seen from Figure 16 that CuO co-exists with SiO_2 without any copper silicate formation at 800°C. Similar results were found in [78] by studying the Cu-O-SiO_2 system at temperatures between 1180°C and 1500°C. However, another study [79] showed that CuO can react with silica in the presence of yttria to form a yttrium copper silicate at 1000°C, as can be seen in Figure 17.

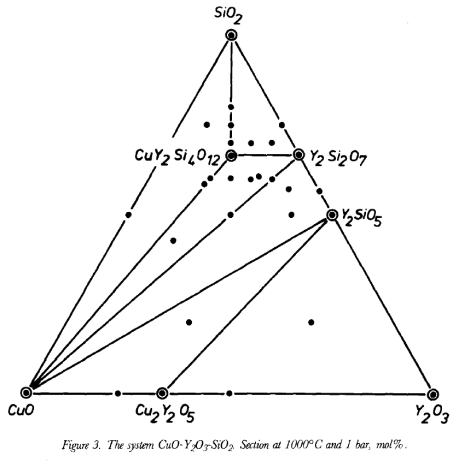

Figure 17: Ternary phase diagrams of CuO, Y_2O_3 and SiO_2 at 1000°C [79]

2.6.4 *CuO - Cu_2O - SiO_2*

The work in [56] studied and reviewed works on the CuO-Cu_2O-SiO_2 system. These reported studies did not find any formation of silicates or solid solutions. In addition, the work in [56] showed a binary phase diagram of Cu_2O and SiO_2 which can be seen in Figure 18.

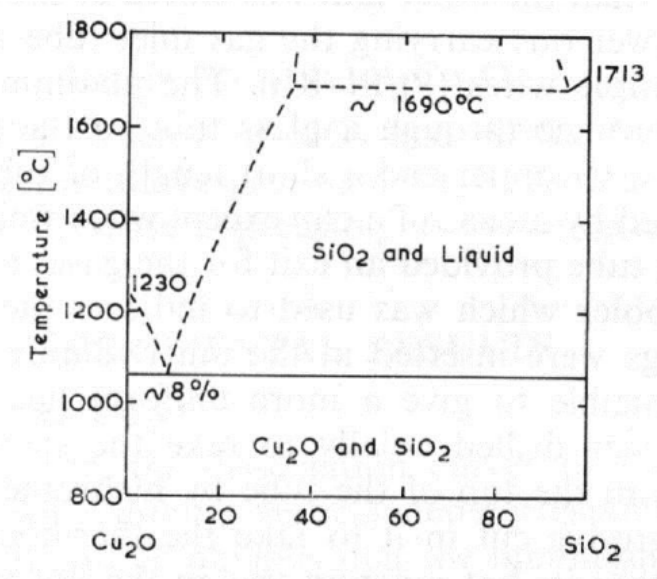

Figure 18: Binary phase diagram of Cu_2O and SiO_2 [56]

3 EXPERIMENTAL RESULTS AND ANALYSES

After introducing the needed background information and surveying the relevant literature, this chapter presents the experimental results and associated analyses, which constitute the core of this work.

3.1 $YBa_2Cu_3O_{7-x}$ glass fibers

3.1.1 *Objective and drawing procedure*

The objective of this work is to analyze the reactions within YBCO glass fibers in order to assess the feasibility of obtaining long-scale superconductive YBCO glass fibers using a fiber draw tower. As part of this analysis, various YBCO fiber draws were performed, in different atmospheres and with different glass compositions and were subsequently studied.

In the performed drawing processes, different sized fused silica tubes from Technical Glass Products, Inc. were used for manufacturing the fused silica preforms. The fused silica tubes were over-clad with successively larger tubes to produce a thick walled glass preform by using a glass working lathe, Litton Model HSJ143. Several preforms were prepared and tested. The final preforms' outer diameter (OD) varied from 10 to 25 mm and the inner diameter (ID) varied between 1 and 3 mm. Furthermore, different tapering techniques were used to reduce the ID so that only a small quantity of YBCO powder is exposed to the high temperatures at the hot-zone of the furnace while softening the preform. Afterwards, the obtained fused silica preforms were filled with a commercially available superconductive orthorhombic YBCO (Y-123) powder (99.99% purity) with a particle size of 2-6 μm, which was purchased from SSC Inc. and from SCI Engineered Materials. A tapered preform design can be seen in Figure 19.

Figure 19: Tapered preform with YBCO powder

After the filling process, the YBCO preform was subsequently drawn into YBCO core glass fibers on the fiber draw tower, which is equipped with a graphite furnace, using the drawing techniques described in [19, 20]. The furnace was steadily heated up to temperatures around 2000°C to soften

the fused silica. This softening process required a time period of around 30 minutes, during which the YBCO powder that is closest to the hot-zone was exposed to the highest temperatures. In order to determine the effect of the oxygen partial pressure on the drawing ability of YBCO glass fibers, draws were performed in vacuum as well as in oxygen atmosphere. In addition, YBCO glass fibers were also drawn using a borosilicate preform manufactured using Corning Pyrex code 7740 glass tubing with a chemical glass composition of 80.6 % SiO_2, 13.0% B_2O_3, 4.0% Na_2O, 2.3 % Al_2O_3 and miscellaneous traces of 0.1 %. The drawing of YBCO glass fibers using a borosilicate preform was performed in order to investigate the effect of the drawing temperature on the reaction of YBCO and silica. As a note, borosilicate glass has a reduced softening point of around 821°C as compared to the softening point of fused silica, which is 1683°C. Due to the low softening point of borosilicate glass, 15 wt.-% silver (I) oxide (Ag_2O), purchased from Alfa Aesar, was added to the YBCO powder to reduce the peritectic melting temperature of YBCO. Reducing the peritectic melting temperature of YBCO by the addition of Ag_2O is reported in [81, 82]. In this regard, the literature states that the addition of a maximum of 20-vol% to 30-vol% of Ag enhances the current density, hardness, Young's modulus and flexural strength [81, 83] of YBCO and can be, therefore, of advantage to our drawing process.

Moreover, different core designs were tested in order to investigate the possibility of mitigating the reaction between YBCO and silica during the drawing process. Three different core designs, in which fused silica is used as the preform material, can be seen in Figure 20.

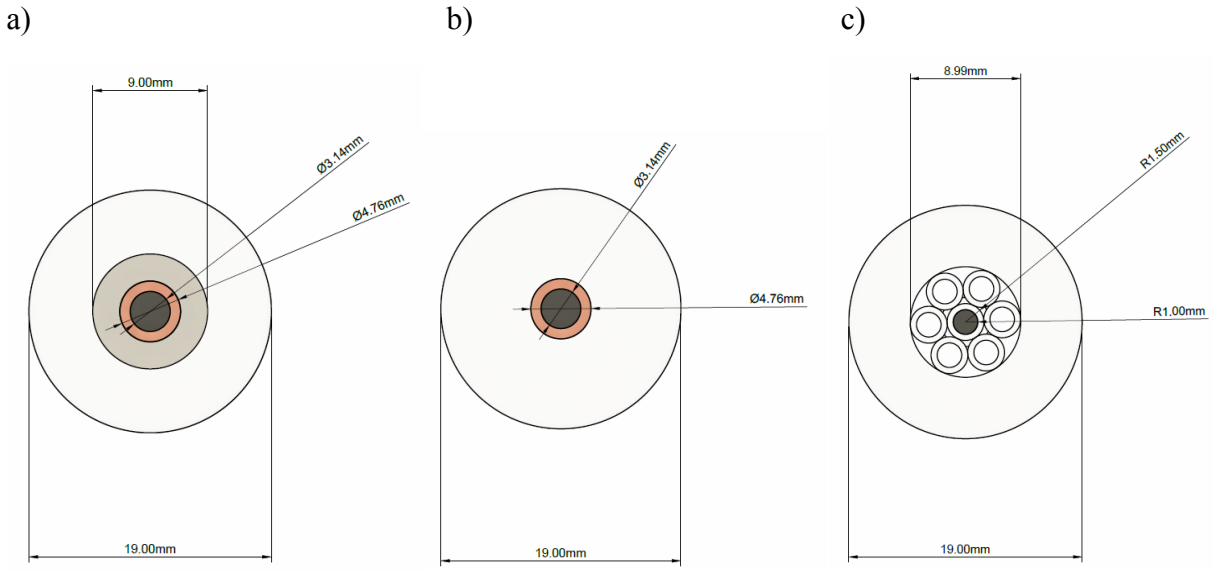

Figure 20: a) Barium silicate (light grey) /Copper (brownish) /YBCO (dark grey) core preform with fused silica cladding, **b)** Copper (brownish) /YBCO (dark grey) core preform with fused silica cladding and **c)** Stacked hollow fused silica preform design with YBCO core (shown in dark grey)

Following the drawing process, cross-sections of as-drawn fiber sections were polished down to 0.1 µm, using successively finer diamond lapping films and characterized with an environmental scanning electron microscope, FEI Quanta 600 FEG. Energy dispersive spectroscopy for chemical composition point analysis, line-scan (with 2 µm increments) and mapping were performed with an attached Bruker QUANTAX 400 Energy Dispersive X-Ray Spectrometer with a high speed Silicon Drifted Detector, at accelerating voltages of 10.0 kV and 20.0 kV. Moreover, XRD analyses were performed on YBCO core fragments using a single-crystal X-ray diffractometer, Rigaku XtaLAB Synergy-S, operating in Debye Scherrer geometry using Cu-K_α radiation and equipped with a HyPix-6000HE area detector. Sample preparation consisted of embedding fiber fragments in Paratone oil and then shattering the fiber to allow for retrieval of glass-free core fragments of dimensions 20-100 µm. Each fragment was analyzed by mounting it on a Nylon loop and collecting a series of 360º phi-scans over a period of 27 minutes. The program CrysAlisPro [84] was used for data collection and to extract the powder pattern from the raw images. The XRD software HighScore Plus was used for data analysis and phase identification. Raman spectroscopy analyses were performed on selected YBCO cores using an unpolarized confocal Raman microscope (WITec alpha-300-SR). The Raman measurements were performed on polished fiber cross-sections using a continuous wavelength laser beam of 532 nm focused with a 50× objective to a spot size of ~2.5 µm. The reflected light was filtered by a long-pass filter (cut-off: 535 nm)

before entering the electron-multiplying CCD spectroscopy detector, Andor Newton DU970. The exposure time was 1 second. In addition, vacuum as-drawn YBCO fused silica fiber sections were characterized using X-ray photoelectron spectroscopy, PHI Quantera SXM.

Furthermore, additional heat-treatments were conducted on vacuum as-drawn YBCO fiber sections in air at 800°C to 1200°C with heating and cooling rates of 5°Cmin^{-1} and a dwelling time of 10 min using a standard tube furnace, MTI Corporation Model GSL-1100X, and a muffle furnace, Barnstead Type 1500, for the 1200°C heat-treatment. In addition, vacuum as-drawn YBCO fiber sections were heat-treated in flowing oxygen, using a rate of 0.4 SLmin^{-1}, at 950°C for dwelling times of 12 and 48 hours with a subsequent dwelling time of 12 hours at 500°C and an overall cooling rate of 1°Cmin^{-1} using the standard tube furnace, MTI Corporation Model GSL-1100X. The heat-treated fiber cross-sections were also studied using ESEM, X-ray diffraction, Raman spectroscopy analyses as well as under cross-polarized light using an optical microscope, Olympus BX51. These additional heat-treatments were performed to further analyze the reactions between the YBCO core and the silica cladding and to possibly restore the superconductive YBCO phase.

3.1.2 *Results and characterization of as-drawn YBCO fused silica glass fibers in vacuum atmosphere*

Using the described drawing method in Section 3.1.1, continuous round-shaped and dense YBCO core fiber sections were successfully drawn, as can be seen in the backscattered-electron (BSE)-image of a vacuum as-drawn YBCO fused silica fiber section in Figure 21, with a length of up to 1.2 meters as shown in Figure 22.

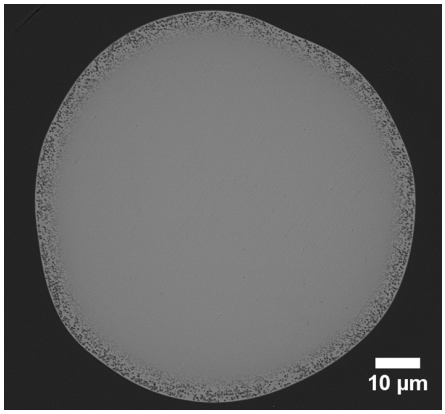

Figure 21: BSE image of the YBCO core (light grey) of a vaccum as-drawn fiber cross-section surrounded by the fused silica cladding (dark grey)

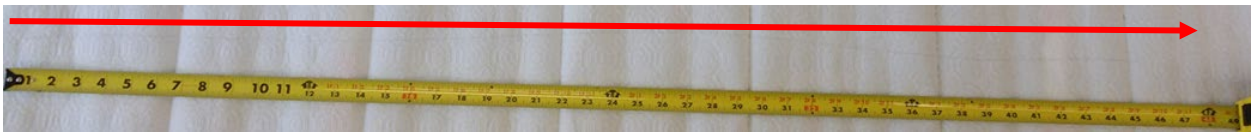

Figure 22: YBCO glass fiber section

The length of the fiber sections is limited by a number of challenges encountered during the drawing process, due primarily to reactions occurring between YBCO and silica as well as due to thermal stresses (caused by the large difference in the thermal expansion coefficient between YBCO and silica) and pressure build up inside the preform, which leads to so-called blow-outs (breakage of the glass). The pressure build up is due to gas formation of barium and copper vapors, which have their boiling point close to 2000°C. Figure 23 demonstrates the end of a YBCO preform after a blow-out occurred. Noticeable in Figure 23 is the color change, which is also an indication of copper vapor formation.

Figure 23: YBCO preform after a blow-out

Throughout this work, we were able to reduce these blow-outs by drying the YBCO powder at 900°C for 4 hours in oxygen atmosphere, directly before the draw, as well as by increasing the thickness of the preform walls. Using these two approaches, we were able to mitigate the blow-outs and reduce breakage of the fibers.

In order to characterize and further understand the occurring reactions between YBCO and silica, in-depth analyses on the as-drawn fibers were performed. In this regard, EDS analyses were performed to primarily study the YBCO core. The obtained EDS data, for the center of the core, is shown in Table 3.

Table 3: EDS point analysis on the center of a vacuum as-drawn YBCO core shown in atomic percent [at.-%]

Y	Ba	Cu	O	Si
3.3	5.5	9.3	62.7	19.2

The EDS data in Table 3 shows that, in addition to yttrium, barium, copper and oxygen, silicon is also present inside the core with a relatively high atomic percentage.

To further investigate the presence of silicon in the core, the cladding and core region were studied using higher magnification BSE imaging, as shown in Figure 24.

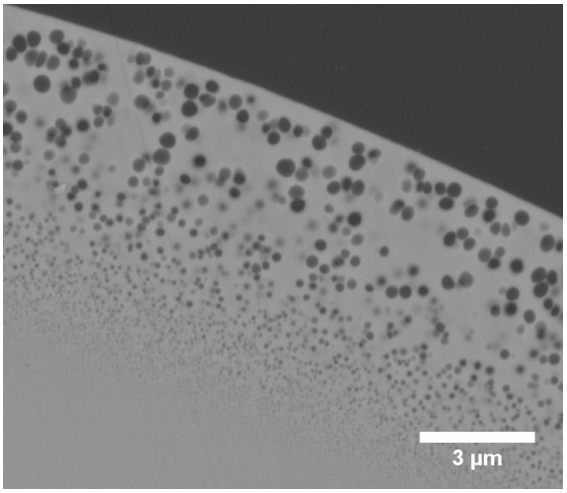

Figure 24: BSE image of the interface layer between the YBCO core (light grey) and the silica cladding (dark grey) of an as-drawn vacuum YBCO fiber cross-section

Figure 24 shows the presence of an interface layer between the cladding and the core region. This interface layer is shown in Figure 24 to contain round precipitations which decrease in size towards the center of the core.

To investigate the nature of these precipitations, EDS point analyses were performed, which demonstrate that the precipitations are rich in silicon and oxygen with a 1:2 ratio, as can be seen in Table 4.

Table 4: EDS point analysis on a dark precipitation at the interface layer in a vacuum as-drawn YBCO fiber section shown in atomic percent [at.-%]

Y	Ba	Cu	O	Si
1.1	2.2	3.6	62.1	31.0

Table 4 also shows low percentages of yttrium, barium and copper. However, this is due to the large excitation volume of the X-rays (around 2 µm), which leads to a composition overlap resulting from measuring not solely the composition of the dark precipitations but also the composition of the adjacent core matrix. The EDS point analyses results in Table 4 indicate the presence of pure silica in the formed interface layer. In addition, a further EDS line-scan across the core-cladding region of the as-drawn YBCO fiber showed that the silicon content decreases in the interface region towards the center of the YBCO core as can be seen in Figure 25. The EDS line-scan shown in Figure 25 starts in the fused silica cladding at the expected Si:O (1:2) ratio, with no Y, Ba, or Cu presence. The cladding-core interface starts at ~12 µm. Between ~12 - 20 µm, the silicon and oxygen content gradually decreases, with concomitant increase in the Y, Ba, and Cu content until the composition flattens and remains steady across the core region until the same concentration gradients are again observed at the opposite core/cladding interface.

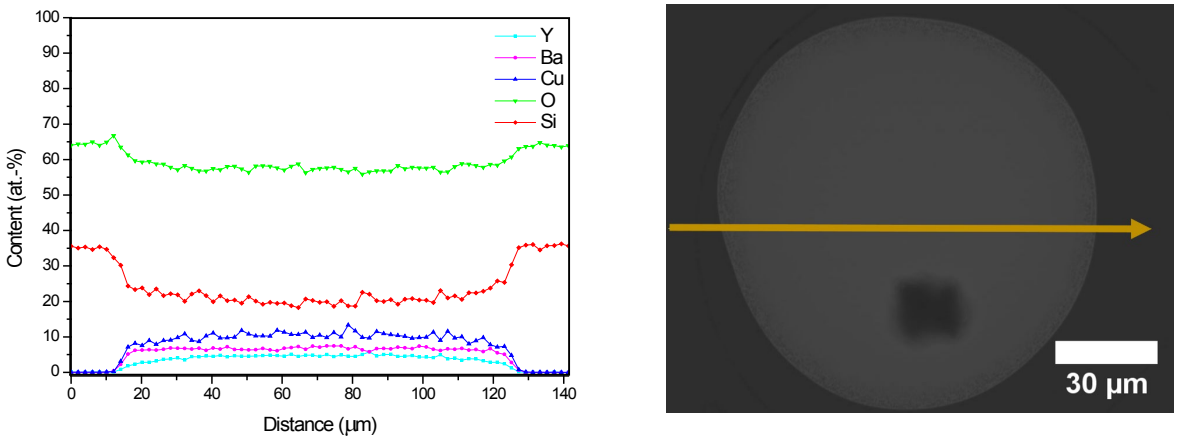

Figure 25: EDS line-scan across the core-cladding region of the vacuum as-drawn YBCO glass fiber with a core diameter of 115 µm

This indicates the occurrence of silicon (Si^{4+}) diffusion from the silica cladding into the interface region within the YBCO core. In fact, previous analyses [14-18] reported the diffusion of silicon ions from a silica substrate into a YBCO layer. The steady silicon concentration in the core can be attributed to a restricted oxygen diffusion, allowing for Si^{4+} to build up and limiting further Si^{4+} ion diffusion.

Moreover, EDS line-scans taken from a larger YBCO glass fiber diameter core (237 µm) and a smaller diameter core (15 µm) are shown in Figure 26 and Figure 27, respectively.

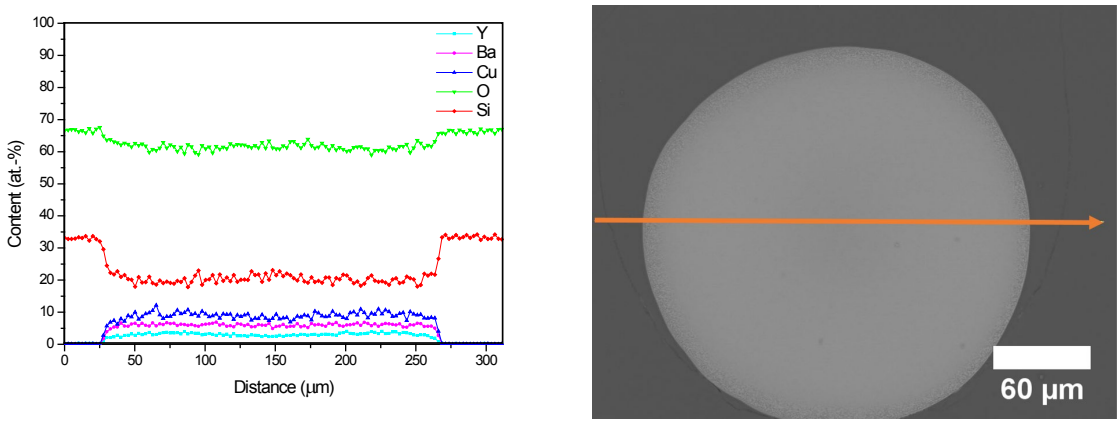

Figure 26: EDS line-scan across the core-cladding region of a vacuum as-drawn YBCO glass fiber with a core diameter of 237 µm

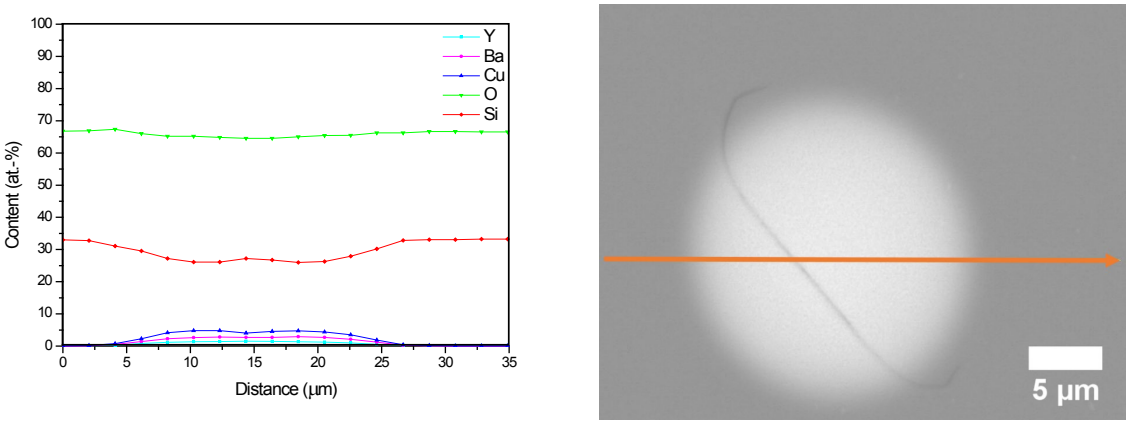

Figure 27: EDS line-scan across the core-cladding region of a vacuum as-drawn cane YBCO glass fiber with a core diameter of 15 µm

Table 5 shows the average silicon content inside the core for the three different core diameters.

Table 5: Dependence of the silicon content inside the core on the diameter of the vacuum as-drawn YBCO core

Diameter of YBCO core	Average silicon content inside the core [at.-%]
15 µm	27.6 ± 2.1
115 µm	20.6 ± 1.3
237 µm	20.2 ± 1.2

The results in Table 5 show that for a larger core diameter of 115 µm and 237 µm, the steady concentration profile of the silicon content inside the core is ~20 at.-%. In addition, both the EDS line-scans in Figure 25 and Figure 26 present a significant diffusion-based concentration gradient at the interface region between the cladding and the core. For the smaller core diameter of 15 µm, the EDS line-scan in Figure 27 shows only a minor concentration gradient at the interface region

with a much higher silicon content of 27.6 ± 1.2 at.-% compared to the larger core diameter fibers. This indicates that a solubility limit of the silicon ion diffusion inside the molten YBCO core exists. The higher silicon and oxygen contents of the smaller diameter core further corroborate the role of the restricted oxygen diffusion in limiting the diffusion of Si^{4+} ions. Moreover, Table 5 and the EDS line-scans shown in Figure 25, Figure 26 and Figure 27 demonstrate that the reactions occurring between the fused silica cladding and the YBCO core are diffusion-controlled.

To further study the silicon content inside the core of the as-drawn YBCO glass fibers, XPS analyses were performed on as-drawn YBCO fiber sections. For these XPS studies, overview spectra of the cladding and the core were measured with a spot size of 50 µm. In addition, the fiber cross-section was sputtered layer by layer (~100nm) to remove any surface contaminations.

The XPS spectrum of the core and the cladding after sputtering can be seen in Figure 28 and Figure 29, respectively.

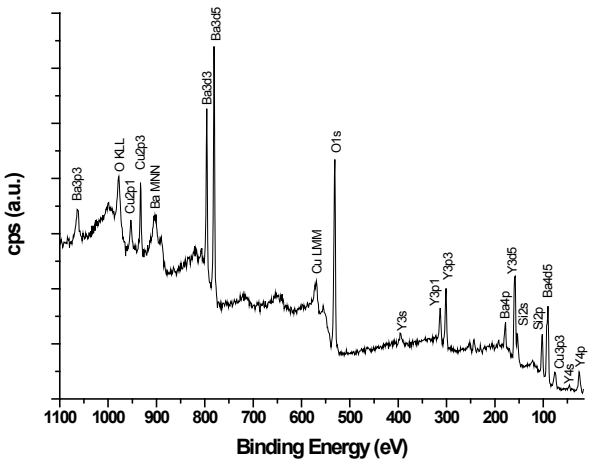

Figure 28: XPS overview spectrum of a sputtered vacuum as-drawn YBCO core surface

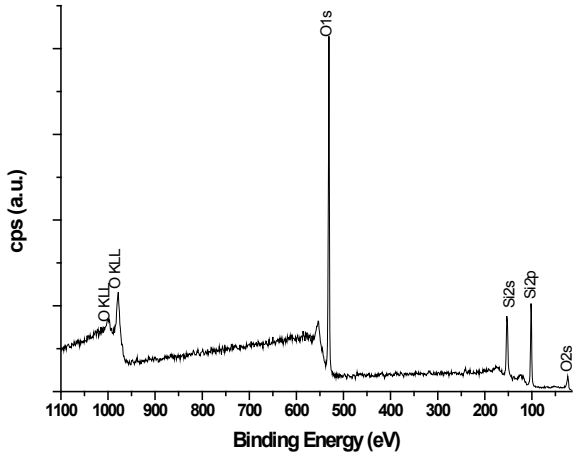

Figure 29: XPS overview spectrum of a sputtered vacuum as-drawn YBCO glass fiber cladding

The composition results of the core and cladding, shown in Table 6, confirm the presence of silicon inside the core (19.3 at.-%) with an approximate equal amount as compared to the results shown in Table 3.

Table 6: XPS analyses on the center of the vacuum as-drawn YBCO core and of the cladding region shown in atomic percent [at.-%]

	Y3p3	**Ba3d5**	**Cu2p3**	**O1s**	**Si2p**
Core	10.0	5.6	5.3	59.8	19.3
Cladding	-	-	-	66.7	33.3

To investigate the nature of this high silicon content inside the core, a high resolution scan of the Si2p peak was performed for the cladding region as well as the core region, as shown in Figure 30, to determine whether silicate formation occurred, for which the Si2p peak is broader and shifted as was described in [85]. The high resolution scan was performed on the non-sputtered surface, so that no bonding information is lost due to the sputtering process.

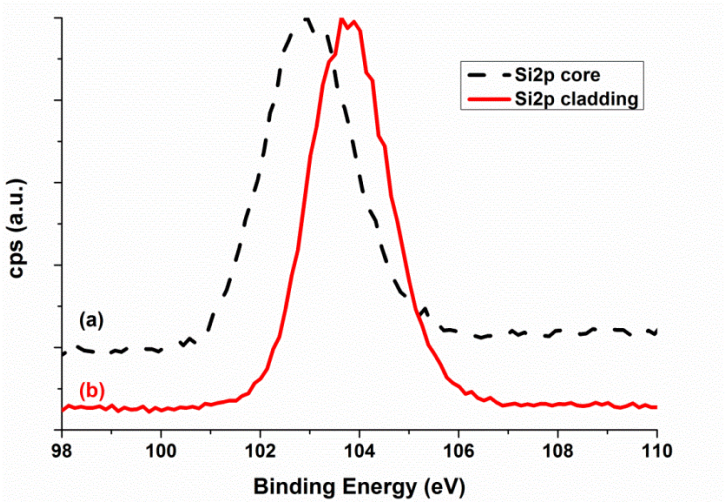

Figure 30: Normalized XPS Si2p peak of the high resolution scan on the non-sputtered surface of **a)** the YBCO core (black dashed line) and **b)** the silica cladding (red solid line)

Figure 30 shows that a broadening and shifting of the Si2p peak occurred. The Si2p peak of the cladding region has a binding energy of 103.6 eV, which corresponds to the binding energy of pure silica [85]. On the other hand, the binding energy of the Si2p peak of the core region is shifted to lower binding energies and lies around 102.9 eV. Furthermore, it is visible that the Si2p peak of the core region is broader as compared to the peak of the cladding material. Hence, this shifting and broadening indicates silicate formation inside the core.

Consequently, in order to determine the phases present inside the vacuum as-drawn YBCO core, XRD analysis on a YBCO core fragment was performed. The fiber core fragment mounted on a Nylon loop for performing the XRD analysis can be seen in Figure 31.

Figure 31: YBCO core fragment mounted with Paratone oil on a Nylon loop

A resulting XRD pattern of the vacuum as-drawn YBCO fiber core can be seen in Figure 32.

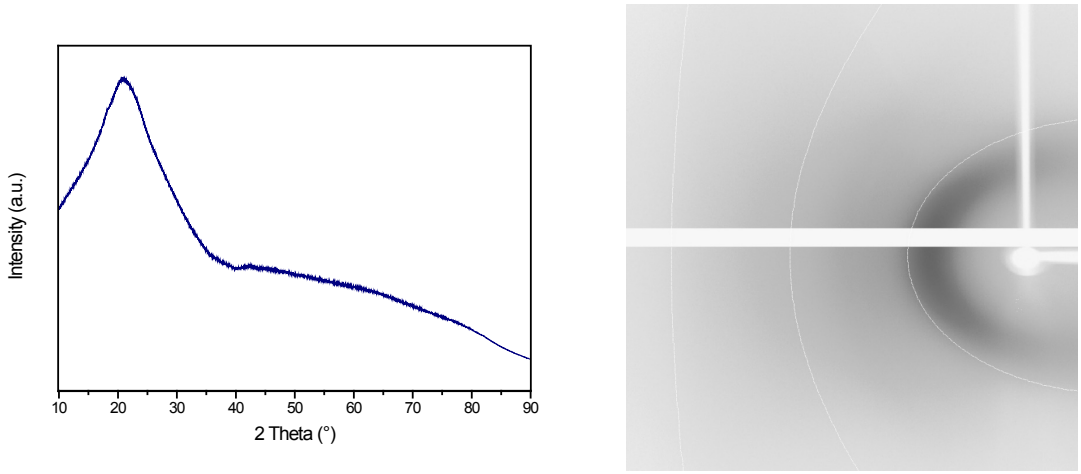

Figure 32: XRD pattern of the vacuum as-drawn YBCO core and the corresponding Debye-Scherrer diffraction ring pattern

As can be seen from the XRD pattern in Figure 32, the core exhibits an amorphous/glassy character. In fact, given the high silicon content inside the core, which forms silicates, and the formation of silica-rich precipitations inside the core, the silica inside the core acts as a glass former leading to the amorphous/glassy phase. In addition, the silica content inside the core favors the melting of Y_2O_3 at lower temperatures by forming lower eutectics, as shown in [76]. These reasons result in the formation of the amorphous YBCO-SiO_2 glass phase.

As a note, the cooling/quenching rate of the as-drawn YBCO fibers on the fiber draw tower can be estimated to be 600 $°Cs^{-1}$ to 2000 $°Cs^{-1}$. The estimation of this rate is performed as follows. It is considered that the hot-zone of the furnace exhibits a temperature of around 2000°C and that the outside temperature of the furnace is around 100°C. Furthermore, it can be estimated that the hot-zone is 20 cm above the lower opening of the furnace and that the hot-zone has a width of around 2.5 cm, which was studied by our group in a previous work [86]. Hence, neglecting the individual cooling rates of silica and YBCO and assuming a nearly linear decrease in temperature will lead to an approximate temperature change of -200°C per cm. This is the maximum cooling rate, assuming instantaneous heat transfer and maintaining uniform temperature throughout the cross-section of the fiber. In general, the draw speed varies between 3 cms^{-1} to 10 cms^{-1} and, hence, the quenching rate can be estimated to be 600 $°Cs^{-1}$ to 2000 $°Cs^{-1}$.

Thus, based on the estimated quenching rates, crystallization upon cooling should have been expected. Therefore, this corroborates our explanation of the formation of the amorphous YBCO-SiO_2 phase.

As stated in Section 2.3.3, a number of works in literature mentioned possible dissolution and diffusion based processes of fused silica into a molten core during the drawing process [21-24, 46-48] of semiconductor core fibers. As will be shown in the following explanation, the high silicon content inside the as-drawn YBCO core is also a result of dissolution and diffusion based reactions between the molten YBCO core and the fused silica cladding.

The high silicon content inside the as-drawn YBCO core is not only a result of a diffusion based process but originates from a dissolution based process between the molten YBCO core and the fused silica cladding. During the drawing process, the molten YBCO core causes the formation of lower eutectics between fused silica and Y_2O_3 [76], as well as between fused silica and the barium- and copper-rich liquid phases [78, 87]. Fused silica can be attacked by glass modifiers inside the molten core at its dangling bonds and bridging-oxygen bonds. Thus, with an increasing content of glass modifiers, the softening point of the fused silica decreases which reduces its viscosity and promotes the dissolution process. The barium oxide, copper oxide as well as yttrium oxide contained in the core are all glass modifiers. Hence, these processes lead to the dissolution of the fused silica into Si^{4+} and O^{2-} ions, which then diffuse into the molten YBCO core. This, indeed, explains the EDS line-scan profiles of the as-drawn YBCO cores shown in Figure 25, Figure 26 and Figure 27. In the dissolution region, the viscosity is higher than the viscosity of the molten-core region, which leads to the diffusion-based concentration gradient shown in Figure 25 and Figure 26. This concentration gradient is, furthermore, caused by the rate-limiting oxygen diffusion through the dissolution region.

In the molten core region, the ions readily mix to give the steady concentration profile observed in the EDS line-scans of the as-drawn YBCO cores shown in Figure 25 and Figure 26. This is due to their higher diffusivity in the liquid state and to the possibility of the occurrence of convection inside the molten core that is induced by a thermal gradient during the drawing process. In addition, due to the dissolution of the fused silica, no out-diffusion of the core material was observed as the

interface moves outwards with the dissolution of the fused silica cladding. This will be further confirmed in Section 3.3.3.

As such, the high silicon content inside the core is due to the dissolution of the fused silica cladding by the molten YBCO core inside the interface region, forming Si^{4+} and O^{2-} ions, which then diffuse into the molten YBCO core. In order to further analyze the effect of the O^{2-} ion diffusion, we next present and discuss the results obtained from our analysis focusing on YBCO glass fibers which were drawn in oxygen atmosphere.

3.1.3 *Results and characterization of as-drawn YBCO fused silica glass fibers in O_2 atmosphere*

YBCO glass fibers were drawn in oxygen atmosphere, in order to investigate the effect of oxygen on the drawing behavior as well as on the reactions between YBCO and the fused silica cladding. As a first step, the preform was softened at the draw tower under vacuum atmosphere, in order to remove any possible outgassing. After the initiation of the draw, oxygen was filled into the preform at a 5 psi oxygen pressure. A YBCO fiber core of an oxygen as-drawn YBCO fiber section can be seen in Figure 33.

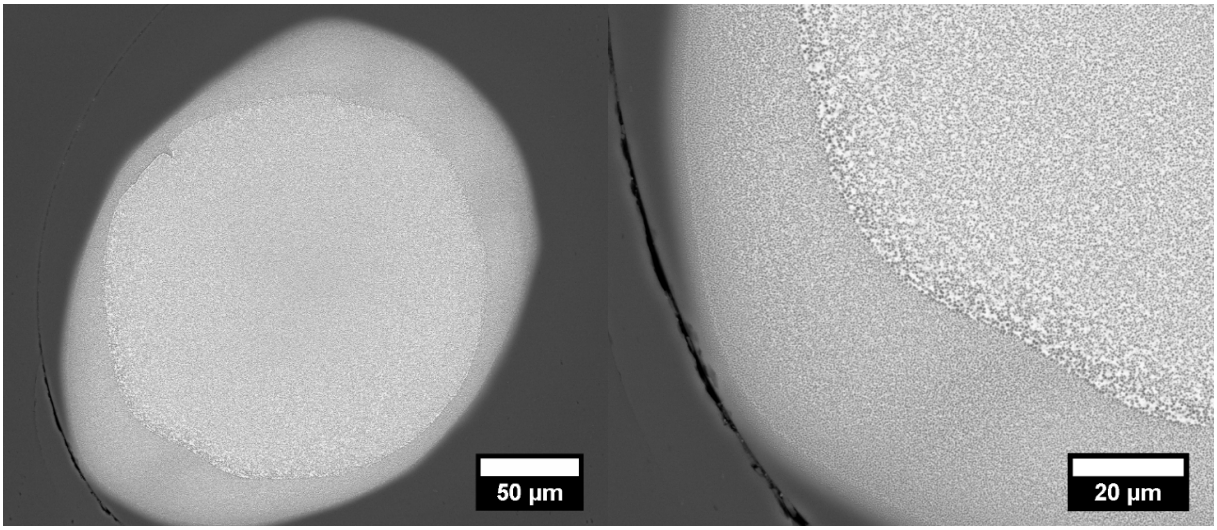

Figure 33: BSE images of an as-drawn YBCO fused silica glass fiber in O_2 atmosphere

As can be seen in Figure 33, a double core structure was obtained during the drawing process as well as precipitation formation inside the entire core. In this regard, the double core structure is attributed to the drawing behavior of molten YBCO.

In fact, during the melting process of YBCO, vapor phases are formed, which can lead to a pressure build up inside the preform that can push up the YBCO melt (away from the hot-zone). Moreover, due to the incongruent melting of YBCO (as shown in Table 1), droplets with air pockets can form. Hence, this can lead to the formation of YBCO coated hollow glass fibers. In fact, a number of our drawing attempts resulted in hollow YBCO glass fibers, in which YBCO formed an inside layer onto the hollow glass fiber inner wall.

Drawing solid core YBCO fibers can be accomplished either by the air pockets being eventually removed without any interference, leading the YBCO melt to be pushed down into the hot-zone (by a final air pocket above the molten YBCO), or by increasing the draw speed to effectively remove the air pockets.

As such, the double core structure, as shown in Figure 33, can be explained by the subsequent occurrence of both processes, which are outlined above, based on which a solid YBCO core forms within a hollow YBCO coated glass fiber.

Moreover, this obtained double core structure shows that a reaction layer of YBCO cannot be used as an effective barrier coating as can be seen from the high silicon content within the core shown in the EDS line-scan in Figure 34.

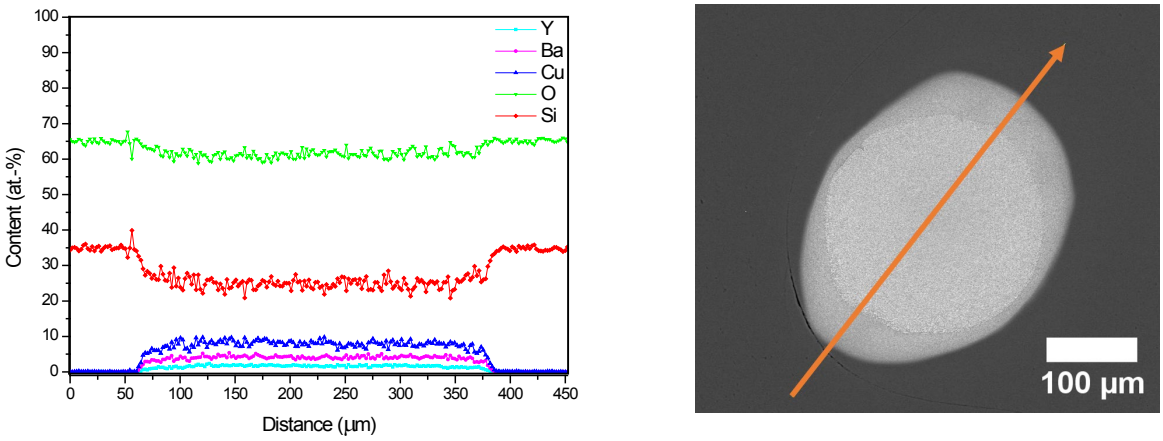

Figure 34: EDS line-scan of an as-drawn YBCO fused silica glass fiber in O_2 atmosphere

Compared to the EDS line-scans of the fibers drawn under vacuum (Figure 25 and Figure 26), the line-scan of a fiber drawn under oxygen atmosphere (Figure 34) shows significantly higher silicon and oxygen content inside the core. Moreover, the higher oxygen content increases the overall silicon diffusion rate inside the YBCO core, as further shown in Table 7, which presents the

variation in silicon and oxygen contents depending on the drawing atmosphere and the region of the core. Thus, these results indicate that oxygen is the rate-limiting step in the co-diffusion of silicon and oxygen ions inside the molten YBCO core, which further corroborates the conclusion drawn in Section 3.1.2.

Table 7: Increase in silicon content inside the core with an increase in oxygen content in as-drawn YBCO glass fibers drawn in vacuum and oxygen atmospheres

Atmosphere (region)	**Silicon content [at.-%]**	**Oxygen content [at.-%]**
Vacuum (center of the core)	20.6 ± 1.3	57.5 ± 0.7
Vacuum (interface)	23.2 ± 0.7	59.3 ± 0.3
O_2 (center of the core)	24.7 ± 1.4	61.2 ± 1.1
O_2 (interface)	26.4 ± 1.8	61.9 ± 1.1
O_2 (at the interface edge towards the cladding)	28.2 ± 0.9	63.6 ± 0.1

In order to analyze the morphology of the YBCO core, high-resolution BSE images of the center of the core were obtained and are shown in Figure 35.

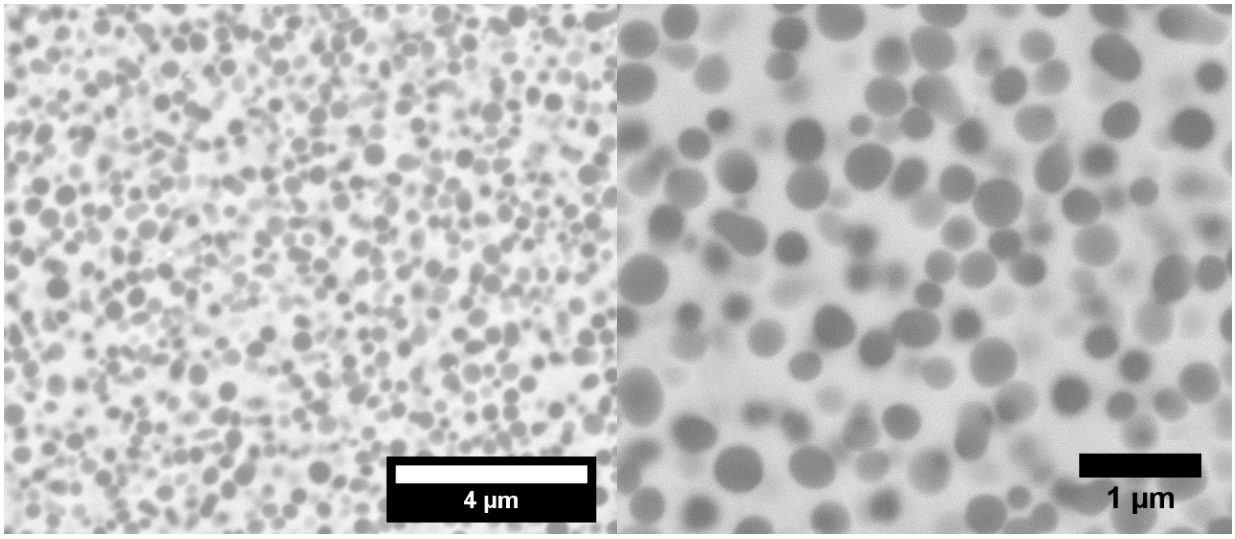

Figure 35: BSE images of the center of an as-drawn YBCO fused silica glass fiber in O_2 atmosphere

The BSE images in Figure 35 reveal the formation of silica-rich precipitations across the entire core for the oxygen drawn fibers. In contrast, our results for the vacuum as-drawn fibers, presented in Section 3.1.2, showed silica-rich precipitation formations at the interface layer but not across the entire core. This precipitation formation across the entire core in the oxygen drawn fibers stems from the excess of oxygen, which enables the increase in diffusion of both silicon and oxygen ions into the molten core. This is further addressed in Section 3.1.5.

Furthermore, Figure 36 shows a BSE image of the interface region of an oxygen as-drawn YBCO fused silica glass fiber. The fiber core shows a spinodal-like phase separation morphology at the interface region.

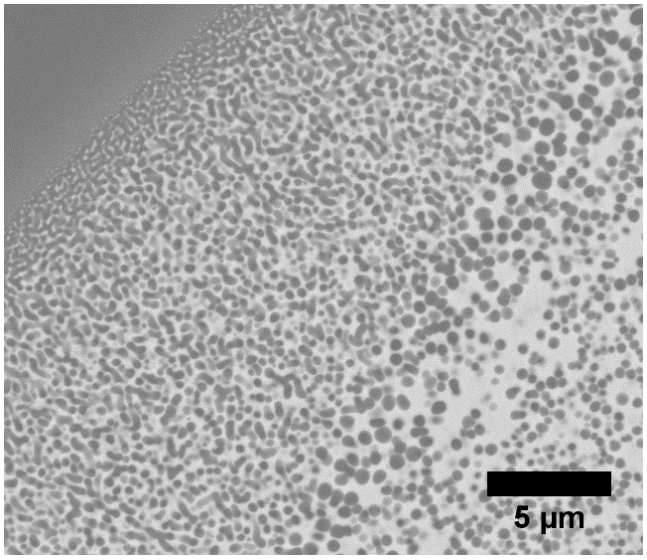

Figure 36: BSE image of the interface region of an as-drawn YBCO fused silica glass fiber in O_2 atmosphere

In order to analyze the core composition, XRD analysis was performed and the corresponding XRD pattern is shown in Figure 37.

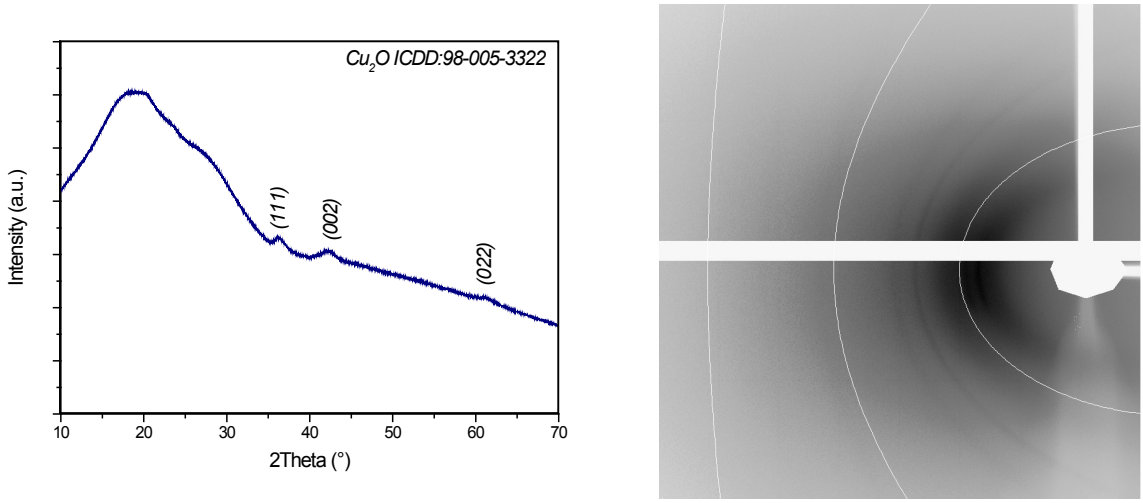

Figure 37: XRD pattern of an as-drawn YBCO fused silica glass fiber in O_2 atmosphere and the corresponding Debye-Scherrer diffraction ring pattern

The XRD pattern in Figure 37 indicates that the oxygen as-drawn YBCO core is mainly amorphous with some minor quantities of crystalline cuprite, implying the silica-rich precipitations inside the core are amorphous. We note that the silica-rich precipitations have a particle size of around 200-

300 nm, i.e. of sufficient size to preclude the possibility of the particles being crystalline, but unobserved due to particle size line-broadening. Section 3.1.6 will discuss the reason as to why cuprite is the first phase to crystallize out of the amorphous silicate phase.

In order to further confirm this conclusion, a Raman measurement was performed on the center of the core and the result can be seen in Figure 38.

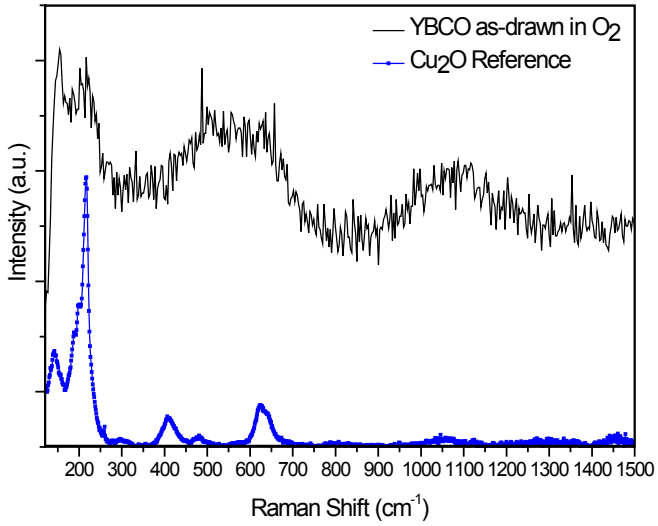

Figure 38: Raman spectrum of an as-drawn YBCO fused silica glass fiber in O_2 atmosphere; Reference from RUFF database: Cu_2O (R050384)

Figure 38 shows no formation of crystalline silica phases. The broad peak at 218 cm^{-1} can indicate that a minor cuprite mode is visible, which is attributed to the second-order Raman-allowed mode ($2E_u$) of cuprite (~218 cm^{-1}) as highlighted in [88, 89]. The other broader peaks can originate from an overlay of the amorphous matrix with the cuprite Raman modes. Overall, the Raman spectrum in Figure 38 is inconclusive due to the broad peaks. Here, we note that the visible Raman shift at around 154 cm^{-1} can be caused by the cut-off edge of the optical long-pass filter of the system.

In general, drawing YBCO glass fibers in an oxygen atmosphere did not lead to any mitigation of the YBCO and silica reaction. Hence, the oxygen atmosphere does not provide improvements as compared to drawing in vacuum.

3.1.4 *Results and characterization of as-drawn YBCO+15 wt-% Ag_2O borosilicate glass fibers in vacuum atmosphere*

In order to analyze the effect of lowering the drawing temperature on the reactions within YBCO and silica, YBCO glass fibers were drawn using borosilicate glass as the preform material. YBCO has the first peritectic melting point at around 1002°C, as shown in Table 1, while borosilicate softens at around 821°C. Hence, in order to be able to draw YBCO powder inside the borosilicate preform, Silver (I)-oxide was added to the YBCO powder to lower the overall melting temperature as discussed in Section 3.1.1.

Due to the fact that the melting point of the powder exceeds the softening point of the borosilicate preform, the draw needed to be performed at temperatures higher than those normally used for borosilicate fiber draws, which introduced a number of challenges during the drawing process. Nonetheless, it was still possible to draw some solid core YBCO glass fibers, as can be seen in Figure 39.

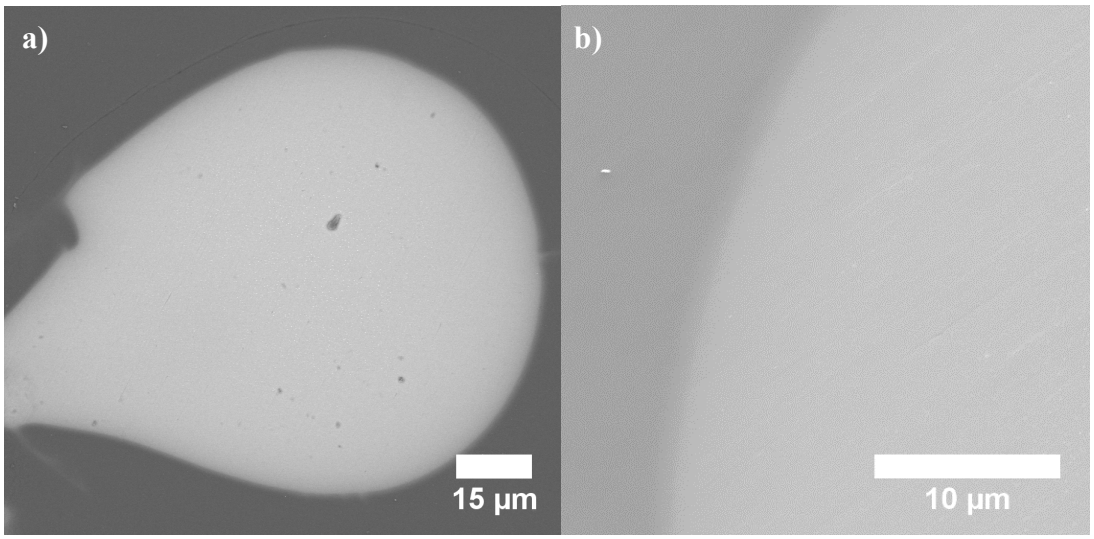

Figure 39: BSE images of an as-drawn YBCO+ 15 wt.-% Ag_2O borosilicate glass fiber in vacuum atmosphere **a)** entire core and **b)** interface region

As can be seen in Figure 39, the core does not show any precipitation formation neither inside the core nor at the interface region, as can be seen in Figure 39 b). However, Figure 39 b) shows that the interface between the cladding and the core is not distinct, which is an indication of an occurring diffusion process. Furthermore, Figure 40 reveals that silver-rich spherical precipitations form in the sub-micrometer to nanometer scale, which is common to occur in glass-forming

materials upon annealing [90]. The spherical silver-rich precipitations were confirmed with EDS point analysis, as can be seen in Table 8.

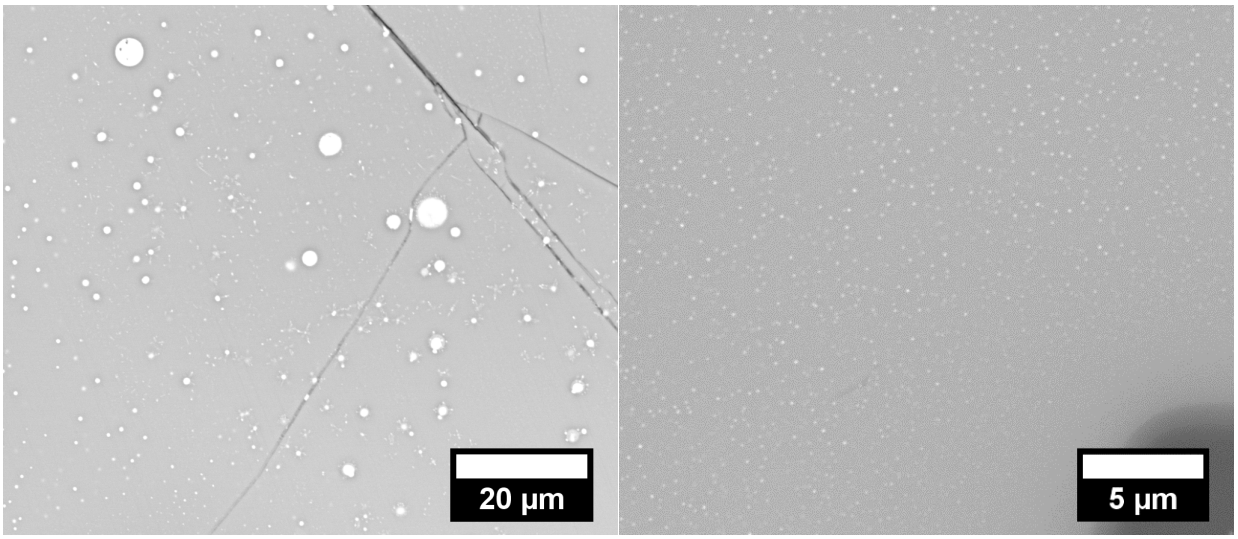

Figure 40: BSE images of silver-rich precipitations in two different as-drawn YBCO+15 wt-% Ag_2O borosilicate glass fiber section cores in vacuum atmosphere

Table 8: EDS point analysis on the spherical precipitation of the vacuum drawn YBCO+15 wt-% Ag_2O borosilicate glass fiber core shown in atomic percent [at.-%]

Y	Ba	Cu	O	Si	Ag
0.0	0.7	1.6	28.5	0.9	68.3

In order, to analyze the dissolution of the fused silica and the subsequent diffusion of Si^{4+} and O^{2-} ions inside the YBCO/Ag_2O core, an EDS line-scan was performed and can be seen in Figure 41. It is important to note that boron inside the glass cladding cannot be detected using EDS analysis on an SEM.

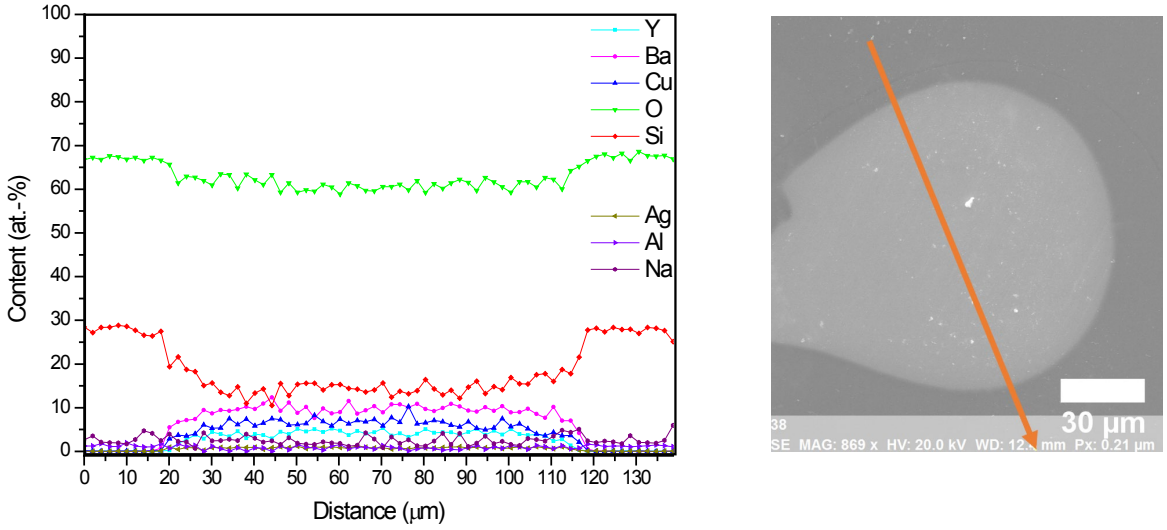

Figure 41: EDS line-scan of an as-drawn YBCO+15 wt-% Ag_2O borosilicate glass fiber section in vacuum atmosphere

The EDS line-scan in Figure 41 shows that, as compared to the fiber sections shown in Sections 3.1.2 and 3.1.3 and whose results can be seen in Table 7, the silicon content inside the core is reduced (around 15.1 at-%) and a stronger diffusion profile of silicon ions inside the core is visible. In addition, the oxygen content inside the core is relatively high. This can be attributed to the silver (I)-oxide, which can act as an oxygen donor [91]. In addition, Figure 41 shows that the yttrium to barium to copper ratio of 1:2:3 is not obtained and that the barium content exceeds the copper content. This is due to the relatively low drawing temperature, which can lead to partial melting of YBCO and to the fact that barium has the lowest melting point. This explanation is further corroborated by the analysis of additional fiber sections, which showed nearly no melting of the core material and a high copper content inside the core, as can be seen in Appendix 1. In order to investigate the core composition further, XRD analysis was performed and can be seen in Figure 42.

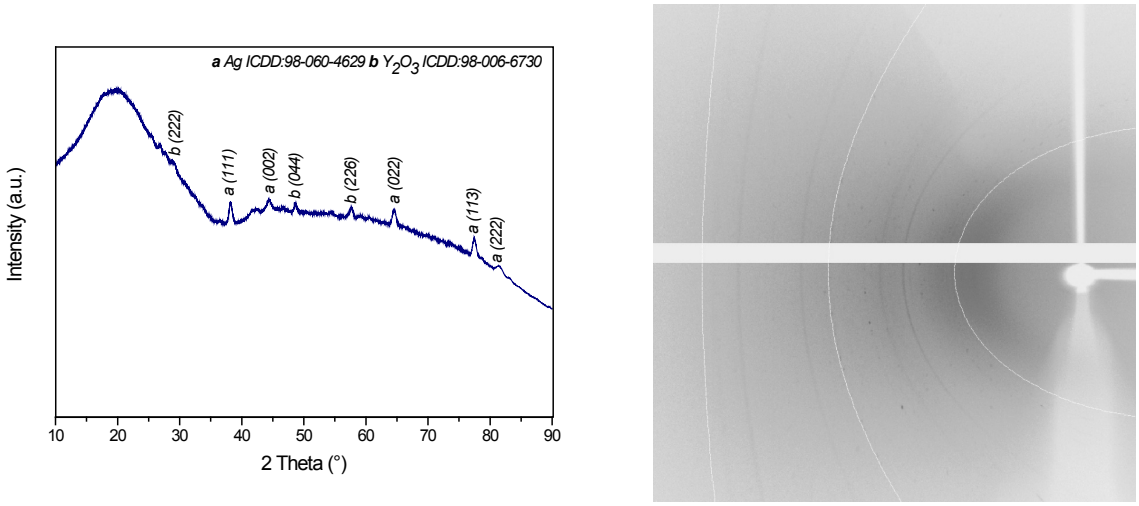

Figure 42: XRD pattern on an as-drawn YBCO+15 wt-% Ag_2O borosilicate glass fiber section core in vacuum atmosphere and the corresponding Debye-Scherrer diffraction ring pattern

Figure 42 shows that, in addition to an amorphous phase, silver and yttria (Y_2O_3) are present inside the core. This result confirms the formation of spherical silver-rich precipitations inside the core. In addition, the presence of yttria shows that the used drawing temperature is above the second peritectic melting of YBCO. Moreover, the silicon diffusion profile in Figure 41 and the absence of silica-rich precipitations demonstrate that a minor dissolution of the borosilicate cladding into its ions occurred as compared to the draws at higher temperatures using a fused silica cladding. In addition, Figure 41 shows that aluminum ion diffusion from the cladding material inside the core occurred with an overall content of around 1 at.-%. This can constitute one of the reasons for which no phase separation occurred inside the core [92]. Other underlying reasons are addressed in the following section.

3.1.5 *Summary and conclusion of the results obtained for as-drawn YBCO glass fibers*

It was shown in Section 3.1.2 that vacuum as-drawn YBCO cores are amorphous and exhibit silicate formation inside the core. Moreover, it was shown that silica-rich precipitations occur, for vacuum drawn fused silica fiber sections, forming an interface layer between the core and the cladding region. In addition, Section 3.1.3 revealed that drawing YBCO glass fibers under oxygen atmosphere leads to silica-rich precipitations inside the entire core in addition to an amorphous silicate phase with a minor crystalline cuprite phase. XRD and Raman measurements showed that these silica-rich precipitations are of amorphous nature. Furthermore, it was revealed that the oxygen atmosphere increases the dissolution rate of fused silica into its Si^{4+} and O^{2-} ions and their

subsequent diffusion inside the YBCO core. This showed that oxygen is the rate-limiting factor in the co-diffusion of Si^{4+} and O^{2-} ions into the molten YBCO core.

An overall atomic percentage average of the core materials is shown in Figure 43 for the vacuum and oxygen atmosphere fibers with fused silica cladding. In addition, to better illustrate the oxide ratios inside the core, Figure 43 shows the theoretically calculated mole percentages of Y_2O_3, BaO, Cu_2O as well as SiO_2 inside the core.

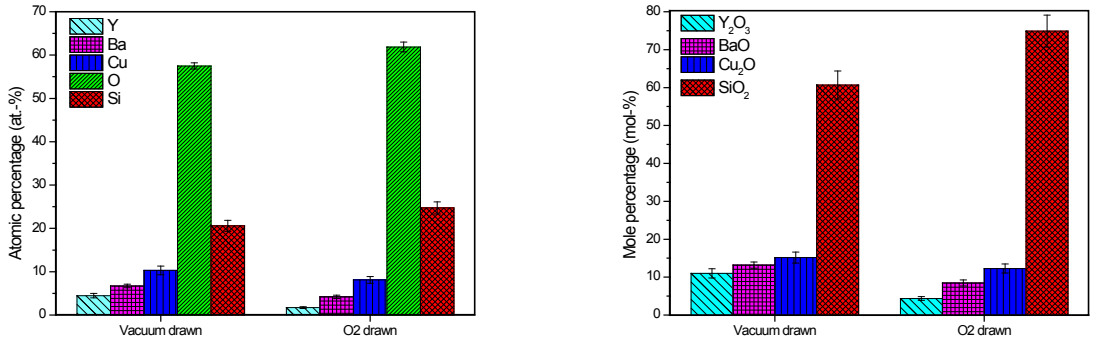

Figure 43: Comparison of yttrium, barium, copper, silicon and oxygen content of different draw conditions in atomic percentages (left) and mole percentages (right) (content shown as average over the steady part of the entire core)

It is clearly visible in Figure 43 that the silicon (24.7 at.-%) as well as the oxygen (61.8 at.-%) contents increased for the oxygen drawn YBCO core as compared to the vacuum drawn YBCO core (Si: 20.6 at.-% and O: 57.5 at.-%). As a result, the yttrium, barium and copper contents are reduced for the oxygen drawn YBCO core as compared to the vacuum drawn YBCO core. Moreover, the higher silica content inside the core of the oxygen drawn YBCO fibers is highlighted in the mole percentage comparison chart in Figure 43. In this regard, Section 3.1.2 presented the reasons for which a dissolution of the fused silica into Si^{4+} and O^{2-} ions and their subsequent diffusion inside the molten YBCO core occur. The reasons for the formation of the silica-rich precipitations in the YBCO glass fiber cores are discussed next.

Section 2.3.4 described the phase separation in glass-forming systems. The example of the BaO-SiO_2 system was given in Section 2.3.4, based on [51-53], which stated that depending on the barium to silica ratio, either spherical barium-rich/silica-rich precipitations or two interconnected phases form. In addition, miscibility gaps are also mentioned for the Y_2O_3-SiO_2 [57, 58] and Cu_2O-SiO_2 [56] system. Thus, it is evident from our obtained results that such a miscibility gap also

exists for the quaternary Y_2O_3-BaO-Cu_2O-SiO_2 (YBCO-SiO_2) system. Moreover, for the soda-lime-silica glass system [50, 93], the oxygen diffusion is reported to be the rate controlling factor in the phase separation process, which corroborates the conclusion that oxygen increases the silica-rich precipitation formation.

Table 9 illustrates the morphology change of the cores of the vacuum and oxygen as-drawn YBCO glass fibers with respect to the change in silica content in the core. The first column of Table 9 shows that the center of the core of the vacuum drawn fiber contains no silica-rich precipitations, which implies that the composition lies outside of the miscibility gap. Column 2 shows precipitations at the interface region of the vacuum as-drawn fibers, which implies that its composition lies within the binodal curve. Columns 3, 4 and 5 illustrate the precipitation formation with respect to the silica concentration for the oxygen drawn fiber over the center region of the core, at the interface region and at the interface edge towards the cladding, respectively. In all three cases, the composition lies within the binodal curve. Based on the results in Table 9, the occurrence of a miscibility gap for the Y_2O_3-BaO-Cu_2O-SiO_2 system, which exists for temperatures above the lower eutectic temperature of the Y_2O_3-SiO_2 system of around 1660°C [94], can be concluded. This emphasizes that the silica-rich precipitation formation occurs when the composition lies inside the metastable binodal curve. The kinetic mechanism of the formation of those silica-rich precipitations stems from a nucleation and growth process. In fact, the silica-rich precipitations are not likely to result from spinodal phase separation due to their small scale. The spinodal phase separation morphology at the core/cladding interface, as it is shown for the oxygen drawn fiber section in the two rightmost columns of Table 9, can be due to entering an unstable spinodal region inside the miscibility gap or caused by a coalescence of the spherical silica-rich precipitations as part of a nucleation and growth process.

Attempts to analyze the nucleation and growth process were not successful due to the occurrence of crystallization processes, which will be further discussed in Section 3.1.6. The crystallization occurs at the interface between the silica-rich precipitations and the amorphous silicate matrix phase, which is energetically favorable due to the lower energy barrier at the interface region. This crystallization at the interface region is shown through the formation of the so-called co-precipitations, which will be further discussed in Section 3.1.6. This explains why the oxygen as-drawn YBCO fibers show cuprite inside the core, as shown in Figure 37, while the vacuum as-

drawn YBCO fibers have an amorphous core. As such, the increased formation of new interfaces with the increase in the number of silica-rich precipitations inside the oxygen as-drawn YBCO fiber core promotes the recrystallization of the cuprite phase upon quenching.

In addition, Section 3.1.4 showed that using borosilicate glass instead of fused silica as the preform material and by adding silver oxide to the YBCO powder in order to reduce the melting point of YBCO, allowed drawing YBCO glass fibers at reduced temperatures. The borosilicate drawing led to an amorphous core with spherical silver-rich particles and a minor crystalline yttria phase. As such, it was demonstrated that no silica-rich precipitations occurred, which corroborates the explanation above on the origin of the silica-rich precipitations in the YBCO-SiO_2 system.

Overall, these results are the first to show the occurrence of a phase separation mechanism in the YBCO-SiO_2 system, and the first to demonstrate the change in morphology depending on the silica content inside the core.

Furthermore, in order to investigate whether the superconductive Y-123 phase can be restored/recrystallized, recrystallization processes of the amorphous as-drawn YBCO glass fibers are required. In this regard, it is of high importance to determine whether the silicon content inside the core hinders the recrystallization process of the Y-123 phase. Therefore, heat-treatment studies were performed on as-drawn YBCO fibers in air and oxygen atmospheres and the obtained results are shown and discussed in the following section.

Table 9: Morphology change depending on mol-% of silica shown for as-drawn YBCO fused silica core fiber sections drawn under vacuum and O_2 atmospheres

	RT vacuum core	**RT vacuum interface**	**RT oxygen core**	**RT oxygen interface**	**RT oxygen interface**
	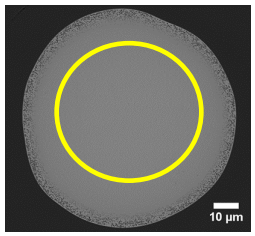	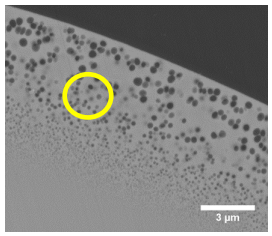	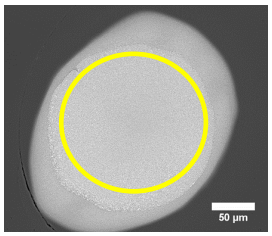	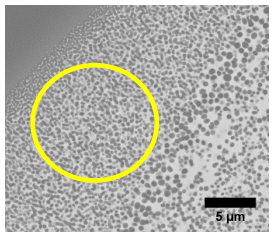	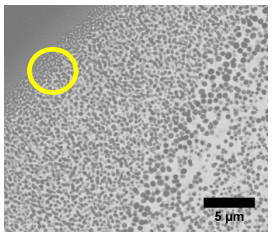
SiO_2	60.7 ± 3.7 mol-%	68.6 ± 2.2 mol-%	74.9 ± 4.2 mol-%	79.4 ± 5.3 mol-%	85.5 ± 2.8 mol-%
Cu_2O	15.2 ± 1.5 mol-%	12.1 ± 0.8 mol-%	12.3 ± 1.2 mol-%	10.5 ± 1.9 mol-%	7.7 ± 0.5 mol-%
BaO	13.2 ± 0.8 mol-%	12.4 ± 0.1 mol-%	8.5 ± 0.8 mol-%	7.0 ± 1.0 mol-%	5.0 ± 0.8 mol-%
Y_2O_3	11.0 ± 1.2 mol-%	6.9 ± 0.8 mol-%	4.4 ± 0.5 mol-%	3.1 ± 0.6 mol-%	1.8 ± 0.2 mol-%
decrease in SiO_2 content ←					
Morphology interpretation	Outside the miscibility gap (solid solution)	Inside the binodal region (nucleation and growth)	Inside the binodal region (nucleation and growth)	Close to spinodal line or coalescence of silica-rich precipitations	Close or inside the spinodal region or coalescence of silica-rich precipitations
	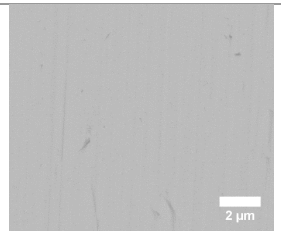	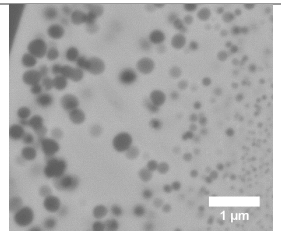	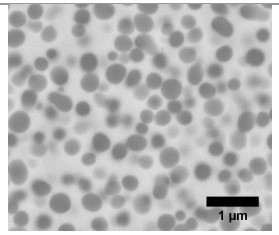	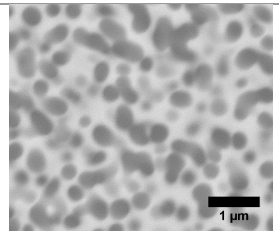	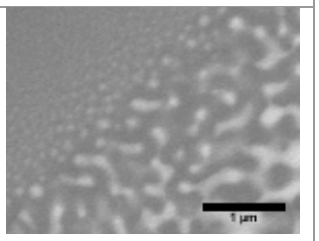

3.1.6 *Results and characterization of heat-treated vacuum as-drawn YBCO fused silica glass fibers*

To investigate the possibility of restoring the superconductive Y-123 phase and further analyze the reactions within YBCO glass fibers, heat-treatment studies on as-drawn YBCO fiber sections were performed at elevated temperatures in air atmosphere as well as under flowing oxygen. In general, heat-treatment studies are indispensable for the understanding of the reactions within the YBCO glass fibers and for the investigation of the possibility of restoring the Y-123 phase. In this regard, Section 3.1.6.1 focuses on the additional heat-treatments in air atmosphere while Section 3.1.6.3 analyses the additional heat-treatments in oxygen atmosphere.

3.1.6.1 Heat-treated as-drawn YBCO glass fibers in air atmosphere

For the heat-treatments, a temperature range of 800°C to 1200°C was chosen due to its relevance to the processing of the melt-textured growth of YBCO [72]. BSE images of the reaction profile of the YBCO core, heat-treated at temperatures between 800°C and 1200°C for a dwelling time of 10 min with heating and cooling rates of 5°Cmin^{-1} in air are shown in Figure 44 and Figure 45.

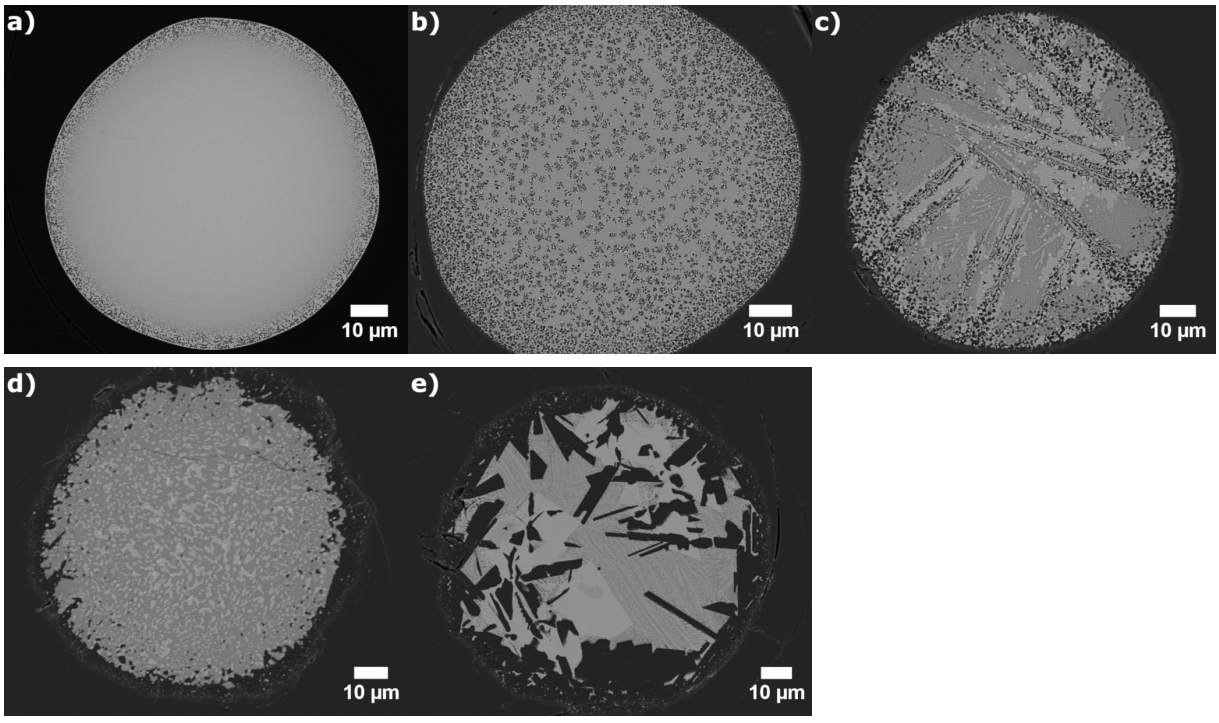

Figure 44: BSE images of YBCO fiber cross-sections heat-treated at **a**) 800°C, **b)** 900°C, **c)** 1000°C, **d)** 1100°C and **e)** 1200°C for a dwelling time of 10 min in air atmosphere

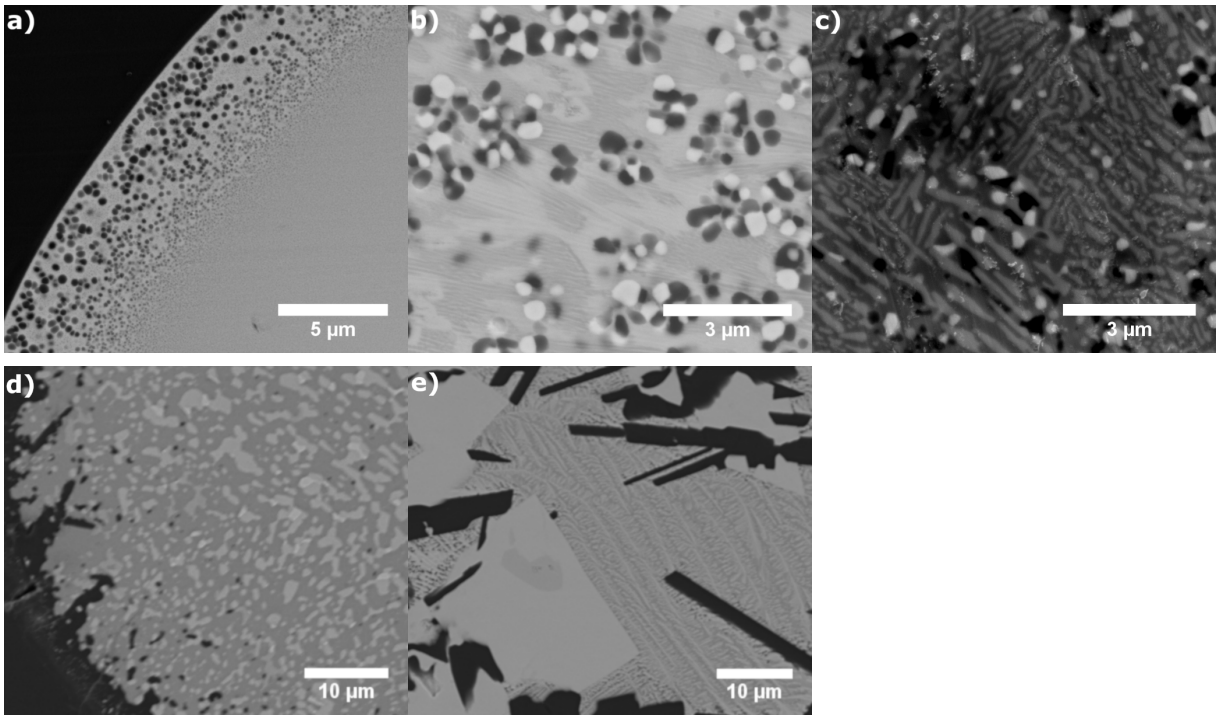

Figure 45: BSE images (with higher magnification) of YBCO fiber cross-sections heat-treated at **a)** 800°C, **b)** 900°C, **c)** 1000°C, **d)** 1100°C and **e)** 1200°C for a dwelling time of 10 min in air atmosphere

The BSE images, in Figure 44 and Figure 45, show no significant change in the silica-rich precipitation layer at 800°C as compared to the as-drawn fiber shown in Figure 24. However, at 900°C, it can be observed that co-precipitations are formed in the entire core. Moreover, at 1000°C, these co-precipitations begin to react and form new phases. At 1100°C, the sharp interface between the cladding and the core disappears. In addition, it can be seen in Figure 45 that more than one phase are present in the matrix at 900°C and 1000°C, which form a lamellar structure.

To analyze the precipitations and phases formed, EDS analyses as well as XRD analyses were performed on the heat-treated fibers. The XRD result for the sample heat-treated at 800°C is shown Figure 46.

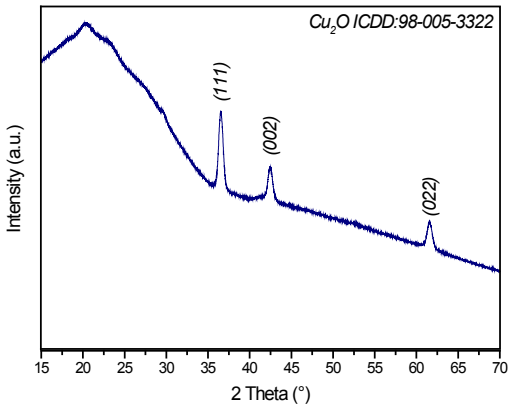

Figure 46: XRD pattern of the heat-treated vacuum as-drawn YBCO fiber core at 800°C for a dwelling time of 10 min in air

The XRD pattern in Figure 46 shows minor microcrystalline peaks in addition to a large amorphous peak. The reflection peaks can be indexed to belong to Cu_2O. Such a Cu_2O recrystallization out of a glassy phase was previously reported for the BSCCO system [95-100]. However, contrary to YBCO, BSCCO contains bismuth oxide (Bi_2O_3), which can act as a glass forming agent and, hence, BSCCO can be quenched to a completely glassy phase [101]. Cu (II)-oxide, which is one of the components in the YBCO system as shown in Table 1, typically transforms above 1026°C [35] into Cu (I)-oxide. Hence, the copper ions during the drawing process inside the YBCO melt are mainly Cu^+-ions. As a result, regarding the copper oxidation state, the amorphous quenched core of the as-drawn fibers mainly consists of Cu^+-ions, which form Cu_2O upon recrystallization. Moreover, as stated in Section 2.6.4, it is reported in [56] that no copper silicates or solid solutions are formed in the CuO-Cu_2O-SiO_2 system up to 1072°C. Hence, this explains the reason as to why pure Cu_2O can crystallize out of the melt despite the high silicon content inside the amorphous core. In addition, Cu_2O formation at low temperatures due to a reaction between silica and YBCO was investigated in [17], which considered a YBCO film on a silica substrate. This also explains the cuprite formation for as-drawn YBCO glass fibers in oxygen atmosphere, which is discussed in Section 3.1.3 and shown in Figure 37.

In addition, the EDS point analysis of the co-precipitations, which formed at 900°C, shows that the darker precipitations are rich in silicon and oxygen with a ratio of 1:2 and the lighter precipitations are rich in copper and oxygen with a ratio of 2:1. This can be seen in Table 10 taking the large excitation volume of the X-rays into consideration and accounting for the overlap with

the SiO_2 phase. Hence, this indicates the formation of cuprite (Cu_2O) precipitations next to silica-rich precipitations, which form co-precipitations.

Table 10: EDS point analysis on the lighter and darker co-precipitations in the vacuum as-drawn YBCO core, heat-treated at 900°C for a dwelling time of 10 min in air atmosphere, shown in atomic percent [at.-%]

	Y	Ba	Cu	O	Si
Darker	1.4	1.5	9.6	58.4	29.1
Lighter	1.0	1.5	44.6	42.2	10.7

In order to confirm these results, XRD analysis was performed on the YBCO core heat-treated at 900°C and can be seen in Figure 47. The XRD pattern in Figure 47 shows the formation of a cristobalite phase in addition to a microcrystalline cuprite formation. Hence, this allows identifying the lighter co-precipitations at 900°C, which are shown in Figure 45 b), to consist of Cu_2O.

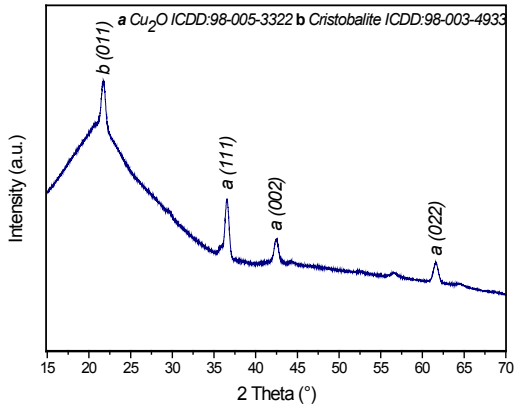

Figure 47: XRD pattern of the heat-treated vacuum as-drawn YBCO fiber core at 900°C for a dwelling time of 10 min in air

To further visualize the composition distribution of the co-precipitations, high magnification EDS mapping of the co-precipitations was performed and can be seen in Figure 48.

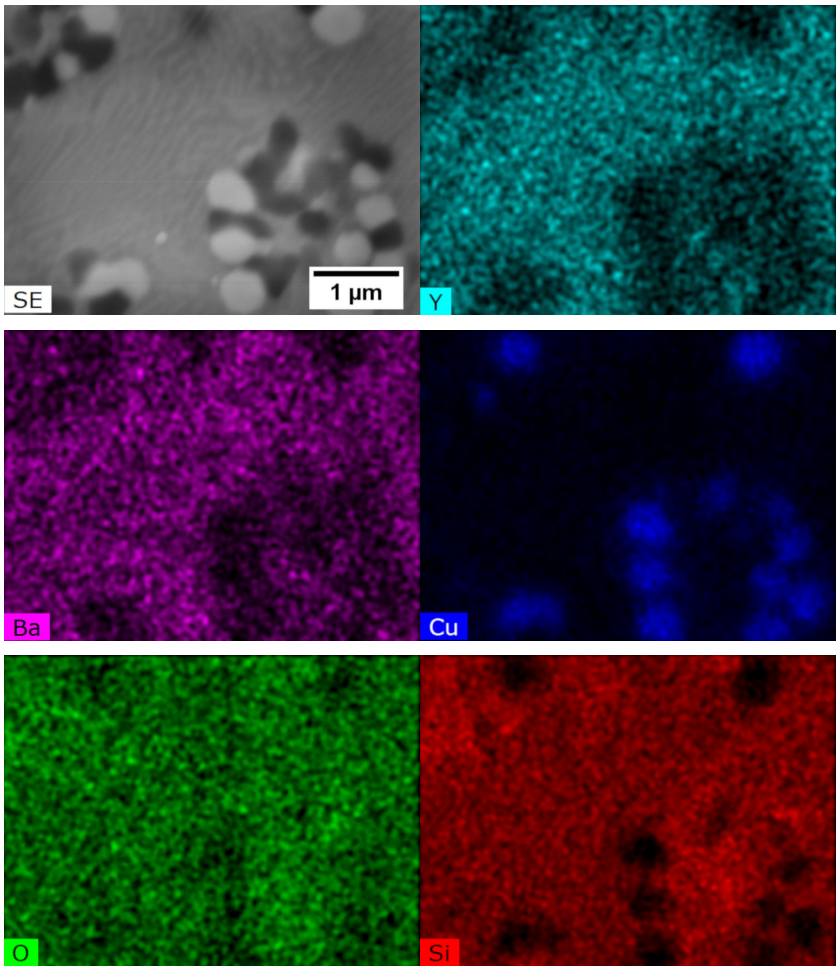

Figure 48: EDS mapping of the co-precipitations inside the YBCO core heat-treated at 900°C for a dwelling time of 10 min in air atmosphere (scale bar 1 µm)

Figure 48 shows that, at the copper-rich precipitations (lighter precipitations), the silicon content is highly reduced, which further confirms the formation of Cu_2O precipitations inside the core.

In order to analyze the cristobalite phase, which forms at 900°C inside the core, Raman measurements were performed on the 900°C and 1000°C heat-treated YBCO fiber cores. The corresponding Raman spectra are shown in Figure 49 and Figure 50, respectively. The Raman spectrum in Figure 49, obtained from measurements performed on the center of the heat-treated YBCO core, only shows Raman modes originating from the cuprite phase. In Figure 50, the heat-treated YBCO fiber core/cladding interface at 1000°C shows both cuprite and cristobalite modes.

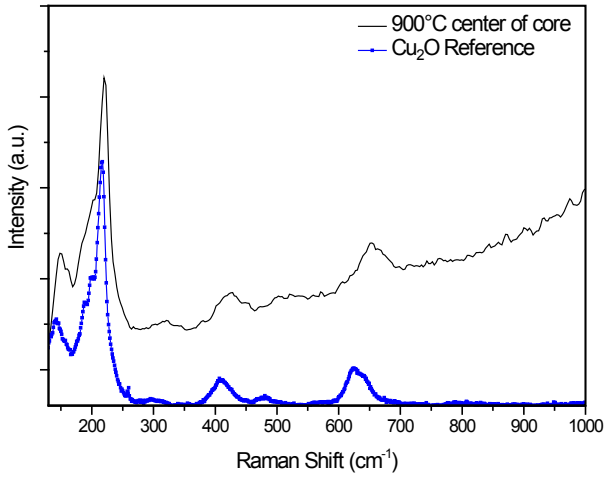

Figure 49: Raman spectrum at the center of a vacuum as-drawn YBCO fiber core heat-treated at 900°C for a dwelling time of 10 min in air; Reference from RUFF database: cuprite (R050384)

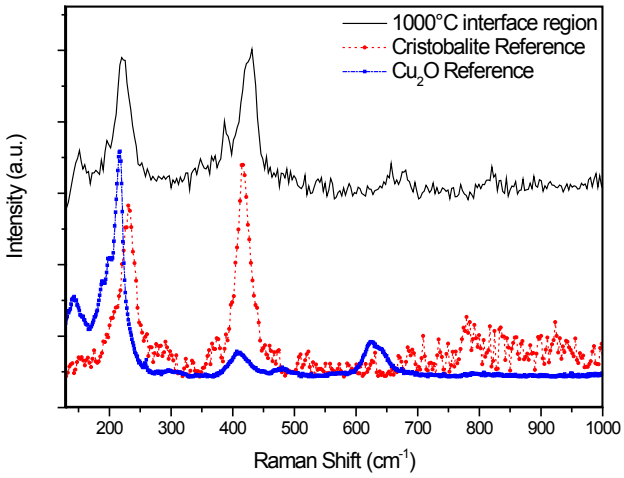

Figure 50: Raman spectrum at the core/cladding interface region of a vacuum as-drawn YBCO fiber heat-treated at 1000°C for a dwelling time of 10 min in air; Reference from RUFF database: cristobalite (X050046) and cuprite (R050384)

In fact, the work in [102] describes the formation of cristobalite in the interface region of liquid silicon and vitreous silica, as can be seen in Figure 51 a).

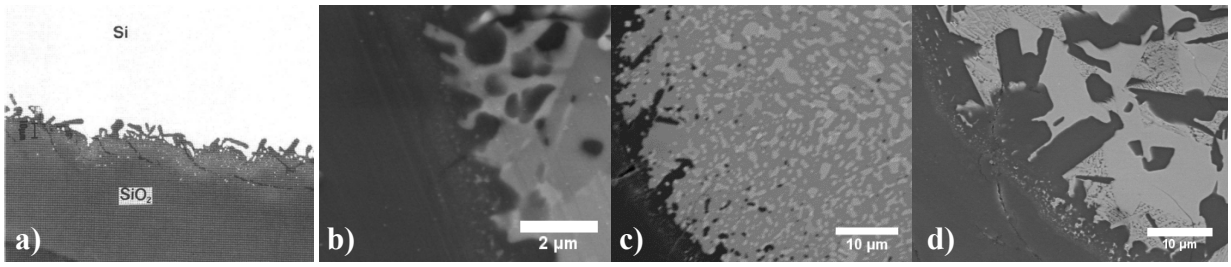

Figure 51: a) Interface layer of cristobalite image taken from [102] compared to the obtained YBCO samples heat-treated at **b)** 1000°C, **c)** 1100°C and **d)** 1200°C for 10 min in air

The interface structure in Figure 51 a) shows close similarity to the morphology features of the core/cladding interface region of our heat-treated YBCO fiber sections at 1000°C, 1100°C and 1200°C, as shown in Figure 51 b) to d), respectively. This, hence, further suggests that cristobalite forms at the interface region.

The EDS mappings of the YBCO core heat-treated at 1000°C to 1200°C are shown in Figure 52 to Figure 54.

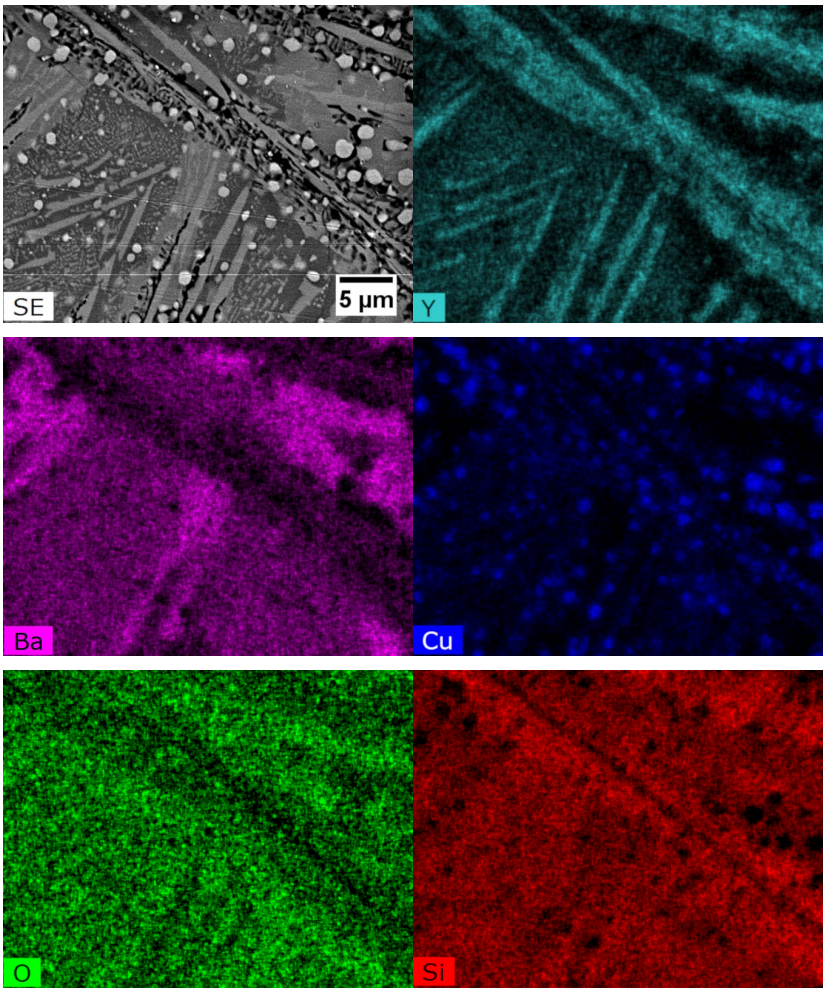

Figure 52: EDS mapping of the vacuum as-drawn YBCO core heat-treated at 1000°C for a dwelling time of 10 min in air atmosphere (scale bar 5 µm)

Figure 52 to Figure 54 show that, at 1000°C, a yttrium-rich phase begins to form. Figure 52 to Figure 54 also show that, in addition to the yttrium-rich phase, a barium-rich phase is formed inside the core at 1000°C, which transforms to a barium-copper-rich phase at 1200°C. In addition, Figure 54 shows the presence of the silica cladding material inside the core at 1200°C.

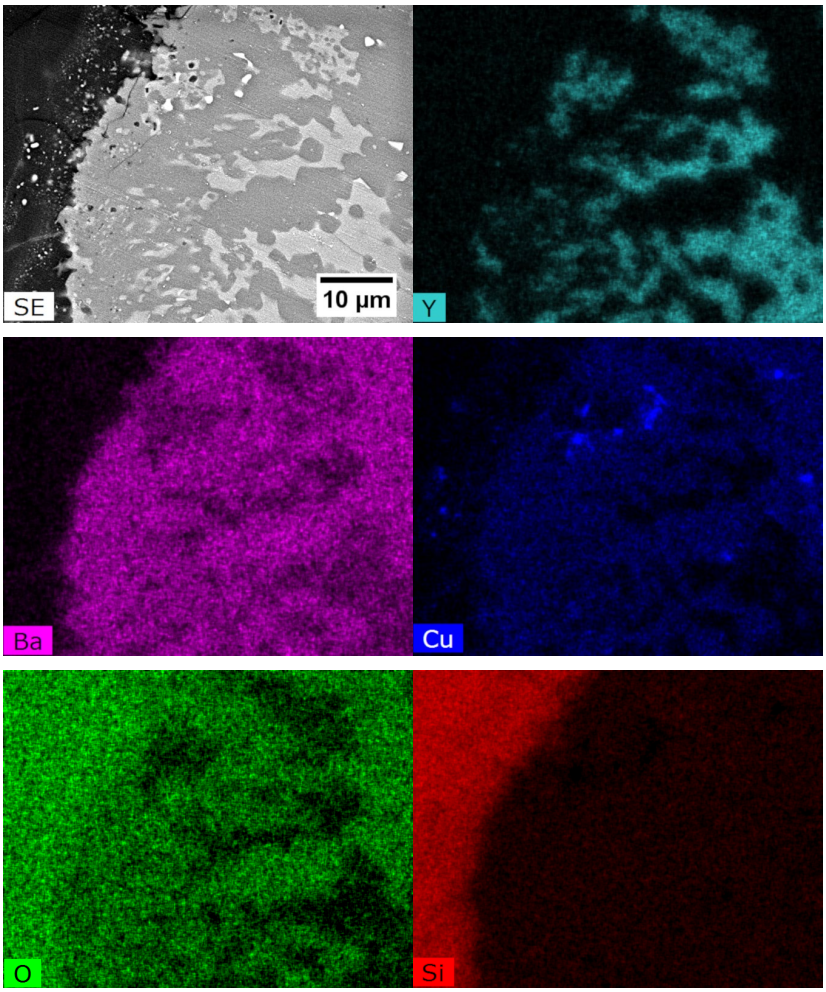

Figure 53: EDS mapping of the vacuum as-drawn YBCO core heat-treated at 1100°C for a dwelling time of 10 min in air atmosphere (scale bar 10 µm)

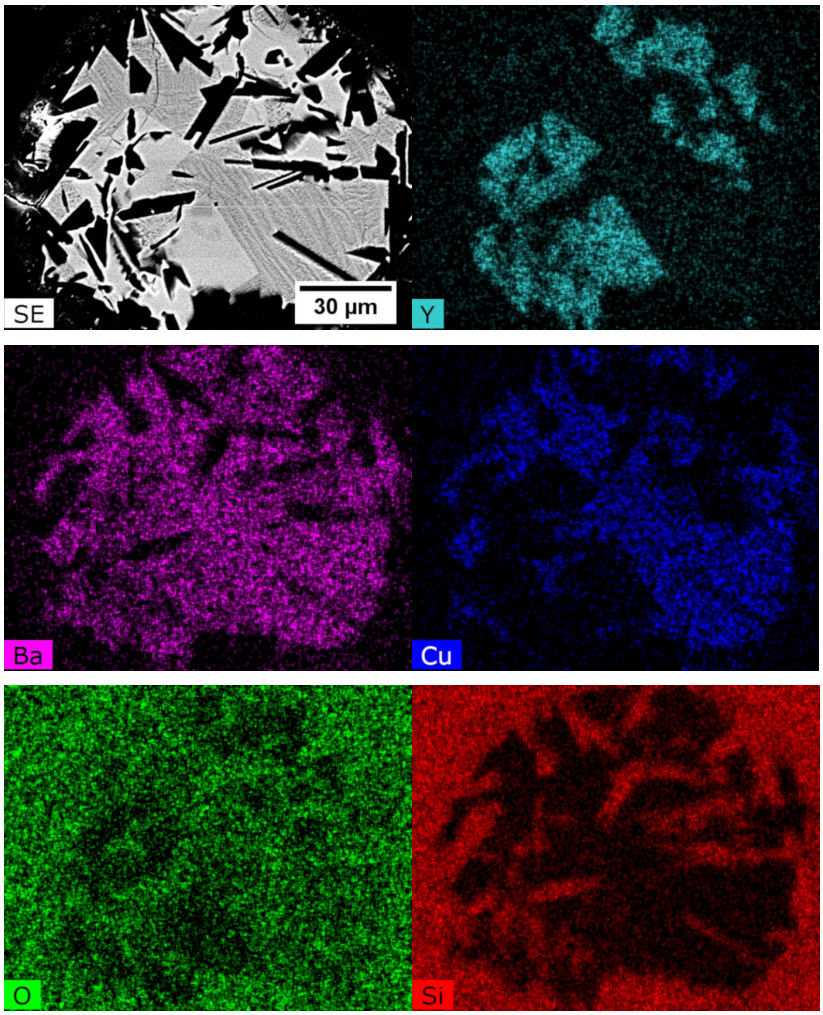

Figure 54: EDS mapping of the vacuum as-drawn YBCO core heat-treated at 1200°C for a dwelling time of 10 min in air atmosphere (scale bar 30 µm)

In order to further analyze the phases formed, EDS point analyses and XRD analyses were performed on the heat-treated fiber sections between 900°C and 1200°C. The EDS point analyses can be seen in Table 11 to Table 14, in which the different phases are circled using different colors. In addition, each table shows the phases which are likely to have formed by computing the ratios of each elemental composition while taking into consideration the overlapping/overlay of phases due to the large excitation volume of around 2 µm.

Table 11: EDS point analysis of the vacuum as-drawn YBCO core heat-treated at 900°C for a dwelling time of 10 min in air atmosphere

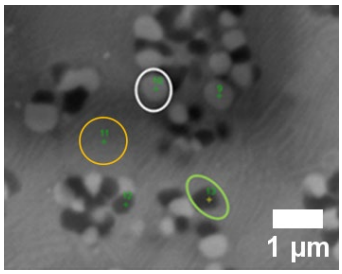

Area measured in atomic-%	Y	Ba	Cu	O	Si
White	1.0	1.5	44.6	42.2	10.7
Green	1.4	1.5	9.6	58.4	29.1
Orange	5.5	8.0	2.4	58.8	25.3

*EDS Analysis at 10 kV

White: Cu_2O formation plus SiO_2 (overlap region)

Green: mainly SiO_2

Orange: deficient in copper; consists of a lamellar structure

Table 12: EDS point analysis of the vacuum as-drawn YBCO core heat-treated at 1000°C for a dwelling time of 10 min in air atmosphere

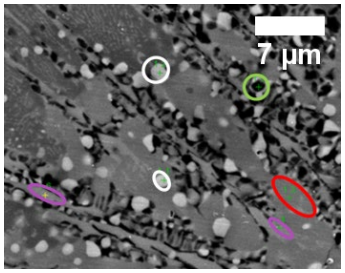

Area measured in atomic-%	Y	Ba	Cu	O	Si
White	1.3	3.3	42.5	43.4	9.5
Green	4.4	3.1	3.1	64.6	24.8
Red	0.7	13.4	2.1	59.5	24.3
Violet	9.2	6.4	2.2	64.3	17.9

*EDS Analysis at 20 kV

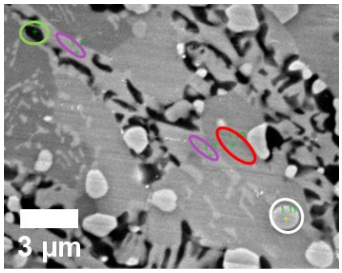

Area measured in atomic-%	Y	Ba	Cu	O	Si
White	0.0	0.2	63.5	35.3	1.0
Green	3.1	1.5	0.8	62.5	32.1
Red	0.0	11.6	1.5	59.1	27.8
Violet	10.3	5.6	0.5	62.9	20.7

*EDS analysis at 10 kV

White: mainly Cu_2O with minor SiO_2 content

Green: mainly SiO_2

Red: mainly barium silicate

Violet: yttrium barium silicate

Table 13: EDS point analysis of the vacuum as-drawn YBCO core heat-treated at 1100°C for a dwelling time of 10 min in air atmosphere

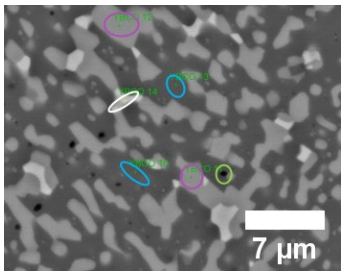

Area measured in atomic-%	Y	Ba	Cu	O	Si
White	1.4	3.9	27.5	53.0	14.2
Green	2.7	5.4	4.6	62.3	25.0
Blue	1.2	6.5	6.8	64.1	21.4
Violet	10.7	6.2	1.4	65.8	15.9

*EDS analysis at 20 kV

White: mainly Cu_2O

Green: mainly SiO_2

Blue: mainly barium copper silicate ($BaCuO_{10}Si_4$)

Violet: yttrium barium silicate ($BaY_2Si_3O_{10}$)

Table 14: EDS point analysis of the vacuum as-drawn YBCO core heat-treated at 1200°C for a dwelling time of 10 min in air atmosphere

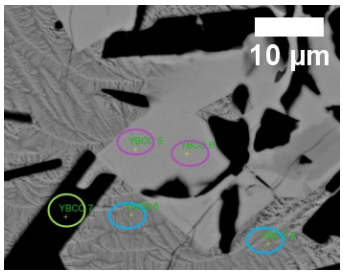

Area measured in atomic-%	Y	Ba	Cu	O	Si
Green	0.1	0.8	0.9	65.9	32.3
Blue	1.0	7.9	11.5	61.7	17.9
Violet	13.1	6.3	0.4	63.7	16.5

*EDS analysis at 20 kV
Green: mainly SiO_2
Blue: barium copper silicate (mixed state)
Violet: yttrium barium silicate ($BaY_2Si_3O_{10}$)

The results of the EDS point analyses and the EDS mapping are compared with the XRD results, which are shown in Figure 55, to provide a further quantitative analysis.

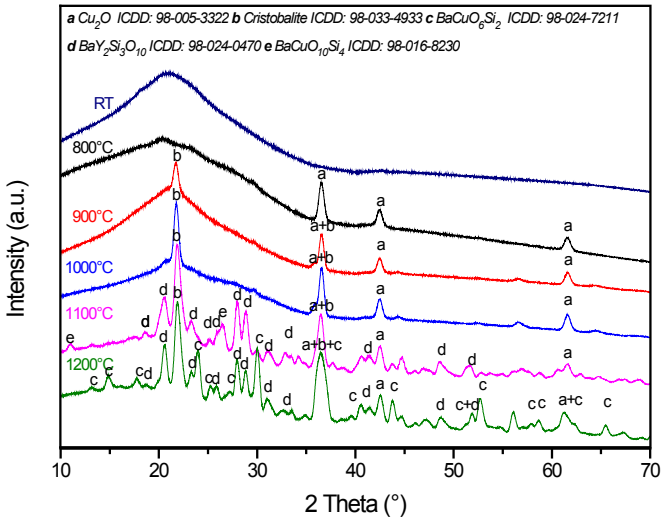

Figure 55: XRD patterns for the heat-treated vacuum as-drawn YBCO glass fibers

The XRD results show that, in addition to cuprite (peaks labeled a) and cristobalite (peaks labeled b), barium copper silicates ($BaCuSi_4O_{10}$ at 1100°C, peaks labeled e, and $BaCuSi_2O_6$ at 1200°C, peaks labeled c) and yttrium barium silicate ($BaY_2Si_3O_{10}$, peaks labeled d) crystalline phases form at 1100°C and 1200°C, which is in line with the results of the EDS analysis. In addition, Figure 56 shows the corresponding Debye-Scherrer diffraction rings. In this regard, single crystalline formations are visible, at 1100°C and 1200°C, which correspond to the $BaY_2Si_3O_{10}$ phase. Figure 55 also shows that an amorphous phase remains present even at 1200°C. Because of the persistent amorphous phase, the broadness of the peaks from the crystalline phase, and the number of phases present at the higher temperatures, Rietveld refinements to obtain phase ratios were not possible.

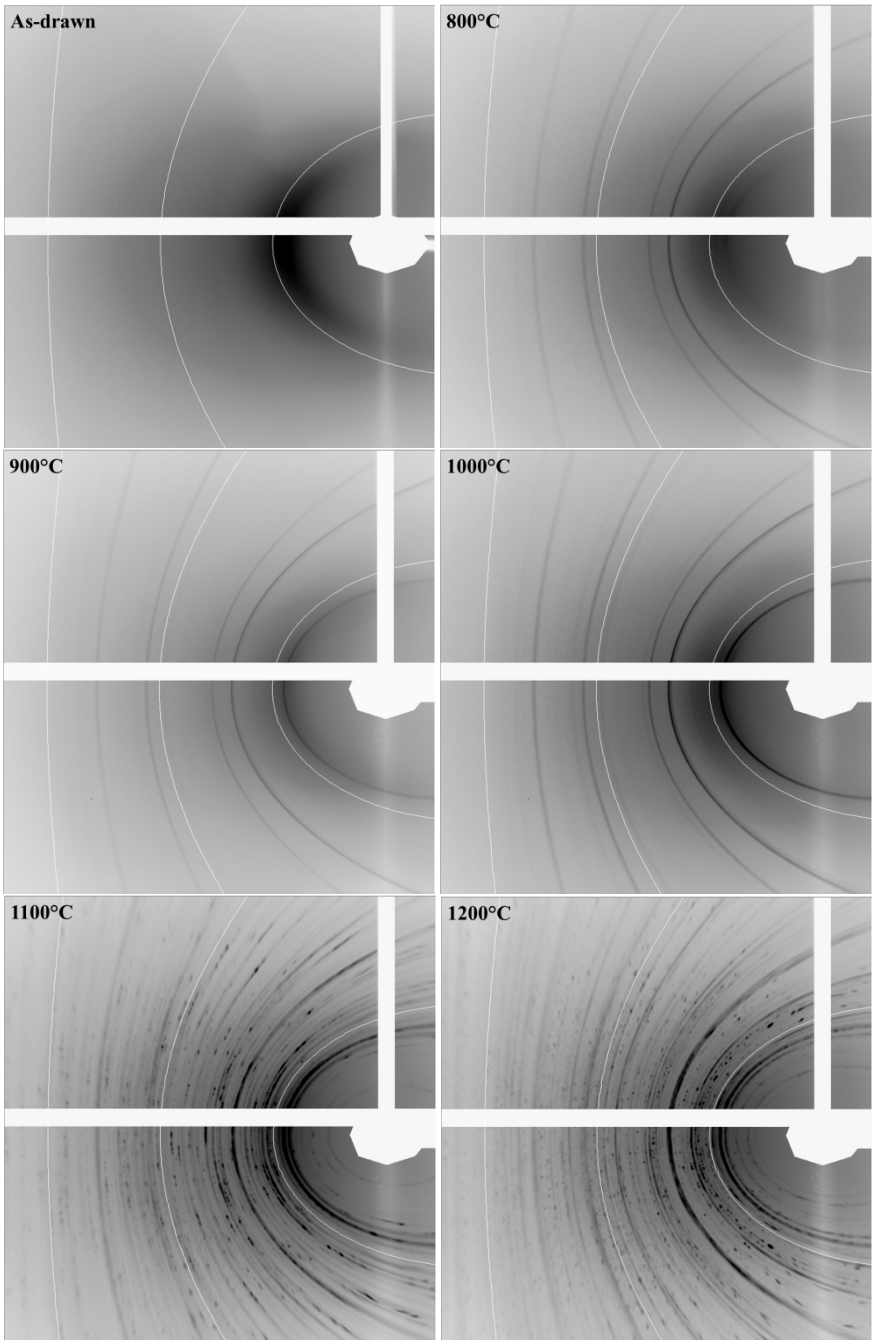

Figure 56: Debye-Scherrer diffraction ring patterns of as-drawn and heat-treated YBCO glass fiber core

The obtained barium copper silicates are known as Han blue ($BaCuSi_4O_{10}$) and Han purple ($BaCuSi_3O_6$) and were used in ancient times as blue/purple pigment colors [103]. Both silicates exhibit in their pure form a blue color. Hence, optical microscopy can also be used to detect the formation of barium copper silicates.

This is, in general, the first study on YBCO and silica, which demonstrates barium copper silicate formation as well as yttrium barium silicate formation within the YBCO-SiO_2 system.

To further study these phase formations, cross-polarized images of the YBCO core were taken on the heat-treated fiber sections. The reflection mode as well as the cross-polarized images can be seen in Figure 57.

Here, we note that cross-polarized light microscopy was performed since it can be used to identify anisotropic grains in an opaque material, due to the characteristic correlation between a certain color and its associated phase [104]. A number of works in the literature [104-108] describe the use of such a cross-polarized light study to generally determine the presence of YBCO impurity phases as well as the superconductive Y-123 phase.

The cross-polarized light study using an optical microscope, which can be seen in Figure 57, shows that, at 800°C, neither the core nor the cladding show any color of polarization, which is an indication of the existence of an isotropic structure. However, the interface layer is visible in a yellow color. At a temperature of 900°C, the co-precipitations show a red/orange color, which intensifies at 1000°C. Moreover, at 1100°C, the red color continues to be present in the center of the core. However, there is a darker blue layer present between the core (red) and the cladding region (yellow). At 1200°C, the core is entirely blue and the interface contains an orange/yellow color.

It is stated in [107] that a red color observed under cross-polarized light is a sign of Cu_2O impurity formation in YBCO. Hence, the cross-polarized imaging results confirm the formation of Cu_2O inside the core, which was also identified using the EDS and XRD analyses. Moreover, the blue color visible at 1100°C and 1200°C is an indication of barium copper silicate formation. Here, we note that the superconductive Y-123 phase would be indicated by a golden color in cross-polarized light [108]. This golden color was not observed in this cross-polarized light study, which indicates the absence of the Y-123 phase and which confirms our previous results.

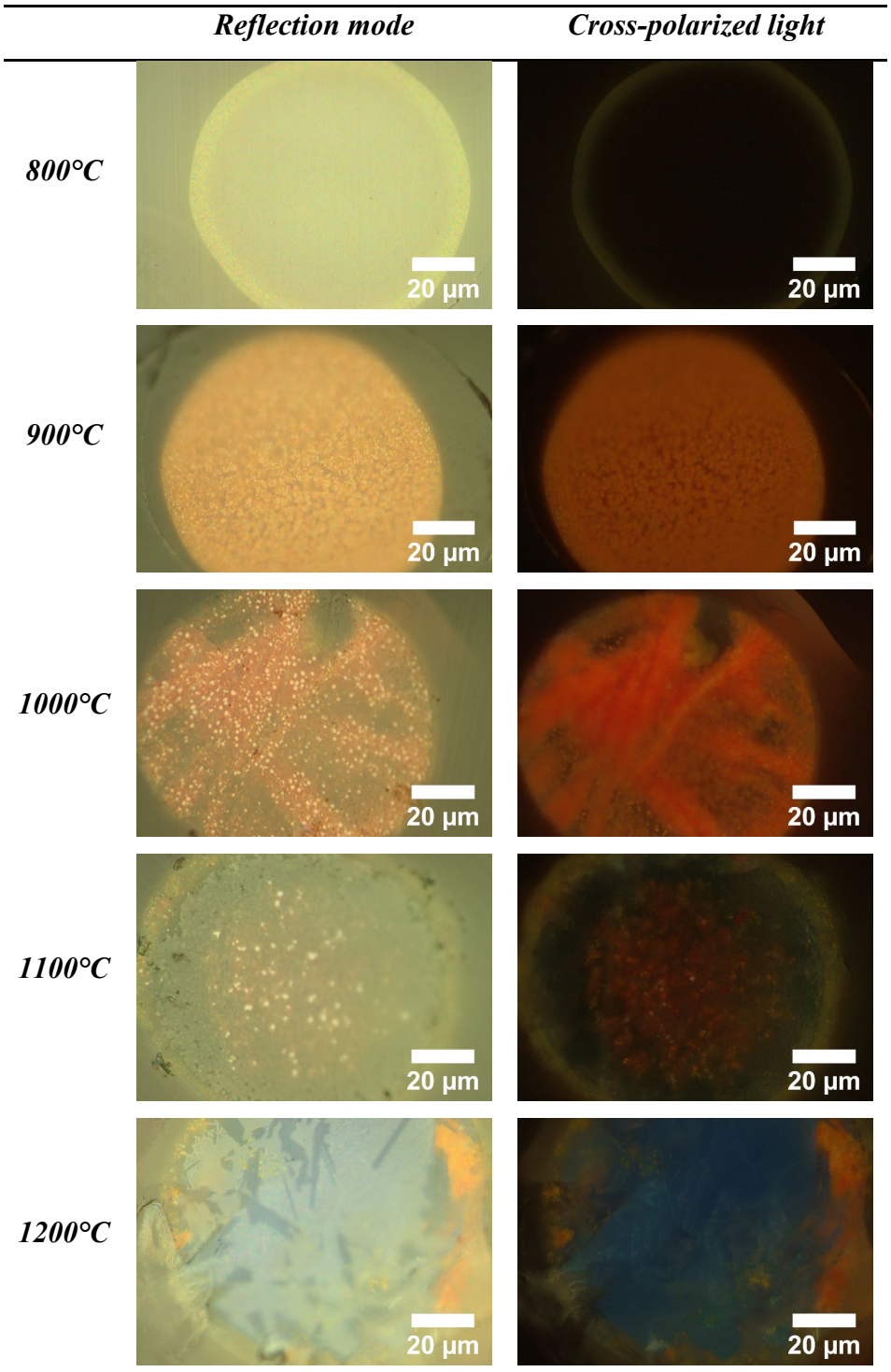

Figure 57: Optical microscope images, in reflection mode and with cross-polarized light, of YBCO fiber cross-sections heat-treated at temperatures between 800°C and 1200°C for a dwelling time of 10 min in air atmosphere

3.1.6.2 Summary and conclusion of the results obtained for heat-treated as-drawn YBCO glass fibers in air atmosphere

In summary, the additional heat-treatments on vacuum as-drawn YBCO fiber sections show that it was not possible to restore the superconductive Y-123 phase using melt-texturing techniques.

Table 15 summarizes the obtained quantitative results, by showing the phases present inside the YBCO core at the different heat-treatment temperatures.

Table 15: Phases present inside the vacuum as-drawn YBCO core at different temperatures determined using EDS point analyses combined with XRD analyses

Heat-treatment temperature	**Phases present**
800°C	Amorphous silicate phase + Cu_2O
900°C	Amorphous silicate phase + Cu_2O + cristobalite
1000°C	Amorphous silicate phase + Cu_2O + cristobalite
1100°C	Amorphous silicate phase + Cu_2O + cristobalite + $BaY_2Si_3O_{10}$ * + $BaCuO_{10}Si_4$
1200°C	Amorphous silicate phase + Cu_2O + cristobalite + $BaY_2Si_3O_{10}$* + $BaCuO_6Si_2$

*single crystal formation shown in Figure 56

Moreover, it was discovered that barium copper as well as yttrium copper silicates are formed as reaction products at elevated temperatures within the YBCO-SiO_2 system.

Furthermore, the additional heat-treatments show that further reactions within the core led to silicate formation even at a short dwelling time of 10 min. Hence, in order to investigate the possibility of recrystallizing the Y-123 from the amorphous as-drawn YBCO core, lower temperature heat-treatments (<1100°C) with longer dwelling times must be investigated. This investigation and the corresponding results are presented in the following section.

3.1.6.3 Heat-treated as-drawn YBCO glass fibers under flowing oxygen

Long-term oxygen heat-treatments were conducted to investigate the possibility of restoring the Y-123 phase in the as-drawn fibers. In fact, long-term oxygen heat-treatments are described in [75] to recrystallize a nearly glassy phase of YBCO into Y-123 phase. However, we note that no study can be found in the literature, which states that a fully amorphous phase can be recrystallized.

As-drawn YBCO fiber sections were heat-treated for two different heating cycles as can be seen in Figure 58.

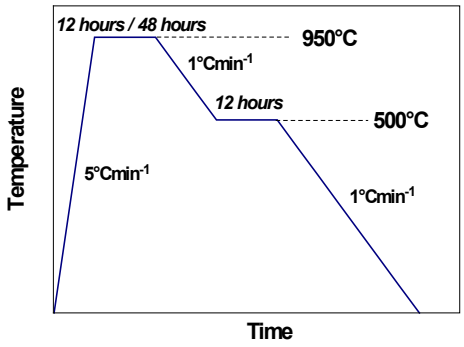

Figure 58: Heat-treatment cycles for long-term oxygen heat-treatment

The slow cooling rate of 1°Cmin^{-1} and the additional dwelling time of 12 hours at 500°C, were chosen to ensure that enough oxygen absorption occurs during the cooling process. The oxygen flow used was 0.4 SLmin^{-1}.

BSE images of the as-drawn YBCO core heat-treated in flowing oxygen for a dwelling time of 12 hours at 950°C are shown in Figure 59.

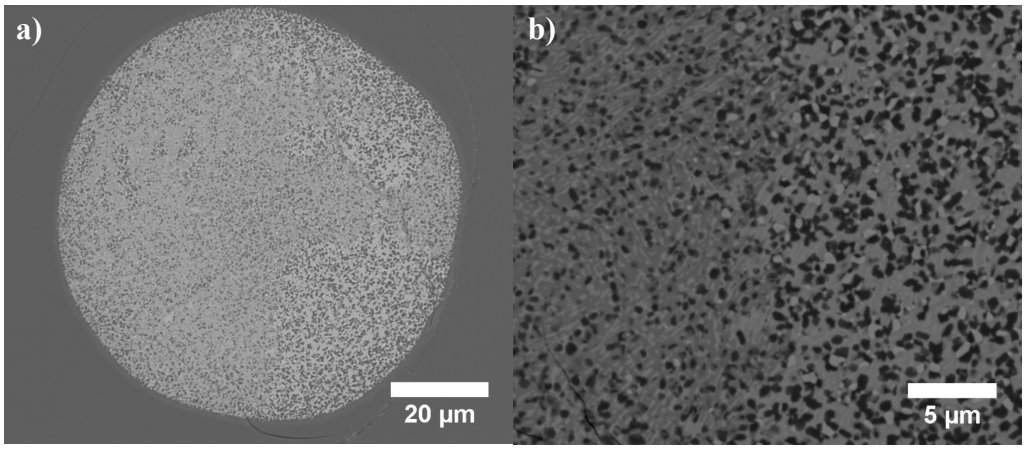

Figure 59: BSE images of heat-treated YBCO fiber sections at 950°C for 12 hours in O_2 **a)** entire YBCO fiber core and **b)** higher magnification image of the YBCO fiber core

As can be seen in Figure 59, the entire core shows a morphology similar to those of the heat-treated YBCO fiber sections in air atmosphere shown in Section 3.1.6.1. An EDS line-scan was performed on the YBCO core to determine whether the overall silicon content inside the YBCO core increased, which would imply further diffusion between the YBCO core and the silica cladding

during the prolonged heat-treatment dwelling time at 950°C. The EDS line-scan is shown in Figure 60.

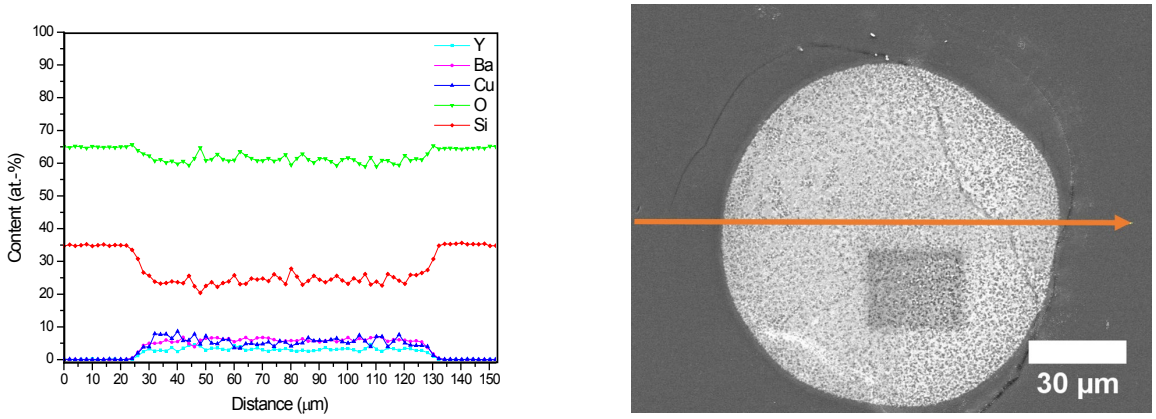

Figure 60: EDS line-scan of the oxygen heat-treated YBCO fiber section for a dwelling time of 12 hours at 950°C

Figure 60 shows that the silicon content inside the core changed marginally as compared to the as-drawn YBCO glass fibers shown in Figure 25.

In addition, the XRD pattern of the oxygen heat-treated sample at 950°C for 12 hours dwelling time is shown in Figure 61 and the Debye-Scherrer diffraction ring pattern can be seen in Figure 62.

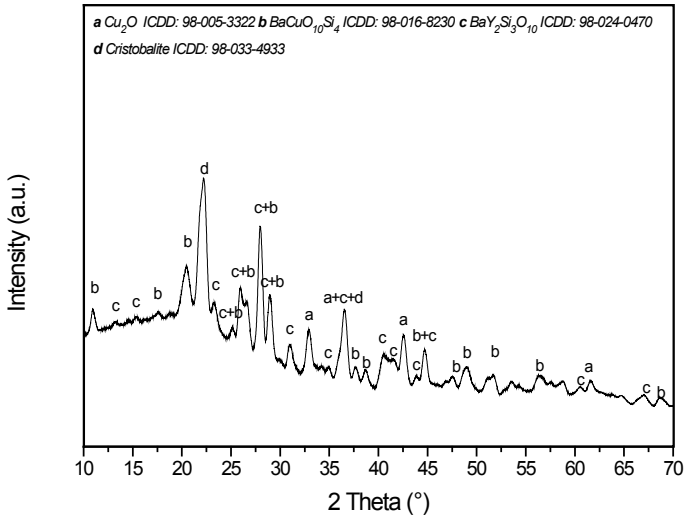

Figure 61: XRD-pattern of the oxygen heat-treated YBCO fiber section for a dwelling time of 12 hours at 950°C

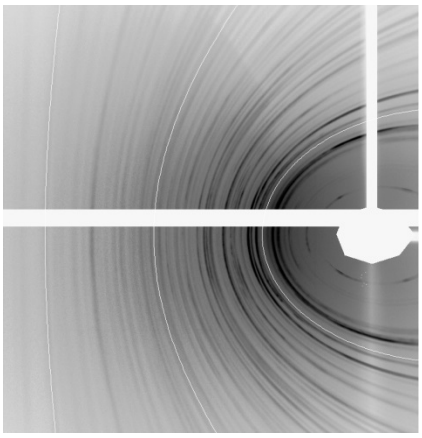

Figure 62: Debye-Scherrer diffraction ring pattern of the oxygen heat-treated YBCO fiber section for a dwelling time of 12 hours at 950°C

The XRD pattern in Figure 61 shows that restoring the Y-123 phase was not possible. The phases formed are indexed to belong to Cu_2O, cristobalite, $BaY_2Si_3O_{10}$ and the oxygen-rich $BaCuO_{10}Si_4$. The optical microscope images in Figure 63 show blueish and red colors in the cross-polarized light, which correspond to $BaCuO_{10}Si_4$ and Cu_2O formation. In addition, Figure 63 shows that no homogeneous phase formation occurred.

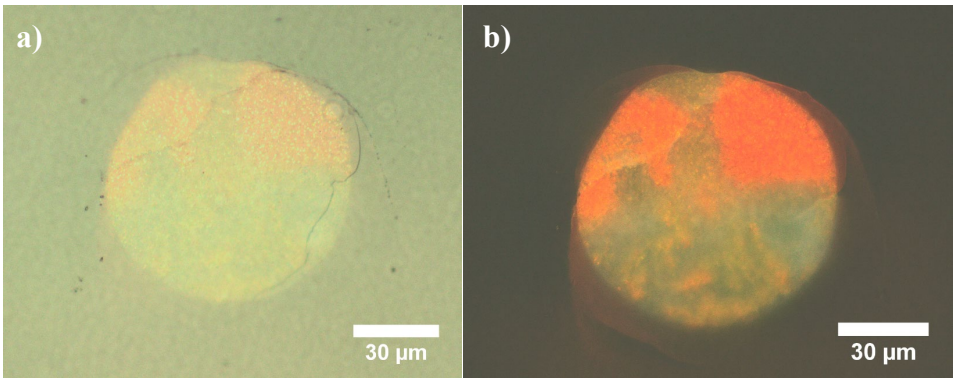

Figure 63: Optical microscope images of the oxygen heat-treated YBCO fiber section for a dwelling time of 12 hours at 950°C; **a)** reflection mode, **b)** cross-polarized light

In general, based on its amorphous glassy core, the as-drawn fiber exhibits a dense structure, which hinders the oxygen diffusion during the heat-treatment. Therefore, a second YBCO fiber section was heat-treated using the same heating cycle, shown in Figure 58, but using a dwelling time of 48 hours instead of 12 hours. SEM images of the YBCO fiber section after the heat-treatment are shown in Figure 64 and the EDS line-scan can be seen in Figure 65.

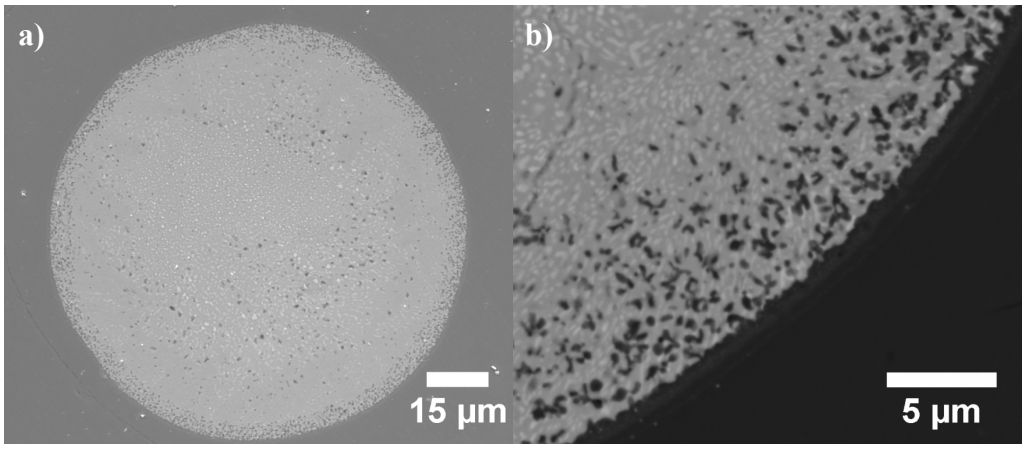

Figure 64: SEM images of the heat-treated YBCO fiber sections at 950°C for 48 hours in O_2 **a)** Secondary electron (SE) image of entire YBCO fiber core and **b)** BSE higher magnification image of the YBCO fiber core

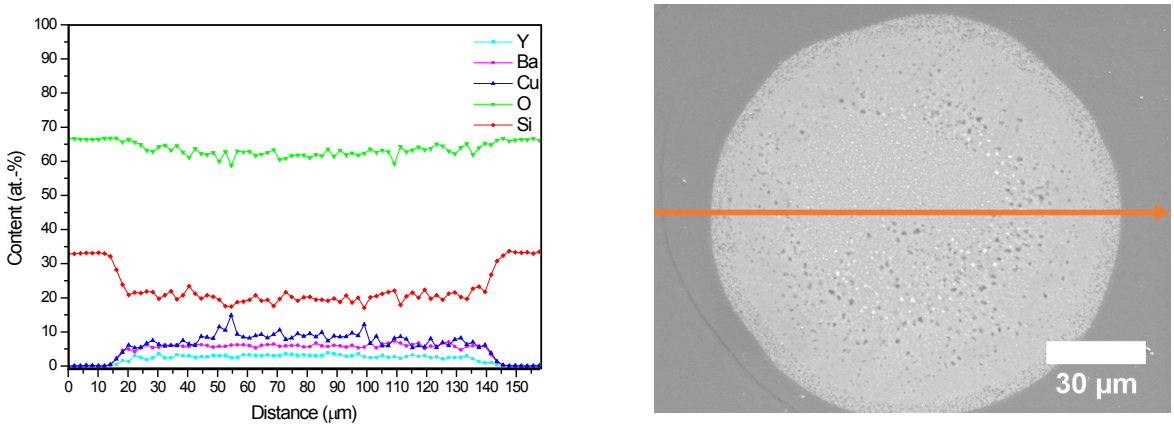

Figure 65: EDS line-scan of the oxygen heat-treated YBCO fiber section for a dwelling time of 48 hours at 950°C

The morphology of the YBCO core, in Figure 64, is similar to that of the sample heat-treated in air at 1100°C (shown in Figure 45). Furthermore, the EDS line-scan in Figure 65 does not show any further silicon diffusion inside the core. In order to analyze the phases formed, EDS point analysis and XRD analysis were performed. The EDS point analysis can be seen in Table 16.

Table 16: EDS point analysis of the oxygen heat-treated YBCO fiber section for a dwelling time of 48 hours at 950°C

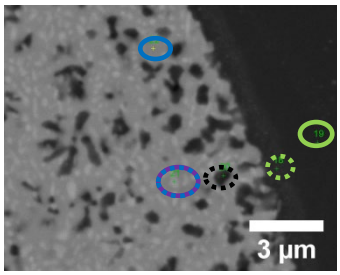

Area measured in atomic-%	Y	Ba	Cu	O	Si
Green	0.0	0.0	0.1	69.0	30.9
Green dotted	0.1	0.4	0.7	67.7	31.1
Black dotted	1.1	1.7	2.1	64.1	31.0
Blue	0.9	5.0	5.8	61.8	26.5
Violet/Blue	5.2	3.8	3.6	63.6	23.8

*EDS analysis at 20 kV
Green: SiO_2
Blue: barium copper silicate ($BaCuSi_4O_{10}$)
Violet/Blue: yttrium barium silicate ($BaY_2Si_3O_{10}$ + $BaCuSi_4O_{10}$)
Black dotted: mixed phases due to overlap

The XRD pattern and the Debye-Scherrer diffraction ring pattern of the oxygen heat-treated fiber section with a 48 hours dwelling time are shown in Figure 66 and Figure 67, respectively.

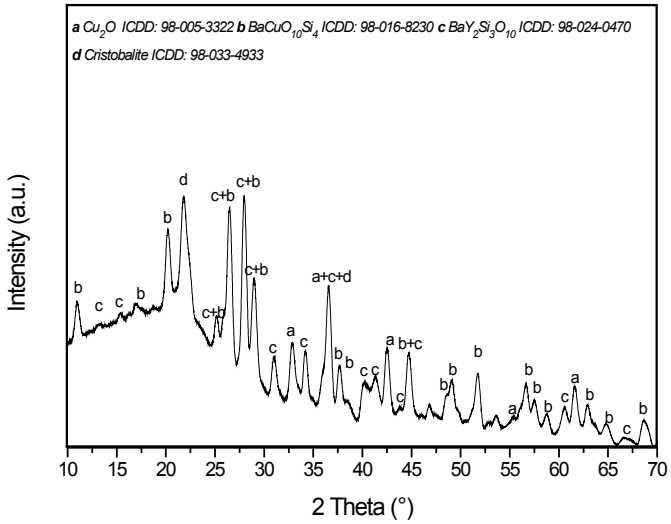

Figure 66: XRD-pattern of the oxygen heat-treated YBCO fiber section for a dwelling time of 48 hours at 950°C

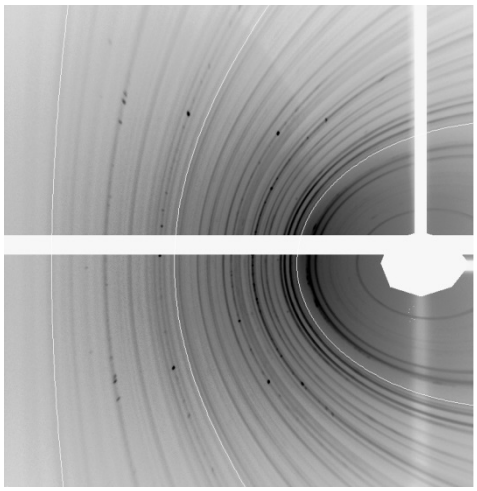

Figure 67: Debye-Scherrer diffraction ring pattern of the oxygen heat-treated YBCO fiber section for a dwelling time of 48 hours at 950°C

The EDS point analysis as well as the XRD analysis show a similar phase formation as compared to the as-drawn YBCO fiber section heat-treated for 12 hours, instead of 48 hours, at 950°C. However, at a dwelling time of 48 hours, single crystal formation of the Cu_2O phase occurred, as can be seen in Figure 67, as well as an increase in intensity of the barium copper silicate phase.

Optical microscope images were taken of the 48 hours fiber section in reflection as well as in cross-polarized mode and are shown in Figure 68.

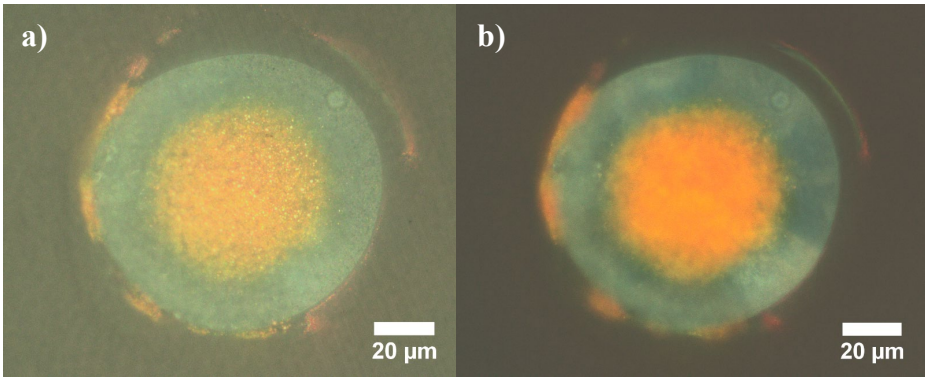

Figure 68: Optical microscope images of the oxygen heat-treated YBCO fiber section for a dwelling time of 48 hours at 950°C; **a)** reflection mode, **b)** cross-polarized light

As shown in Figure 68, the blue color of the oxygen-rich barium copper silicate forms an outer phase layer inside the core region. Whereas, the center of the core shows a mixed phase. Hence, it is expected that longer heat-treatments will transform the entire core region into barium copper silicate and yttrium barium silicate.

3.1.6.4 Summary and conclusion of the results obtained for heat-treated as-drawn YBCO glass fibers under flowing oxygen

In summary, it was shown that long oxygen heat-treatments at lower temperatures (<1100°C) do not lead to the formation/recrystallization of the Y-123 in the drawn YBCO fibers. Moreover, it was shown that barium copper and yttrium barium silicate form at lower temperatures (950°C), as compared to the air heat-treated as-drawn YBCO fiber sections, after a prolonged heating. Hence, this supports the conclusion that barium copper silicate and yttrium barium silicate are the stable phases in the YBCO-SiO_2 system at the lower temperatures.

3.1.7 *Summary*

This section has presented the first reported success in drawing YBCO glass fibers using a fiber draw tower and have shown the occurrence of dissolution and diffusion based reactions between the YBCO core and the silica cladding. In this regard, we have provided an in-depth analysis of these reactions, presented a novel phase separation analysis within the glass-forming YBCO-SiO_2 system and investigated the possibility of reducing the occurring reactions and mitigating their effects. The performed analyses have considered draws in vacuum and in oxygen atmospheres, different cladding materials (fused silica and borosilicate) and different preform designs. In addition, the conducted analyses have also considered as-drawn fibers as well as heat-treated fibers in different atmospheres, temperatures and dwelling times.

Moreover, different preform designs (shown in Figure 20) were drawn and analyzed using SEM imaging and EDS analyses. However, the obtained fiber sections showed that the variations in the preform design had no effect on reducing the dissolution and diffusion based reactions between the YBCO core and the silica cladding.

In order to further analyze the reactions within the YBCO-SiO_2 system and to draw further conclusions regarding phase relations therein, Sections 3.2 and 3.3 provide additional analyses focusing on YBCO+SiO_2 pellets, heat-treated in air and oxygen atmospheres, as well as rapid thermal annealing experiments, with a subsequent quenching step, on YBCO+SiO_2 rods and YBCO powder inserted in a fused silica tube.

3.2 Phase relations within $YBa_2Cu_3O_{7-x}$ + SiO_2 pellets

This section focuses on $YBa_2Cu_3O_{7-x}$+SiO_2 pellets heat-treated in air as well as in oxygen atmospheres in order to generate further conclusions regarding the phase relations within the YBCO-SiO_2 system.

3.2.1 *Objective and procedure*

In order to investigate the effect of the silica content on the superconductivity of YBCO and investigate the underlying phase relations, YBCO powder (SCI Engineered Materials 99.99% purity) was pressed into 1g pellets using a cold isostatic press by adding 0 at.-% (pure YBCO pellet), 20 at.-%, 33.33 at.-% or 50 at.-% amorphous silica powder (99.9% Alfa Aesar), respectively. The mold used for the cold isostatic pressing was self-made by using latex rubber tubing (5234K23) and high-temperature pull-through round plugs (2903K22) from McMaster-Carr. The pellets were heat-treated at 900°C to 1200°C in air using a muffle furnace, Barnstead Type 1500. In addition, heat-treatments at 900°C to 1100°C were performed under flowing oxygen with the rate of 0.2 $SLmin^{-1}$ using a standard tube furnace, MTI Corporation Model GSL-1100X. The heating and cooling rates were set to 5°$Cmin^{-1}$ and the used dwelling time was 30 min (for both heat-treatment atmospheres). In addition, the crucible used is a piece of high purity alumina (99.8%) tubing from CoorsTek. Furthermore, YBCO powder was used as a barrier layer between the YBCO pellet and the alumina crucible. Following this method, no detectable impurity formation occurred between alumina and the pellet. Due to the partial melting of YBCO at around 1002°C (as shown in Table 1), the pellets begin to form a liquid phase above this temperature. The liquid that is formed wets and corrodes the alumina crucible. Hence, long dwelling times cannot be used in this study, due to the wetting and corrosion issues, which prevent the possibility of determining equilibrium phases at these elevated temperatures. Therefore, long heat-treatments were solely performed at 900°C for dwelling times of 12 hours and seven days in air atmosphere.

In order to characterize the heat-treated pellets, the pellets were polished with silicon carbide grinding paper down to a grit size of P4000. Their crystal structure was determined using XRD analyses on a PANalytical powder X-Ray diffraction instrument using Cu-K_α-radiation. HighScore Plus was used for Rietveld refinement analysis in order to determine the phases present after the heat-treatment. Furthermore, the heat-treated pellets in air atmosphere were characterized with an

environmental scanning electron microscope, FEI Quanta 600 FEG. Energy dispersive spectroscopy for chemical composition point analysis and mapping were performed using an attached Bruker QUANTAX 400 Energy Dispersive X-Ray Spectrometer with a high speed Silicon Drifted Detector at an accelerating voltage of 20.0 kV.

In general, this study is the first to analyze YBCO powder with silica powder addition at elevated temperatures above 1000°C. In this regard, the goal of this study is to identify the phases formed after heat-treatments in air and in O_2 atmosphere using XRD and EDS analyses, as well as to determine the effect of the silica addition on the superconductivity of YBCO. As previously mentioned, due to the YBCO material wetting and corroding the crucible material, prolonged dwelling times to investigate the equilibrium phases between YBCO and silica at elevated temperatures are not feasible. However, this study serves as a first investigation of phase relations between YBCO and silica at elevated temperatures.

3.2.2 *Results on YBCO/SiO_2 pellets heat-treated in air atmosphere*

First, pure YBCO pellets were characterized in order to be used as a reference. The pure YBCO pellets were heat-treated between 900°C and 1200°C for a dwelling time of 30 min in air atmosphere with heating and cooling rates of 5°Cmin^{-1}. These pellets were, then, analyzed using XRD and EDS on the SEM. The XRD patterns of the pure YBCO pellets are shown Figure 69.

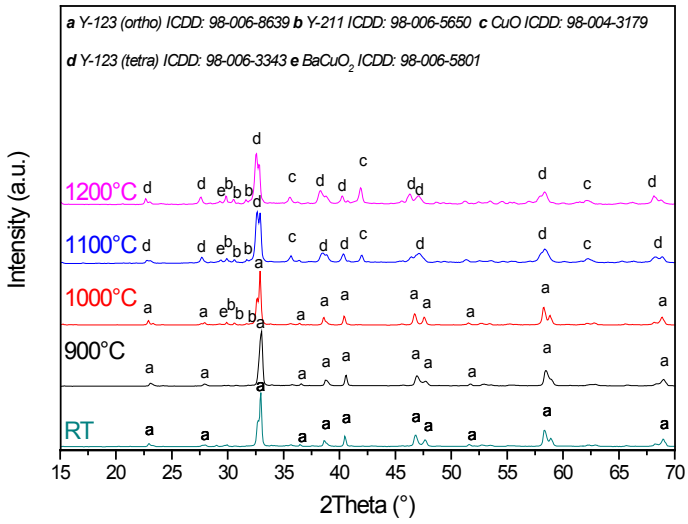

Figure 69: XRD patterns of the pure YBCO pellets heat-treated at 900°C, 1000°C, 1100°C and 1200°C for a dwelling time of 30 min in air atmosphere

It can be seen in Figure 69 that the Y-123 phase still exists from room temperature up to 1200°C. However, due to the eutectic and peritectic reactions within the YBCO system, as shown in Table 1, second phases form such as Y-211, CuO and $BaCuO_2$. In addition, due to the heat-treatment in air, the oxygen deficient tetragonal Y-123 phase forms above 1000°C. To further analyze the obtained composition, SEM analyses were performed on the heat-treated pure YBCO pellets. The BSE images can be seen in Figure 70.

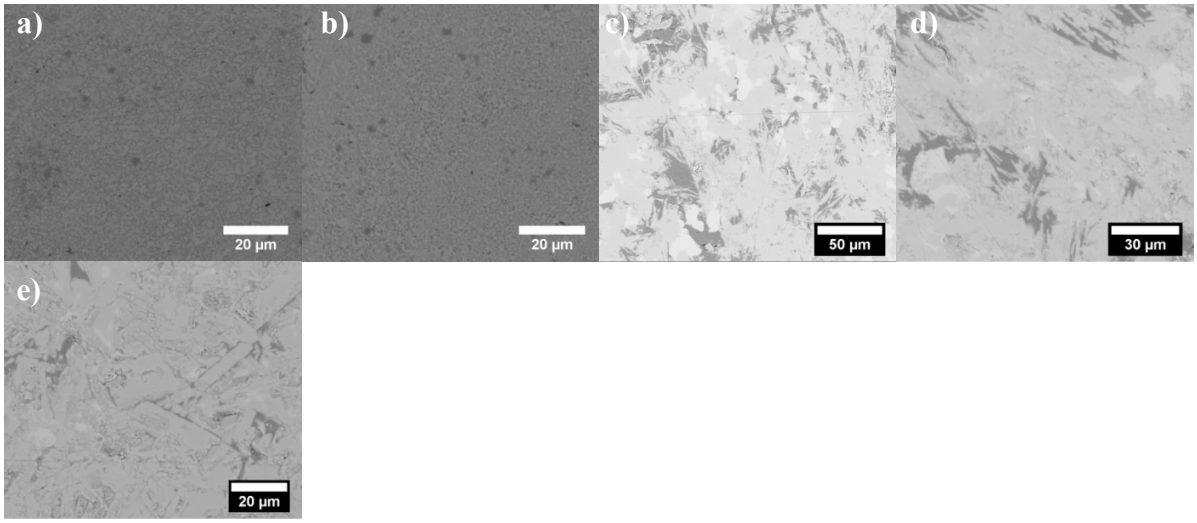

Figure 70: BSE images of the pure YBCO pellets at **a)** room temperature and heat-treated at **b)** 900°C, **c)** 1000°C, **d)** 1100°C and **e)** 1200°C for 30 min dwelling time in air atmosphere

The BSE images in Figure 70 show, due to their Z-contrast imaging ability, the formation of second phases during the heat-treatment process.

To further analyze the phases present, EDS point analyses were performed. The results can be seen in Table 17. The oxygen content in all EDS point analyses show a lower value as theoretically expected. It should be noted that roughness of the surface can lead to the loss of characteristic X-Rays of low energy X-ray exhibiting elements, such as oxygen. The EDS results, shown in Table 17, confirm the obtained XRD results for all heat-treated pure YBCO pellets.

Table 17: EDS point analysis of the pure YBCO pellets at **a)** room temperature and after heat-treatments at **b)** 900°C, **c)** 1000°C, **d)** 1100°C and **e)** 1200°C for 30 min dwelling time in air atmosphere

a)

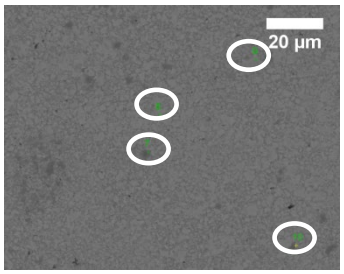

Area measured in atomic-%	Y	Ba	Cu	O
White	9.0	16.6	28.7	45.7
White	9.4	17.6	27.6	45.4
White	8.4	16.5	27.6	47.5
White	8.2	15.4	27.0	49.4

White: Y-123

b)

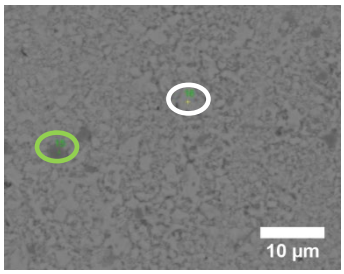

Area measured in atomic-%	Y	Ba	Cu	O
White	8.5	16.4	27.1	48.0
Green	1.4	3.3	49.6	45.7

White: Y-123
Green: CuO (overlap with Y-123 phase)

c)

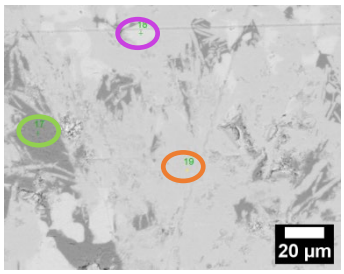

Area measured in atomic-%	Y	Ba	Cu	O
Orange	24.3	11.7	12.5	51.5
Green	0.0	0.2	55.7	44.1
Violet	0.2	23.8	27.7	48.3

Orange: Y-211
Green: CuO
Violet: $BaCuO_2$
*not visible here: Y-123 phase

d)

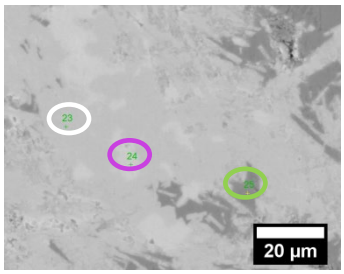

Area measured in atomic-%	Y	Ba	Cu	O
White	7.7	18.1	26.3	47.9
Green	0.0	0.3	53.4	46.3
Violet	0.0	23.5	29.1	47.4

White: Y-123
Green: CuO
Violet: $BaCuO_2$
*not visible here: Y-211 phase

e)

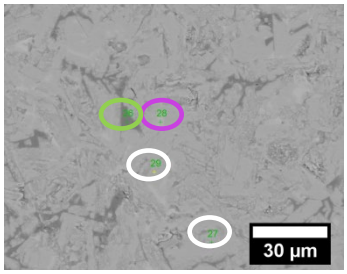

Area measured in atomic-%	Y	Ba	Cu	O
White	8.3	16.5	25.6	49.6
White	8.6	16.6	25.3	49.5
Green	0.0	0.2	52.9	46.9
Violet	0.2	22.9	27.7	49.2

White: Y-123
Green: CuO
Violet: $BaCuO_2$
*not visible here: Y-211 phase

In the following step, the pellets with silica addition of 20 at.-%, 33.33 at.-% as well as 50 at.-% were characterized. The results are shown and analyzed next.

3.2.2.1 YBCO + 20 at.-% SiO_2 pellets

The XRD patterns of the YBCO+20 at.-% SiO_2 pellets heat-treated at 900°C to 1200°C for a dwelling time of 30 min in air atmosphere are shown in Figure 71.

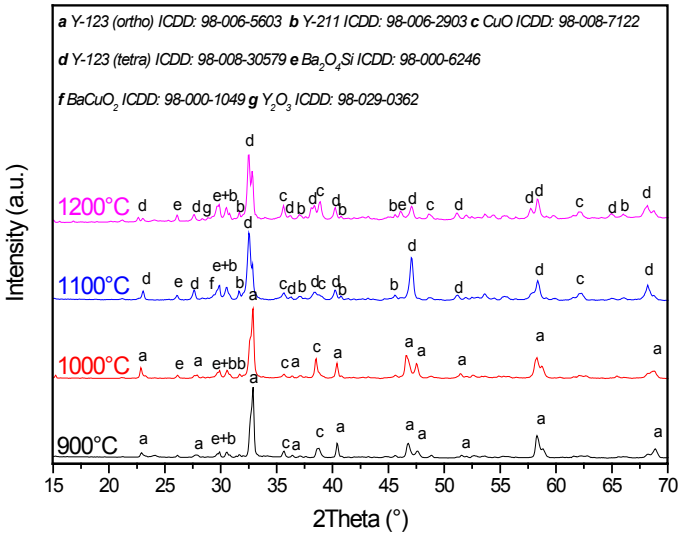

Figure 71: XRD patterns of the YBCO+20 at.-% SiO_2 pellets heat-treated at 900°C, 1000°C, 1100°C and 1200°C for a dwelling time of 30 min in air atmosphere

As shown in Figure 71, YBCO and SiO_2 react at 900°C to form barium silicate. Nonetheless, the Y-123 phase remains present at temperatures up to 1200°C. However, at 1100°C and 1200°C, the non-superconductive tetragonal phase of Y-123 is present, as it was also the case for the pure heat-treated YBCO pellets. Furthermore, the BSE images of the morphology of the pellets can be seen in Figure 72 and the EDS point analysis is shown in Table 18.

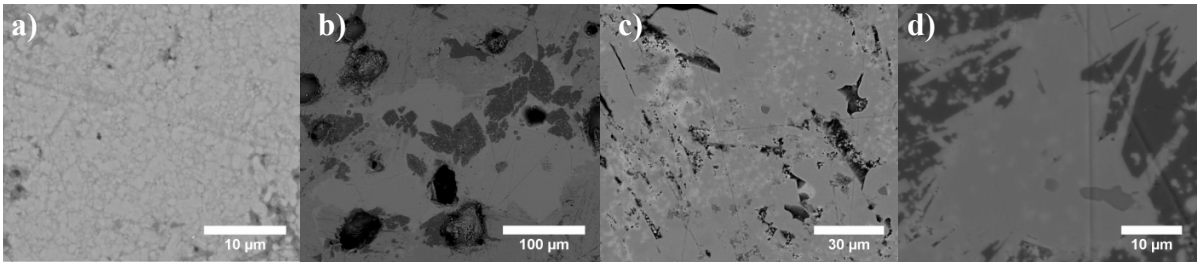

Figure 72: BSE images of the YBCO+20 at.-% SiO_2 pellets heat-treated at **a)** 900°C, **b)** 1000°C, **c)** 1100°C and **d)** 1200°C for 30 min dwelling time in air atmosphere

Table 18: EDS point analysis of the YBCO+20 at.-% SiO_2 pellets at **a)** 900°C, **b)** 1000°C, **c)** 1100°C and **d)** 1200°C for 30 min dwelling time in air atmosphere

a)

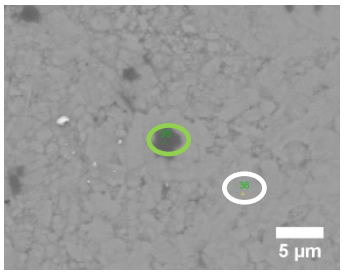

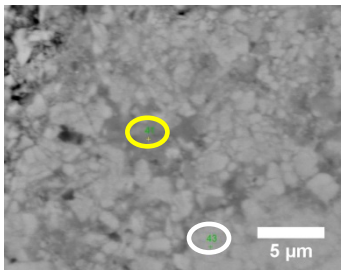

Area measured in atomic-%	Y	Ba	Cu	O	Si
White	9.1	17.6	26.8	46.5	0.0
Green	0.3	1.3	54.4	44.0	0.0
Yellow	4.9	13.8	15.8	59.6	5.9
White	8.3	16.9	26.7	48.1	0.0

White: Y-123
Green: CuO (overlap with Y-123 phase)
Yellow: Ba_2SiO_4 (overlap with Y-123 phase)

b)

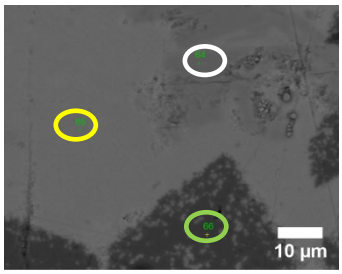

Area measured in atomic-%	Y	Ba	Cu	O	Si
White	8.9	17.5	28.7	44.9	0.0
Yellow	0.0	28.6	18.1	47.9	5.4
Green	0.0	0.9	57.2	41.8	0.1

White: Y-123
Green: CuO
Yellow: Ba_2SiO_4 + $BaCuO_2$

c)

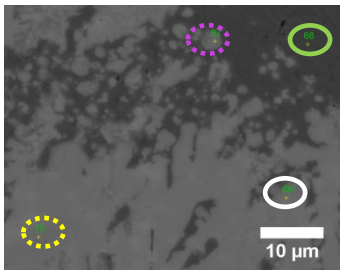

Area measured in atomic-%	Y	Ba	Cu	O	Si
Violet dotted	22.0	10.6	16.9	50.5	0.0
Green	0.1	0.9	53.8	45.0	0.2
White	5.4	22.2	18.7	48.5	5.2
Yellow dotted	24.5	11.9	14.0	49.6	0.0

Violet dotted: Y-211 + overlap with CuO phase
Green: CuO
White: Y-123 + Ba_2SiO_4
Yellow dotted: Y-211

d)

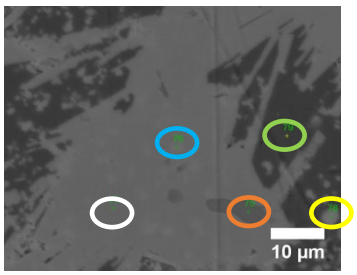

Area measured in atomic-%	Y	Ba	Cu	O	Si
Orange	51.5	0.5	1.7	46.2	0.1
Blue	4.0	29.1	12.7	46.1	8.1
Green	0.0	0.2	60.0	39.8	0.0
White	26.8	13.2	15.3	44.7	0.0
Yellow	0.0	34.3	7.0	46.8	11.9

Orange: Y_2O_3
Blue: Y-123 + Ba_2SiO_4
Green: CuO
White: Y-211
Yellow: Ba_2SiO_4 + $BaCuO_2$

The EDS point analysis in Table 18, as well as the EDS mapping shown in Appendix 2, show that barium silicate formation occurs at the barium copper oxide rich liquid phase regions and form CuO and Ba_2SiO_4 upon cooling. Furthermore, Y_2O_3 forms at 1200°C, which is detectable using the XRD as well as the EDS analyses. The formation of the Y_2O_3 phase at 1200°C is an indication that the addition of silica reduces the temperature of the peritectic reactions. Indeed, this was also reported in [9] to occur for the peritectic melting of the Y-123 phase into the Y-211 phase and the liquid phase below 1000°C. In addition, as shown in Figure 72, the morphology of the pellets is more porous as compared to the pure YBCO pellets, which can stem from the silica powder addition.

3.2.2.2 YBCO + 33.33 at.-% SiO_2 pellets

The XRD patterns of the YBCO+33.33 at.-% SiO_2 pellets heat-treated at 900°C to 1200°C for a dwelling time of 30 min in air atmosphere are shown in Figure 73.

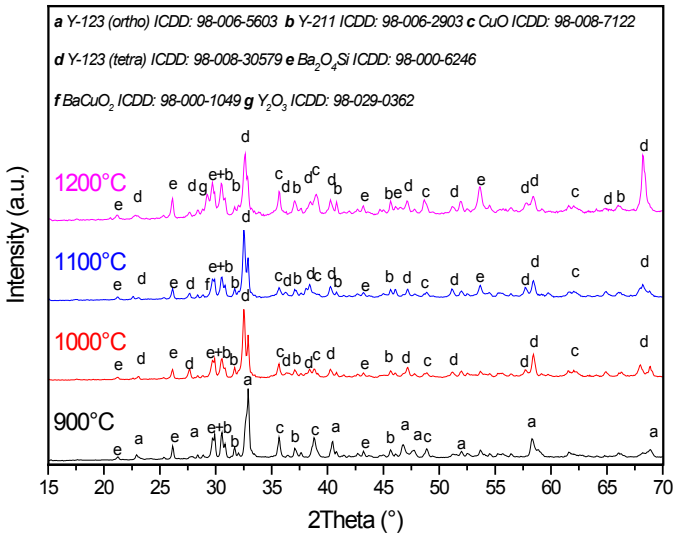

Figure 73: XRD patterns of the YBCO+33.33 at.-% SiO_2 pellets heat-treated at 900°C, 1000°C, 1100°C and 1200°C for a dwelling time of 30 min in air atmosphere

Figure 73 shows that, above 900°C, the tetragonal Y-123 phase forms. Furthermore, the XRD patterns in Figure 73 show an increase in the 100% intensity peak of the barium silicate phase, at a 2 Theta angle of around 29.5°, as compared to the 100% intensity peak of the Y-123 phase, at a 2 Theta angle of 32.9° (orthorhombic Y-123) and 32.5° (tetragonal Y-123). To confirm this change in phase formation, Rietveld refinement results will be presented and analyzed in Section 3.2.2.4.

Furthermore, the BSE images of the YBCO+33.33 at.-% SiO_2 pellets are shown in Figure 74 and the EDS point analysis is shown in Table 19.

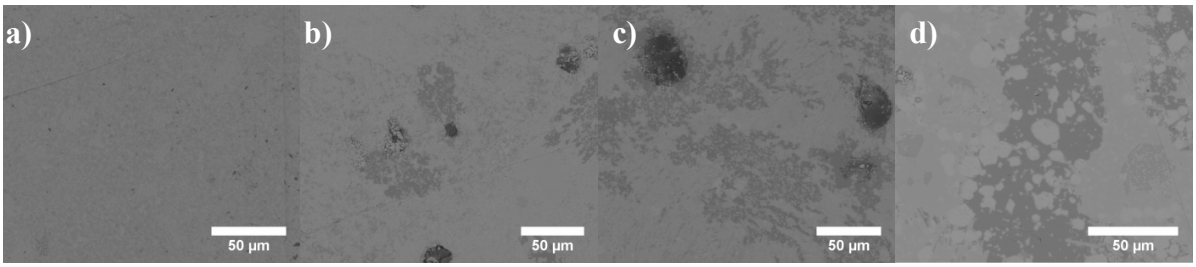

Figure 74: BSE images of the YBCO+33.33 at.-% SiO_2 pellets heat-treated at **a)** 900°C, **b)** 1000°C, **c)** 1100°C and **d)** 1200°C for 30 min dwelling time in air atmosphere

As shown in Table 19, the YBCO+SiO_2 pellet heat-treated at 900°C still shows pure unreacted silica particles, which is an indication of a moderate reaction rate of YBCO and silica at 900°C. The high silicon content areas, which are detectable at 900°C and 1000°C, can stem from the polishing process using the silicon carbide grinding paper, as it is unlikely that they are caused by a strong reaction process between the silica powder and the YBCO powder. In addition, the XRD analyses do not show crystalline silicon formation.

Table 19: EDS point analysis of the YBCO+33.33 at.-% SiO_2 pellets at **a)** 900°C, **b)** 1000°C, **c)** 1100°C and **d)** 1200°C for 30 min dwelling time in air atmosphere

a)

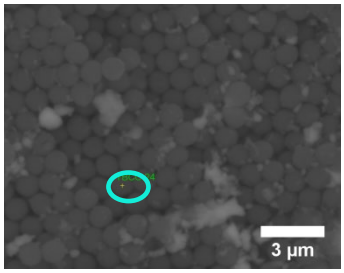

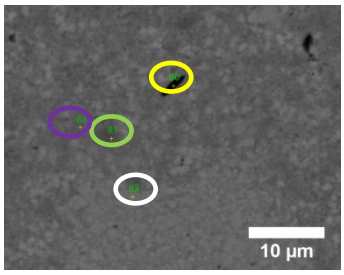

Area measured in atomic-%	Y	Ba	Cu	O	Si
Turquoise	0.1	0.1	0.2	63.6	36.0
Green	1.6	5.2	45.3	46.3	1.6
Yellow	3.4	6.3	13.1	17.1	60.1
White	8.8	16.4	27.5	47.3	0.0
Violet	8.3	5.9	37.8	47.4	0.6

Turquoise: un-reacted SiO_2 particles 1 µm diameter
White: Y-123
Green: CuO (overlap with Y-123 and Ba_2SiO_4 phases)
Yellow: Silicon-rich region (overlap with Y-123 phase)
Violet: Y-211 + CuO

b)

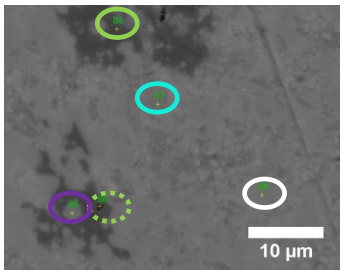

Area measured in atomic-%	Y	Ba	Cu	O	Si
Turquoise	11.0	21.2	15.3	48.5	4.0
Green dotted	0.0	3.4	53.6	41.4	1.6
Green	0.2	1.5	55.8	42.1	0.4
White	7.2	23.2	17.9	47.0	4.7
Violet	8.9	17.7	22.2	44.9	6.3

Turquoise: undefined
Green dotted: CuO + Ba_2SiO_4
Green: CuO + Ba_2SiO_4
White: Y-123 + Ba_2SiO_4
Violet: Y-123+ Silicon-rich region
*not visible here: Y-211 phase

c)

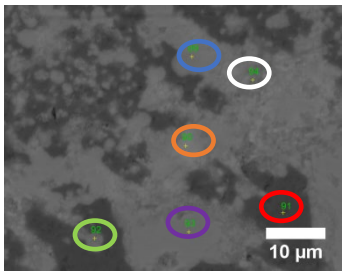

Area measured in atomic-%	Y	Ba	Cu	O	Si
Green	21.1	11.3	19.4	48.2	0.0
Orange	0.2	35.6	2.2	48.7	13.3
White	11.6	16.2	19.9	50.8	1.5
Blue	20.1	14.6	17.8	47.5	0.0
Violet	26.5	12.8	15.7	45.0	0.0
Red	0.0	0.2	58.9	40.9	0.0

Green: Y-211 + CuO
Orange: CuO + Ba_2SiO_4
White: Y-123 + Ba_2SiO_4
Blue: Y-211/Y-123
Violet: Y-211
Red: CuO

d)

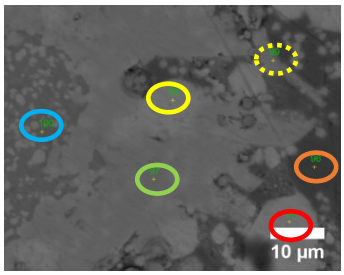

Area measured in atomic-%	Y	Ba	Cu	O	Si
Yellow	0.0	33.7	1.2	51.9	13.2
Green	25.7	12.3	13.6	48.4	0.0
Yellow dotted	8.0	17.9	29.1	44.9	0.1
Blue	47.6	0.5	0.3	51.4	0.2
Orange	0.0	0.2	55.0	44.8	0.1
Red	0.0	34.1	1.8	50.9	13.2

Yellow: Ba_2SiO_4 + minor CuO
Green: Y-211
Yellow dotted: Y-123
Blue: Y_2O_3
Orange: CuO
Red: Ba_2SiO_4 + minor CuO

3.2.2.3 YBCO + 50 at.-% SiO_2 pellets

The XRD patterns of the YBCO+50 at.-% SiO_2 pellets heat-treated at 900°C to 1200°C for a dwelling time of 30 min in air atmosphere are shown in Figure 75.

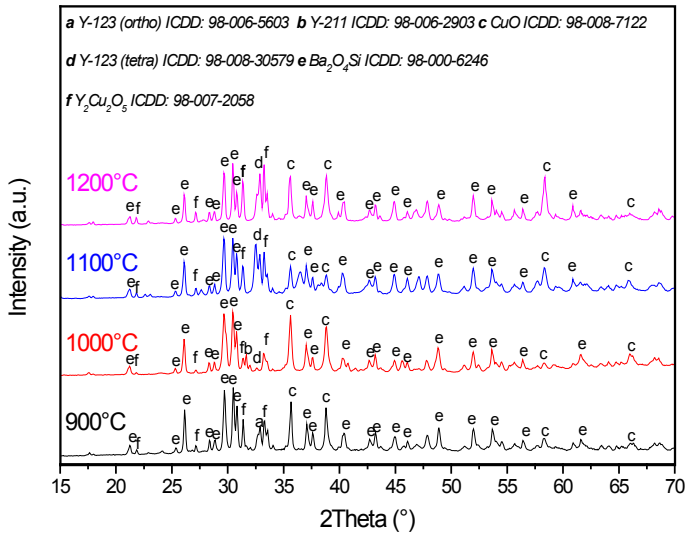

Figure 75: XRD patterns of the YBCO+50 at.-% SiO_2 pellets heat-treated at 900°C, 1000°C, 1100°C and 1200°C for a dwelling time of 30 min in air atmosphere

The XRD patterns, in Figure 75, no longer show a clear Y-123 phase, which is an indication of a strong reaction between silica and YBCO. Due to the high silica content, nearly all of the Y-123 phase reacted with silica to form barium silicate and yttrium copper oxide. To further analyze these results, BSE images of the heat-treated YBCO+50 at.-% SiO_2 pellets are shown in Figure 76 and EDS point analysis is shown in Table 20.

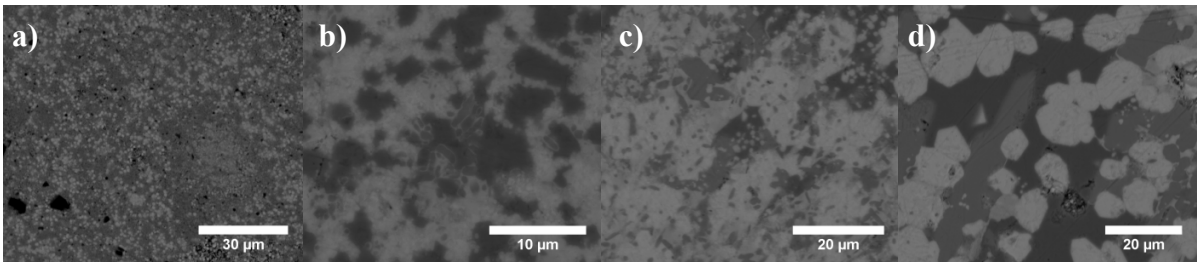

Figure 76: BSE images of the YBCO+50 at.-% SiO_2 pellets heat-treated at **a)** 900°C, **b)** 1000°C, **c)** 1100°C and **d)** 1200°C for 30 min dwelling time in air atmosphere

The EDS analysis confirms the presence of the Y-123 phase up to 1200°C in a minor quantity. However, the EDS analysis shows that the Y-123 phase is surrounded by yttrium copper oxide and the barium silicate phases, which will lead the Y-123 to decompose when further increasing the dwelling time, as will be shown in Section 3.2.2.4. The EDS mapping shown in Appendix 2 clearly illustrates the distribution of the phases.

In addition, the EDS point analysis performed on the YBCO+SiO_2 pellet heat-treated at 900°C shows a silicon-rich phase formation.

Table 20: EDS point analysis of the YBCO+50 at.-% SiO_2 pellets at **a)** 900°C, **b)** 1000°C, **c)** 1100°C and **d)** 1200°C for 30 min dwelling time in air atmosphere

a)

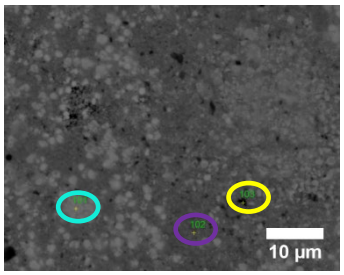

Area measured in atomic-%	Y	Ba	Cu	O	Si
Turquoise	0.8	29.3	2.8	55.1	12.0
Violet	10.8	5.5	30.9	50.6	2.2
Yellow	4.9	9.6	15.4	20.8	49.3

Turquoise: Y-123 + Ba_2SiO_4
Violet: Y-211 + CuO + Silicon-rich phase
Yellow: Y-123 + Silicon-rich phase

b)

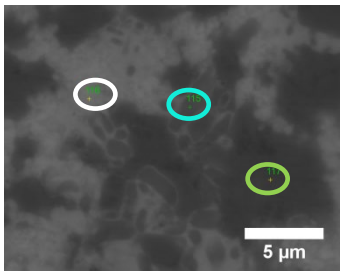

Area measured in atomic-%	Y	Ba	Cu	O	Si
Turquoise	21.4	5.7	24.5	48.0	0.4
Green	1.1	0.4	54.1	44.4	0.0
White	2.9	26.8	7.7	52.4	10.2

Turquoise: mainly $Y_2Cu_2O_5$ + Ba_2SiO_4
Green: CuO
White: Y-123+ Ba_2SiO_4

c)

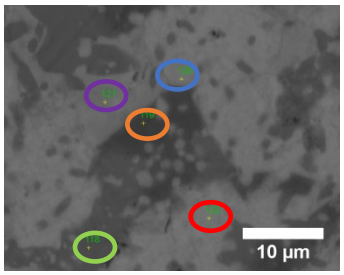

Area measured in atomic-%	Y	Ba	Cu	O	Si
Green	24.8	0.4	23.5	51.2	0.1
Orange	2.5	0.3	48.3	48.8	0.1
Blue	0.5	27.5	5.3	54.8	11.9
Violet	7.8	17.5	25.5	48.0	1.2
Red	0.0	31.5	2.2	53.1	13.2

Green: $Y_2Cu_2O_5$
Orange: mainly CuO
Blue: mainly Ba_2SiO_4 , CuO
Violet: mainly Y-123
Red: mainly Ba_2SiO_4 , CuO

d)

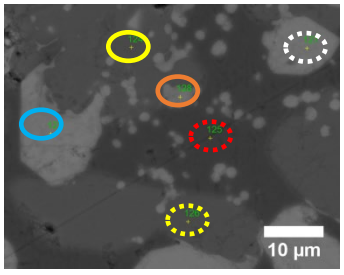

Area measured in atomic-%	Y	Ba	Cu	O	Si
Blue	0.0	33.8	1.6	51.4	13.2
Yellow	26.0	0.5	25.1	48.3	0.1
Red dotted	0.0	0.0	56.7	43.3	0.0
Yellow dotted	26.4	0.1	25.6	47.9	0.0
White dotted	0.0	33.0	2.9	50.9	13.2
Orange	1.3	28.5	8.0	50.8	11.4
Green	8.7	17.0	27.9	46.4	0.0
Red	9.0	18.0	28.5	44.5	0.0

Blue: mainly Ba_2SiO_4 , CuO
Yellow: $Y_2Cu_2O_5$
Red dotted: CuO
Yellow dotted: $Y_2Cu_2O_5$

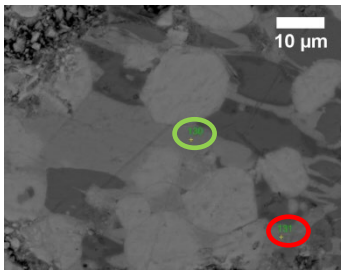

White dotted: mainly Ba_2SiO_4 , CuO
Orange: mainly Ba_2SiO_4 , CuO, Y-123
Green: Y-123
Red: Y-123

3.2.2.4 Y-123 and Ba_2SiO_4 dependence on silica content for heat-treated YBCO + SiO_2 pellets in air atmosphere

In order to investigate the effect of the silica content on the degradation of the Y-123 phase, the XRD patterns were analyzed using the HighScore Plus software. In this regard, the effect of the silica content on the decomposition of the Y-123 phase and the formation of the Ba_2SiO_4 phase, is shown in Figure 77 and Figure 78, respectively.

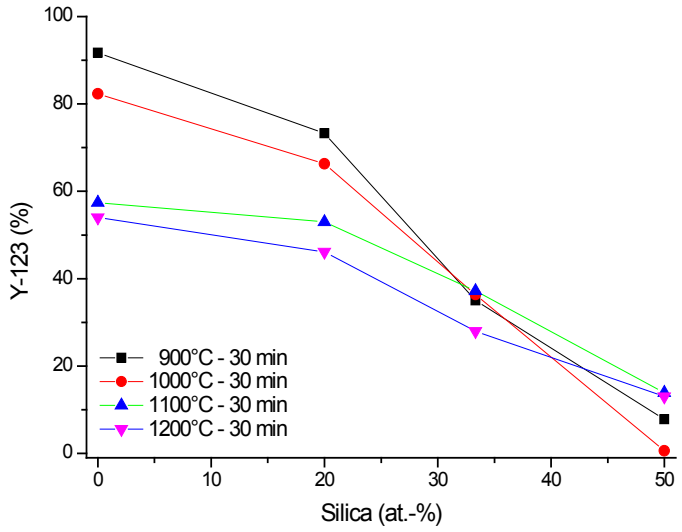

Figure 77: Effect of silica content on the decomposition of the Y-123 phase

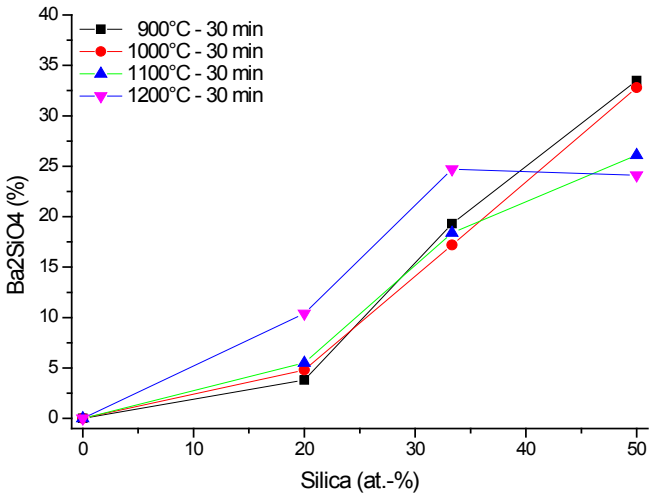

Figure 78: Effect of silica content on the formation of Ba_2SiO_4

As shown in Figure 77, an increase in the heating temperature leads to a faster degradation of the Y-123 phase for a silica content of 20 at.-%. However, with a further increase in silica content, the temperature effect on the degradation of the Y-123 phase becomes marginal, taking the error in the software analysis into consideration. In conclusion, our results show that a silica addition drastically reduces the Y-123 phase even at a short dwelling time of 30 min, which is the dwelling time used in our analyses. Moreover, Figure 78 shows that with an increase in silica content and with an increase in temperature, the formation of the barium silicate phase increases.

As mentioned earlier in Section 3.2.1, due to wetting and corrosion issues by YBCO, heat-treatments at longer dwelling times (a dwelling time of 12 hours and a dwelling time of 7 days) were only performed for a 900°C heat-treatment temperature. In this regard, Figure 79 shows that for a silica content of 20 at.-%, the 12 hours and the 7 days dwelling times lead to a faster decrease of the Y-123 phase and a faster increase of the barium silicate phase, as compared to the 30 min dwelling time. Whereas, with an addition of 33.33 at.-% silica, no strong difference in the effect on the decomposition of the Y-123 phase and the formation of the barium silicate phase can be observed between all three dwelling times. The addition of 50 at.-% silica leads, however, to a complete decomposition of the Y-123 phase for the 12 hours and 7 days dwelling times, as opposed to the case of the 30 min dwelling time. Hence, our conclusion in Section 3.2.2.3, stating that the Y-123 phase decomposes completely into barium silicate and yttrium copper oxide with an increase in dwelling time, is further confirmed.

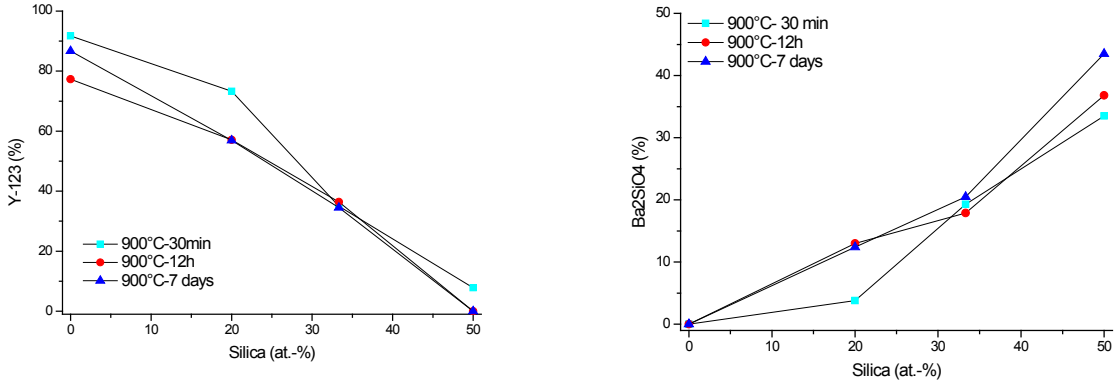

Figure 79: YBCO+20 at.-% silica pellets heat-treated in air atmosphere at 900°C-12h in air atmosphere: Effect of silica content on Y-123 phase (left) and Ba_2SiO_4 phase (right)

In general, Figure 79 indicates that the rate of the reaction between YBCO and silica increases with an increase in silica content. This implies that reactions occur after a shorter dwelling time at higher silica contents.

Moreover, as described in Section 2.5.1, the work in [10] states that after a 48 hours annealing at 900°C, YBCO and silica with a mole ratio of 1:1 still exhibit the superconductive Y-123 phase in addition to barium silicate. As such, our work on heat-treated YBCO+SiO_2 pellets for a dwelling time of 12 hours and 7 days at 900°C show that the results obtained in [10] cannot be generalized, due to the fact that in our work a mole ratio of 1:1 (YBCO:silica) led to a complete decomposition of the Y-123 phase after a 12 hours dwelling time.

In order to investigate the effect of oxygen atmosphere on the reaction of YBCO and silica within YBCO+SiO_2 pellets, heat-treatments were also performed in oxygen atmosphere. The results of these heat-treatments are presented and analyzed in the following section.

3.2.3 *Results on YBCO + SiO_2 pellets heat-treated in O_2 atmosphere*

In order to analyze the effect of the oxygen partial pressure on the reaction of YBCO and silica, YBCO+SiO_2 pellets were heat-treated in flowing oxygen and characterized, afterwards, using XRD analyses. Due to furnace restrictions, the heat-treatments were only performed up to a temperature of 1100°C. The XRD patterns of the pure reference YBCO pellets can be seen in Figure 80.

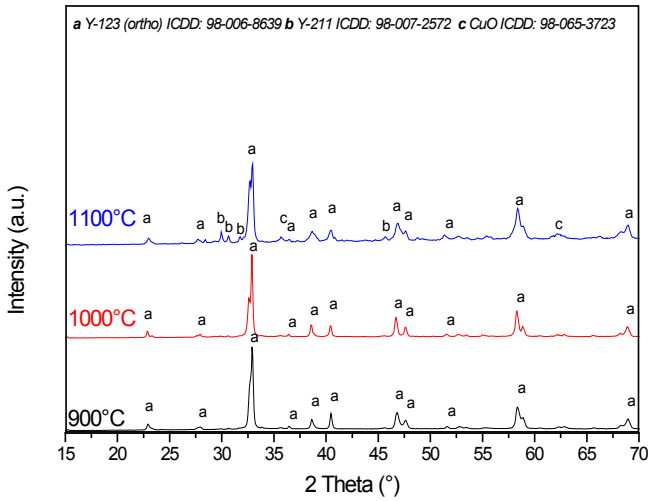

Figure 80: XRD pattern of pure YBCO pellets heat-treated at 900°C, 1000°C and 1100°C for a dwelling time of 30 min in O_2 atmosphere

Figure 80 shows that, due to the flowing oxygen, the YBCO pellet heat-treated at 1100°C resulted in the formation of the orthorhombic Y-123 phase, as opposed to the case of the air heat-treated samples. Moreover, impurity phases are visible to contain CuO as well as the green Y-211 phase for all three heat-treatment temperatures.

The XRD pattern of the YBCO + SiO_2 pellets with a silica addition of 20 at.-% are shown in Figure 81. As can be seen in Figure 81, the barium silicate phase forms at 900°C. In addition to the barium silicate formation, CuO and Y-211 phases also form. Moreover, the orthorhombic Y-123 phase transforms into the tetragonal non-superconductive phase at 1100°C, which is not the case for the pure YBCO reference pellet heat-treated at 1100°C and shown in Figure 80. As such, this indicates that the addition of silica hinders the formation of the superconductive Y-123 phase at elevated temperatures.

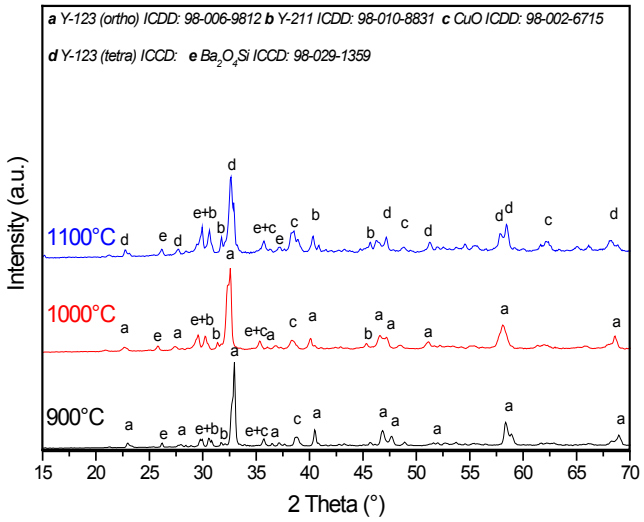

Figure 81: XRD pattern of YBCO + 20 at.-% SiO_2 pellets heat-treated at 900°C, 1000°C and 1100°C for a dwelling time of 30 min in O_2 atmosphere

Moreover, the XRD patterns of the YBCO+SiO_2 pellets with a silica addition of 33.33 at.-% are presented in Figure 82. As shown in Figure 82, an increase in the barium silicate phase occurs with a reduction in the Y-123 phase. Figure 82 shows that the CuO and Y-211 phases are also present. In addition, the Y-123 phase is present in its tetragonal non-superconductive crystal structure at 1000°C and 1100°C despite the oxygen heat-treatment. Thus, this confirms that silica hinders the orthorhombic superconductive Y-123 formation as discussed in the analysis of the oxygen heat-treated YBCO+20 at.-% SiO_2 pellets.

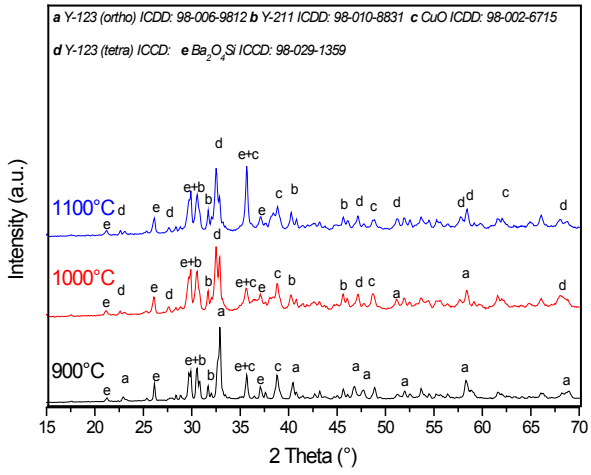

Figure 82: XRD pattern of YBCO+33.33 at.-% SiO_2 pellets heat-treated at 900°C, 1000°C and 1100°C for a dwelling time of 30 min in O_2 atmosphere

The XRD patterns of the YBCO+SiO_2 pellets with an addition of 50 at.-% silica are shown in Figure 83. The XRD patterns reveal a major barium silicate phase formation at all three temperatures in addition to a presence of CuO, $Y_2Cu_2O_5$, Y-211 and a minor Y-123 phase.

As such, our results show that an increase in the silicon content, decreases the onset temperature of the transformation from the orthorhombic crystal structure into the tetragonal crystal structure of the Y-123 phase.

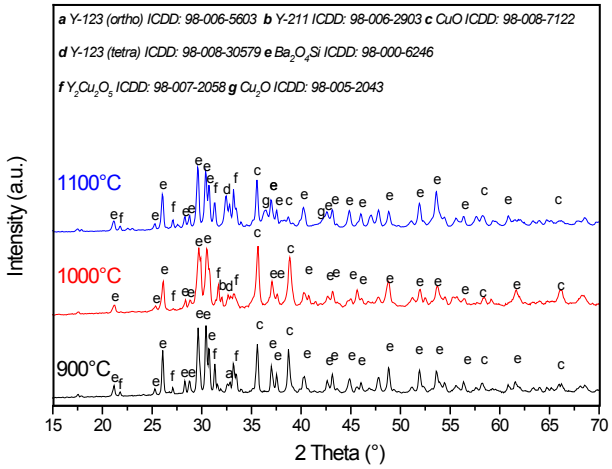

Figure 83: XRD pattern of YBCO+50 at.-% SiO_2 pellets heat-treated at 900°C, 1000°C and 1100°C for a dwelling time of 30 min in O_2 atmosphere

3.2.3.1 Y-123 and Ba_2SiO_4 dependence on the silica content for heat-treated YBCO + SiO_2 pellets in O_2 atmosphere

In order to quantitatively analyze the decomposition of the Y-123 phase and the formation of the barium silicate phase with an increase in the silica content, HighScore Plus was used to analyze the XRD patterns. In this respect, the decomposition of the Y-123 phase and the increase in the barium silicate phase, with respect to the increase in the silica content, are shown in Figure 84 and Figure 85, respectively.

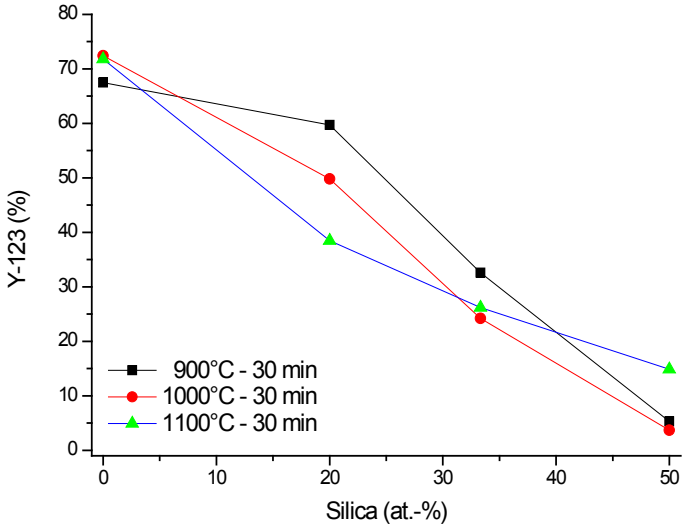

Figure 84: Effect of silica content on the decomposition of Y-123

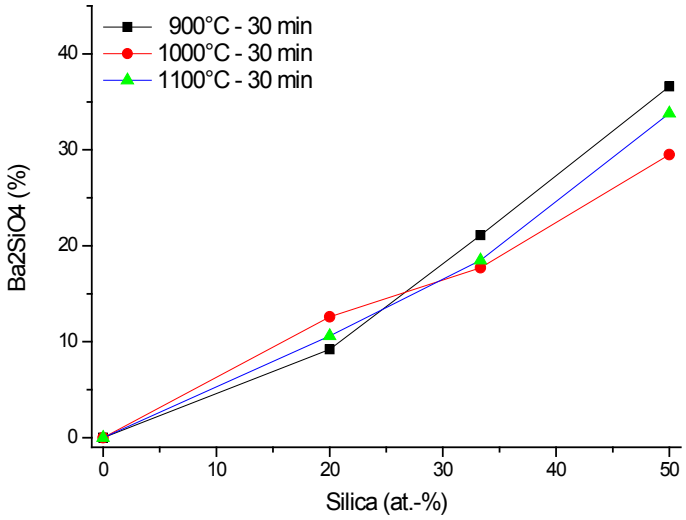

Figure 85: Effect of silica content on the formation of Ba_2SiO_4

Figure 84 and Figure 85 show the same trend in the decomposition of Y-123 and the formation of barium silicate as compared to the air samples. Hence, this indicates that the oxygen partial pressure does not have a strong effect on the overall reaction behavior of YBCO and silica powder at this temperature range.

3.2.4 *Summary of results*

In general, the characterization analysis of the YBCO+SiO_2 pellets showed that silica corrodes the Y-123 phase and forms barium silicate and yttrium copper oxide. Moreover, the oxygen heat-treatments have shown that the silica content hinders the orthorhombic Y-123 phase formation. In addition, it was shown in Section 3.2.2.3, that prolonged dwelling times lead to a complete decomposing of the Y-123 phase into barium silicate as well as yttrium copper oxide.

Furthermore, the heat-treated YBCO+SiO_2 pellets show an overall higher Y-123 content for the 1100°C and 1200°C heat-treated pellets as compared to the 900°C and 1000°C heat-treated pellets, which can stem from cooling through the first peritectic melting (as shown in Table 1), which can lead to the partial retransformation of the Y-123 phase (tetragonal crystal structure).

In summary, this analysis clearly showed that barium is the only element in the YBCO system which reacts with silica (forming barium silicate) at temperatures between 900°C and 1200°C and dwelling times of 30 min. Moreover, contrary to literature [8], which studied the reaction of YBCO and silica powder at 950°C for 5 hours dwelling time in O_2, our results show that no yttrium silicates form at temperatures between 900°C and 1200°C. In addition, this work revealed that, for a YBCO+50 at.-% silica pellet, the Y-123 phase completely decomposes after a heat-treatment at 900°C and a dwelling time of 12 hours.

Table 21 and Table 22 show a summary of all the phases that form in air and in oxygen atmosphere for the different compositions of the YBCO+SiO_2 pellets and the different heat-treatment temperatures.

In general, due to the multiphase formation, a quantitative analysis of the XRD data is highly challenging. Thus, as mentioned earlier, the Rietveld refinements obtained by analyzing the XRD patterns using the HighScore Plus software could be subject to errors.

Table 21: Reaction products in YBCO+SiO_2 pellets in air atmosphere

Temperature	YBCO pure	20 at.-% SiO_2	33.33 at.-% SiO_2	50 at.-% SiO_2
900°C-30 min	Y-123, CuO, Y-211	Y-123, CuO, Y-211, Ba_2SiO_4	Y-123, CuO, Y-211, Ba_2SiO_4, $BaCuO_2$, (amorphous SiO_2)	Y-123, CuO, Y-211, Ba_2SiO_4, $Y_2Cu_2O_5$
900°C-12 hours	Y-123, CuO, Y-211	Y-123, CuO, Y-211, Ba_2SiO_4	Y-123, CuO, Y-211, Ba_2SiO_4	CuO, Y-211, Ba_2SiO_4, $Y_2Cu_2O_5$
900°C-7 days	Y-123, CuO, Y-211	Y-123, CuO, Y-211, Ba_2SiO_4	Y-123, CuO, Y-211, Ba_2SiO_4	CuO, Y-211, Ba_2SiO_4, $Y_2Cu_2O_5$
1000°C-30 min	Y-123, CuO, Y-211, $BaCuO_2$	Y-123, CuO, Y-211, Ba_2SiO_4, $BaCuO_2$	Y-123, CuO Y-211, Ba_2SiO_4	Y-123, CuO, Y-211, Ba_2SiO_4, $Y_2Cu_2O_5$
1100°C-30 min	Y-123, CuO, Y-211, $BaCuO_2$	Y-123, CuO, Y-211, Ba_2SiO_4, CuO, $BaCuO_2$	Y-123, CuO, Y-211, Ba_2SiO_4	Y-123, CuO, Ba_2SiO_4, $Y_2Cu_2O_5$
1200°C-30 min	Y-123, CuO, Y-211, $BaCuO_2$	Y-123, CuO, Y-211, Ba_2SiO_4, $BaCuO_2$, Y_2O_3	Y-123, CuO, Y-211, Ba_2SiO_4, Y_2O_3	Y-123, CuO, Ba_2SiO_4, $Y_2Cu_2O_5$

Table 22: Reaction products in YBCO+SiO_2 pellets in O_2 atmosphere

Temperature	YBCO pure	20 at.-% SiO_2	33.33 at.-% SiO_2	50 at.-% SiO_2
900°C-30 min	Y-123, CuO, Y-211	Y-123, CuO, Y-211, Ba_2SiO_4	Y-123, CuO, Y-211, Ba_2SiO_4	Y-123, CuO, Y-211, Ba_2SiO_4, $Y_2Cu_2O_5$
1000°C-30 min	Y-123, CuO, Y-211	Y-123, CuO, Y-211, Ba_2SiO_4	Y-123, CuO, Y-211, Ba_2SiO_4	Y-123, CuO, Y-211, Ba_2SiO_4, $Y_2Cu_2O_5$
1100°C-30 min	Y-123, CuO, Y-211	Y-123, CuO, Y-211, Ba_2SiO_4	Y-123, CuO, Y-211, Ba_2SiO_4	Y-123, CuO, Y-211, Ba_2SiO_4, $Y_2Cu_2O_5$, Cu_2O

To further characterize the reactions between YBCO and silica and to further understand the reactions within YBCO glass fibers, Section 3.3 will focus on rapid thermal annealing experiments, with a subsequent quenching step, on YBCO+SiO_2 rods and on YBCO powder inside a fused silica tube.

3.3 Rapid thermal annealing analyses with subsequent quenching within the YBCO-SiO_2 system

3.3.1 *Objective and procedure*

The objective of the analyses using rapid thermal annealing experiments with a subsequent quenching step is to closely mimic the YBCO glass fiber study, to gain further insights on phase relations within the YBCO-SiO_2 system and to assess the possibility of restoring the Y-123 phase.

Rapid thermal annealing (RTA) experiments were performed on a pure YBCO rod and on a YBCO+20 at.-% silica rod with a subsequent quenching step, to possibly achieve a fully amorphous structure and to investigate possible recrystallization heat-treatments. In this regard, we investigate whether using silica, which acts as a glass former, allows achieving a fully amorphous YBCO within our experimental set-up.

A pure reference YBCO powder (SCI Engineered Materials 99.99% purity) and the YBCO+20 at.-% amorphous silica powder (99.9% Alfa Aesar) were pressed into rods using a cold isostatic press and a self-made mold. The mold consists of latex rubber tubing (5234K971) and high-temperature pull-through round plugs (2903K17), purchased from McMaster-Carr. The pressed rods were placed inside a silica tube and exposed to high temperatures using a hydrogen/oxygen torch. The molten rods were then quenched using liquid nitrogen. The quenched rods were ground into a fine powder and analyzed using XRD analysis. In order to analyze the recrystallization of the as-quenched powders, additional heat-treatments were performed at 950°C under flowing oxygen, at a 0.2 $SLmin^{-1}$ rate, using a standard tube furnace, MTI Corporation Model GSL-1100X. The heating and cooling rates were set to 5°$Cmin^{-1}$, and the used dwelling time was 84 hours. We note that a silica tube was used as crucible material during the heating process using the hydrogen/oxygen torch. The obtained results and associated analyses are presented in the following section, i.e., Section 3.3.2.

Furthermore, we also performed an RTA experiment on YBCO powder inserted inside a fused silica tube (OD:4 mm, ID: 1 mm), by using rapid thermal annealing at 1100°C for 1 hour dwelling time followed by a subsequent quenching step in air to room temperature. In this regard, after pre-heating the muffle furnace, Barnstead Thermolyne Type 47900, up to 1100°C, the fused silica tube was filled with pre-dried YBCO powder and was, then, inserted in the furnace and removed after a dwelling time of 1 hour. The furnace set-up with an inserted tube can be seen in Figure 86. The experiments were carried-out in vacuum atmosphere in order to remove any possible vapor formation and, furthermore, to mimic the vacuum drawing process at the draw tower.

Figure 86: YBCO/SiO_2 tube sample inserted vertically inside the furnace

After the RTA experiment and the quenching process, the tube was cut in half using a low speed saw. The surface of the tube was then ground and gently polished using a 220, 500, 1000, 1200, P2400 and P4000 grit paper and was, subsequently, inspected under an optical microscope. The samples were analyzed using EDS on an ESEM and using XRD analysis. The associated results will be presented and analyzed in Section 3.3.3.

3.3.2 *Quenching experiments on YBCO + SiO_2 rods inserted inside a silica tube*

The quenching experiments on pure YBCO rods and YBCO+20 at.-% silica rods inserted inside a silica tube are analyzed, next, in Sections 3.3.2.1 and 3.3.2.2, respectively.

3.3.2.1 Results for quenching a pure YBCO rod

The XRD patterns of the pure as-quenched and heat-treated YBCO rod can be seen in Figure 87.

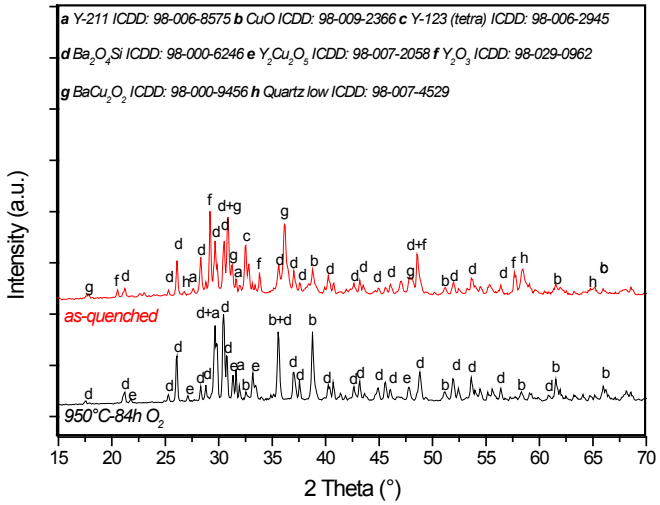

Figure 87: XRD patterns of the as-quenched (red) pure YBCO rod (red) and after a 950°C-84h O_2 heat-treatment (black)

Figure 87 shows that the as-quenched pure YBCO rod does not show any visible amorphous character and that a set of phases has formed including yttria. This shows that we were able to heat-treat the rod with the hydrogen/oxygen torch above the second peritectic melting temperature of YBCO (as shown Table 1). In addition, the XRD pattern of the as-quenched sample in Figure 87 also reveals that the silica tube, which was used as the crucible material, reacted with the molten YBCO and formed barium silicate. Hence, this leads to two observations. First, it shows that the reaction between silica and YBCO is very rapid (the melting with the hydrogen/oxygen torch lasted for around 1 minute). Second, it demonstrates that the reactions between YBCO and the fused silica tube occur even at lower temperatures, as compared to the temperatures at the draw tower. Hence, these reactions cannot be prohibited by just using glass materials with lower softening temperatures, as compared to fused silica. This corroborates our results presented in Section 3.1.4 for YBCO fibers with a borosilicate cladding. Moreover, Figure 87 shows that the Y-123 phase decomposes after the additional heat-treatment at 950°C for 84 hours in oxygen atmosphere.

Furthermore, in order to analyze the phase distribution for the as-quenched and the heat-treated pure YBCO rod, the XRD patterns shown in Figure 87 were analyzed using the HighScore Plus software. Figure 88 shows the volume percentages of the phases present.

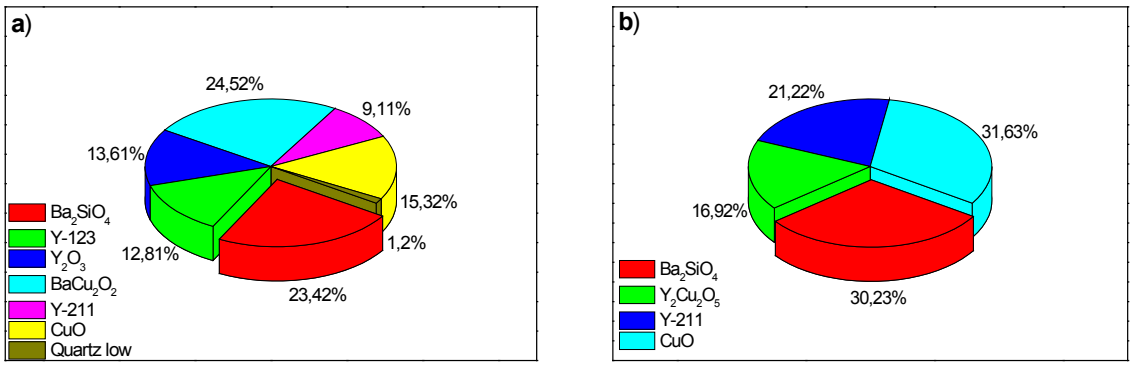

Figure 88: Volume percentages of the phases formed for the a) as-quenched pure YBCO rod and b) heat-treated as quenched pure YBCO rod

As shown in Figure 88, the barium silicate phase (in red) increases in vol.-% after the heat-treatment. In this regard, Y-123, Y_2O_3, $BaCu_2O_2$ and quartz phases reacted during the oxygen heat-treatment to form $Y_2Cu_2O_5$, Y-211, CuO and Ba_2SiO_4.

Next, the results for the YBCO+20 at.-% silica rod are introduced and analyzed.

3.3.2.2 Results for quenching a YBCO + 20 at-% silica rod

Figure 89 shows the XRD patterns of the as-quenched and the heat-treated YBCO+20 at.-% SiO_2 rod.

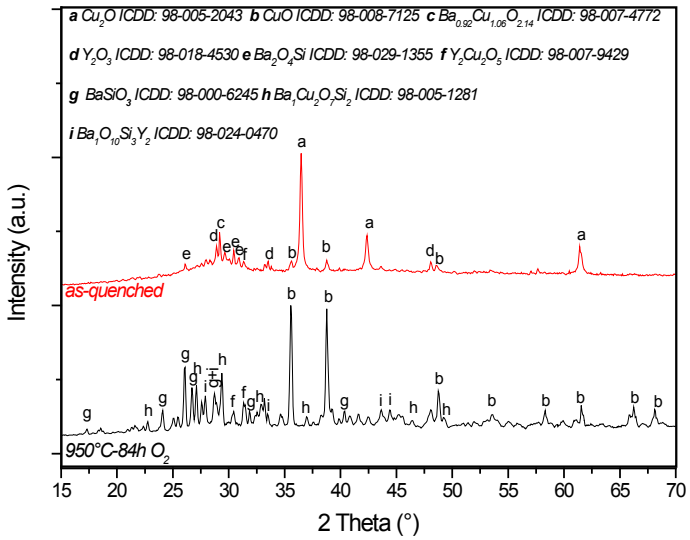

Figure 89: XRD patterns of the as-quenched YBCO+20 at.-% SiO_2 rod (red) and after a 950°C-84h O_2 heat-treatment (black)

As shown in Figure 89, an amorphous phase formed in addition to Cu_2O and some minor phases. This indicates that silica inside the core can, indeed, act as a glass former. In addition, due to the strong amorphous background of the as-quenched rod, only the volume percentages for the heat-treated rod are shown in Figure 90. These results are obtained by analyzing the XRD pattern of the heat-treated rod using the HighScore Plus software.

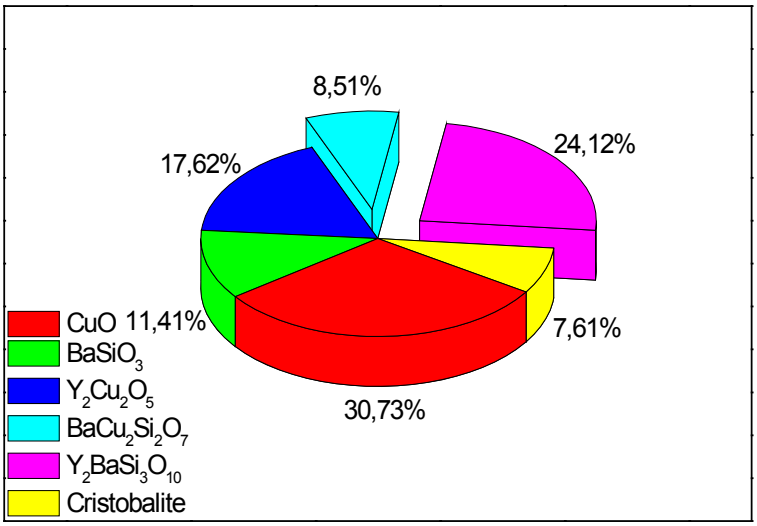

Figure 90: Pie chart of heat-treated as-quenched YBCO+20 at.-% silica rod

Figure 90 shows that the higher silicon/silica content inside the quenched rod led to barium copper as well as yttrium barium silicate formation, which corroborates our fiber analysis results in Section 3.1. Moreover, the results in Figure 89 and Figure 90 show that no Y-123 phase can be obtained in the presence of a high silica content, and that barium copper silicate and yttrium barium silicate are stable phases forming inside the YBCO-SiO_2 system, which further confirms our results presented in Section 3.1.

In the next step, rapid thermal annealing on a pure YBCO powder inside a silica tube was performed and the results are shown next.

3.3.3 *Rapid thermal annealing and quenching of pure YBCO powder inside a silica tube*

The objective of this experiment is to further analyze the diffusion and dissolution process within the YBCO-SiO_2 system by using a rapid thermal annealing at 1100°C for 1 hour dwelling time

followed by a subsequent quenching step. The EDS line-scan of the polished YBCO/SiO_2 tube cross-section is shown in Figure 91 and the EDS mapping is presented in Figure 92.

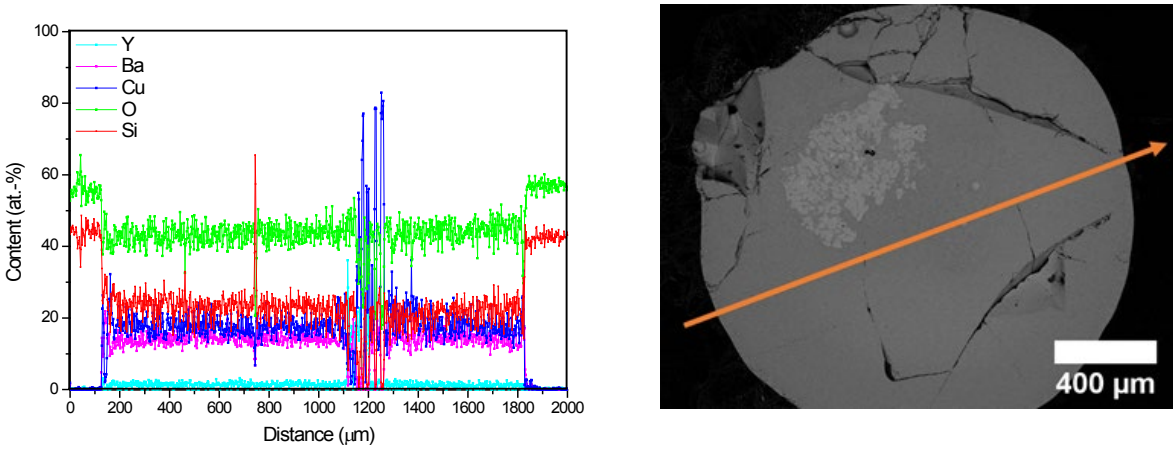

Figure 91: EDS line-scan of the rapid thermally annealed YBCO/SiO_2 tube at 1100°C for 1h dwelling time with a subsequent quenching step

Figure 91 shows that silicon is present inside the entire core region with a similar atomic percentage as compared to the fiber samples in Section 3.1. Moreover, the core diameter increased from 1 mm to around 1.7 mm, which indicates a dissolution of the fused silica tube. As such, this confirms the conclusion made in Section 3.1.2, stating that no out-diffusion of the core material can be visible as the interface moves outwards with the dissolution of the fused silica cladding.

In order to determine the phases that form inside the core, an EDS point analysis was conducted on the areas shown in the secondary electron (SE) image in Figure 92. The EDS point analysis results are shown in Table 23. As can be seen in Table 23, as well as in the phase contrast of the EDS mapping in Figure 92, different phase regions are present. The main phases inside the core can be determined to belong to Y_2O_3, Cu_2O, $Y_2BaSi_3O_{10}$ and $BaCuSi_2O_6$. Furthermore, Figure 91 shows that the dominant phases inside the core are $Y_2BaSi_3O_{10}$ and $BaCuSi_2O_6$. This result is of paramount importance to our work, as it allows concluding that the stable phases inside the YBCO-SiO_2 system are $Y_2BaSi_3O_{10}$ and barium copper silicate, whose composition changes depending on the oxygen content.

Regarding the results in Table 23, we note that, as discussed in Section 3.2.2, the oxygen content in all EDS point analyses show a lower value than theoretically expected, as the roughness of

the sample can lead to the loss of characteristic X-Rays of low energy X-ray exhibiting elements, such as oxygen.

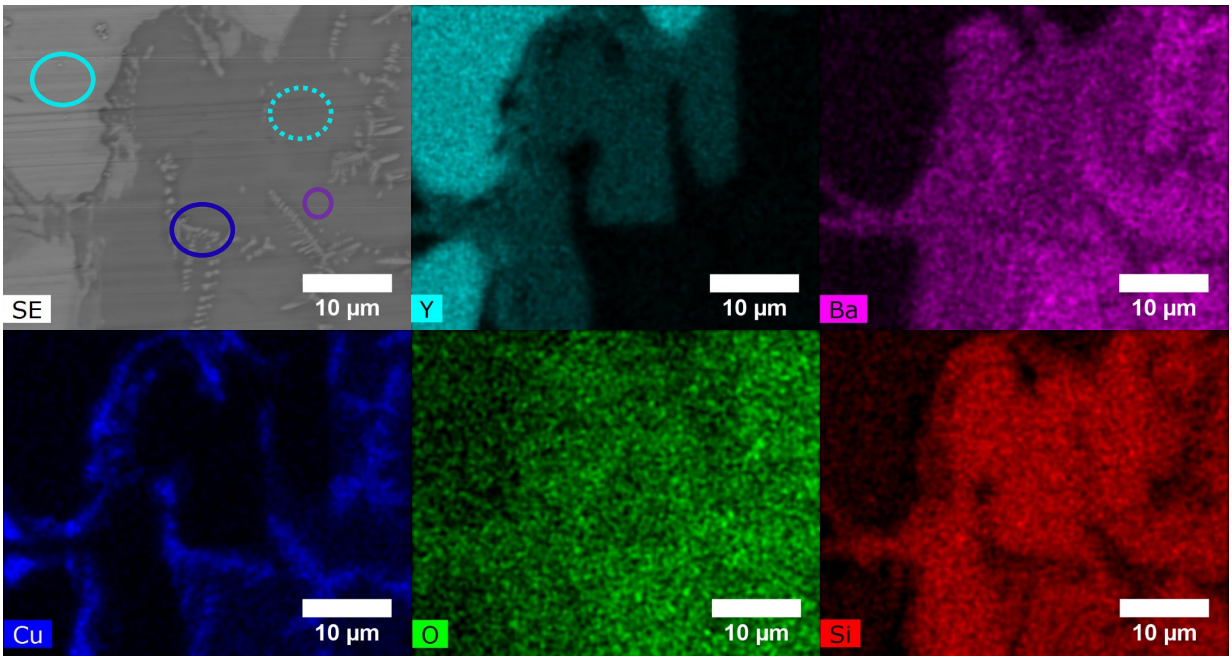

Figure 92: EDS mapping of the rapid thermally annealed YBCO/SiO_2 tube at 1100°C for 1h dwelling time with a subsequent quenching step

Table 23: EDS point analysis of the rapid thermally annealed YBCO/SiO_2 tube at 1100°C for 1h dwelling time with a subsequent quenching step, shown in atomic percent [at.-%]

	Y	Ba	Cu	O	Si	Main phases formed
	58.7	0.0	2.1	39.2	0.0	Y_2O_3
	14.1	9.8	2.6	52.2	21.3	$Y_2BaSi_3O_{10}$
	1.7	8.1	38.1	37.1	15.0	Cu_2O
	1.4	13.0	11.5	51.3	22.8	$BaCuSi_2O_6$

In order to further analyze the composition of the core, XRD analysis was performed on a small section of the core. The resulting XRD pattern is shown in black in Figure 93. The XRD pattern in blue is shown as a reference and is the pattern from the heat-treated YBCO glass fiber at 1100°C for a dwelling time of 10 min in air, shown in Section 3.1.6.1.

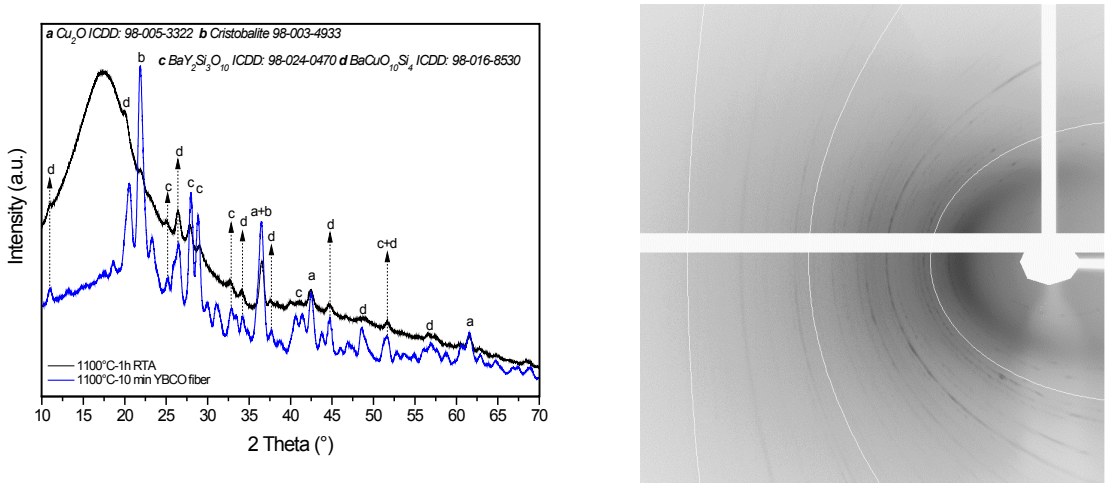

Figure 93: XRD patterns of the rapid thermally annealed YBCO/SiO_2 tube at 1100°C for 1h dwelling time with a subsequent quenching step (in black) and the heat-treated vacuum as-drawn YBCO fiber at 1100°C-10 min in air atmosphere as a reference (in blue) and the corresponding Debye-Scherrer diffraction ring pattern

As shown in Figure 93, the XRD pattern of the rapid thermally annealed sample shows a broad amorphous phase, which belongs to amorphous silica (originating from the fused silica tube). Hence, this indicates that the analyzed core piece was obtained from the interface region. It is, furthermore, visible in Figure 93 that cristobalite, cuprite, barium copper silicate and yttrium barium silicate reflection peaks are present. However, due to the strong amorphous background of the rapid thermally annealed YBCO/SiO_2 tube, no further quantitative results can be obtained. Moreover, the XRD analysis indicates the formation of $BaCuSi_4O_{10}$ instead of $BaCuSi_2O_6$, which is shown using EDS analysis in Table 23. Hence, it is highly possible that a mixed phase of barium copper silicates formed inside the core.

This analysis shows that the rapid thermal annealing experiments on YBCO powder inside a fused silica tube lead to stronger reactions as compared to the heat-treatments performed on YBCO powder/silica powder pellets in Section 3.2, which used defined slow heating and cooling rates. This highlights that the dissolution of the fused silica tube by the molten YBCO core, and the used heating rate, are key factors with regard to the rate of reaction between YBCO and silica.

We note that due to the small size of the YBCO core, the XRD analysis was performed on a Rigaku XtaLAB Synergy-S instrument using Cu-K_α radiation, following the same method used for performing the XRD analysis of the fiber core samples shown in Section 3.1.

3.3.4 *Summary*

This section has provided further analyses on the formation of phases within the YBCO-SiO_2 system based on a set of rapid thermal annealing experiments, with a subsequent quenching step, on YBCO+SiO_2 rods and on YBCO powder inside a fused silica tube. The experiments were conducted to further analyze the YBCO and silica reactions and to investigate the possibility of recrystallization of the superconductive Y-123 phase. The results shown in this section corroborated the results and conclusions drawn in Sections 3.1 and 3.2.

4 SUMMARY AND CONCLUSION

In this dissertation, we have investigated and determined the reaction processes between YBCO and SiO_2 at elevated temperatures within the YBCO glass fiber system as well as in YBCO powder+silica powder pellets and YBCO powder/fused silica tube samples, as illustrated in Figure 94. In this regard, this work enabled determining phase relations within the $YBa_2Cu_3O_{7-x}$-SiO_2 system and defining their impacts on potentially obtaining superconducting fibers. Furthermore, this work determined the effect of the silicon content on the superconductivity of YBCO at elevated temperatures.

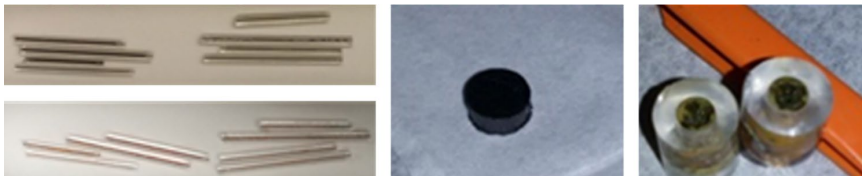

Figure 94: Illustration of the three main focus areas of this dissertation: reactions within YBCO glass fibers (left), reactions within YBCO+SiO_2 pellets (middle) and rapid thermal annealing experiments on YBCO-SiO_2 samples (right, showing a thermally annealed and quenched YBCO/SiO_2 tube)

4.1 Summary of main results

We have shown that during the YBCO glass fiber drawing process at the fiber draw tower, dissolution of the fused silica cladding into its Si^{4+} and O^{2-} ions occurs followed by a subsequent diffusion of Si^{4+} and O^{2-} inside the molten YBCO core. This leads to an amorphous silicate and amorphous silica-rich precipitations formation inside the core. In addition, we have shown that the dissolution of the fused silica cladding into its ions originates from lower eutectics, which form between yttria, copper oxide, barium oxide and silica and which reduce the overall softening point of fused silica. Moreover, we have shown that the dissolution is intensified due to the glass modifying properties of yttria, copper oxide and barium oxide, as we have thoroughly discussed in Section 3.1.2.

We have demonstrated that a miscibility gap exists within the glass-forming YBCO-SiO_2 system, which leads to the silica-rich precipitations formation. The region of the existing miscibility gap was identified based on the morphology of the YBCO core and the silica content inside the core. In this regard, the binodal and spinodal phase lines inside the miscibility gap were predicted as illustrated in Table 9.

In addition, we have shown that an increase in oxygen content, captured by drawing YBCO glass fibers in an oxygen-rich environment, increases the rate of the diffusion of silicon ions into the molten YBCO core, which shows that the O^{2-} ion diffusion is the rate-limiting step in this process. This, as a result, increases the silica-rich precipitations inside the core, as rigorously shown in Section 3.1.5. Moreover, we have proposed in Section 3.1.2 and confirmed in Section 3.3.3 that, due to the dissolution of the fused silica, no out-diffusion of the core material can be visible as the interface moves outwards with the dissolution of the cladding.

YBCO glass fibers were also drawn using a borosilicate preform in order to investigate the effect of the reduced drawing temperature on the dissolution and diffusion based reactions of YBCO and silica. In this regard, we have shown that, even though this leads to a lower silicon content inside the core, the dissolution and diffusion based reactions of the cladding material inside the molten YBCO core still occur. In addition, we have revealed that the YBCO core drawn with a borosilicate preform does not show any phase separation. This can be attributed to the lower silica content inside the core, as discussed in Section 3.1.5.

Furthermore, recrystallization heat-treatments were performed in air as well as in oxygen atmospheres on vacuum as-drawn YBCO fibers in order to investigate the possibility of restoring the superconductive Y-123 phase. The heat-treatments showed the formation of Cu_2O, cristobalite, yttrium barium silicate, as well as barium copper silicate. As such, these heat-treatments have indicated the infeasibility of restoring the superconductive Y-123 phase.

Additional analyses have been performed in this dissertation to further determine and analyze phase relations within the YBCO-SiO_2 system. In this regard, the analyses performed on YBCO+SiO_2 pellets in air and in oxygen atmospheres in Section 3.2 have shown that the increase in silica content leads to a gradual decomposition of the superconductive Y-123 phase and a gradual increase in the formation of a barium silicate phase. In addition, rapid thermal annealing experiments with a subsequent quenching step, discussed in Section 3.3, have demonstrated that the presence of a high silica content mixed with YBCO leads to phases comparable to those obtained in the YBCO fiber study, shown in Section 3.1. This, in turn, has corroborated our conclusion stating that the stable phases at elevated temperatures are yttrium barium silicate and barium copper silicate.

This dissertation has determined and analyzed the phase relations within the YBCO-SiO_2 system as well as the dissolution of the silica cladding into its ions and their subsequent diffusion inside the molten YBCO core, which prohibits the successful drawing of superconductive YBCO glass fibers using the molten-core approach. Chapter 5 will discuss alternative techniques and methods for potentially drawing superconductive YBCO fibers, providing a future outlook and paving the way for future research directions.

In general, the dissolution and diffusion based reactions between the silica cladding and the molten YBCO core are not solely relevant to the YBCO-SiO_2 system but are rather a common issue in drawing glass fibers using the molten-core approach. Hence, the understanding and identification of these reaction processes, arising when drawing glass-fibers using the molten-core approach, as thoroughly presented and investigated in this dissertation, extends the contribution of the current work beyond YBCO glass fibers. The key contributions of this work are summarized next, in Section 4.2.

4.2 Summary of key contributions

A summary of the key contributions to the body of literature in the field of YBCO and the YBCO-SiO_2 system, introduced in this dissertation, is provided next:

- First demonstration and evaluation of drawing YBCO glass fibers with a fused silica and borosilicate cladding using the molten-core approach on a fiber draw tower under vacuum and oxygen atmospheres. The obtained results revealed:
    - The inevitable occurrence of a dissolution of the fused silica cladding into Si^{4+} and O^{2-} ions and their subsequent diffusion into the molten YBCO core
    - The effect of the drawing temperature on the extent of the dissolution and diffusion based reactions, as shown by using borosilicate as the glass preform
    - The intensification of the co-diffusion of Si^{4+} and O^{2-} ions into the molten YBCO core in an oxygen atmosphere and that the diffusion of the O^{2-} ions is the rate-limiting step
- First discovery of a glass-forming YBCO-SiO_2 system
    - This work provided a novel and rigorous analysis of the phase separation mechanism in the YBCO-SiO_2 system

    - This work revealed the existence of a miscibility gap at high silica mole percentages
- Novel evaluation of a possible restoration/recrystallization of superconductive $YBa_2Cu_3O_{7-x}$ phase in as-drawn amorphous YBCO glass fibers
    - Determination of the effects of heat-treatments
    - Characterization of the effects of the fused silica cladding
- First experiments and results on the YBCO-SiO_2 system at elevated temperatures (above 1000°C)
    - Novel reaction products were identified such as yttrium barium silicate and barium copper silicate, and demonstrated to be the stable phases at elevated temperatures
- Development of a fundamental understanding of glass fibers manufactured using the molten-core approach, which is not solely limited to the YBCO-SiO_2 system, but is rather of direct relevance to general glass-clad manufacturing using the molten-core approach

5 FUTURE WORK

In this chapter, we explore future research directions focusing on potential approaches for drawing superconductive YBCO fibers as well as on further possible analyses of phase relations in the YBCO-SiO_2 system.

In order to investigate further possibilities of drawing superconductive YBCO fibers, high temperature stable barrier coatings within the preform design can be applied and tested. This would allow investigating whether the dissolution and diffusion based reaction processes between fused silica and YBCO can be mitigated. The work in [109] describes a method in which a CaO barrier coating is used for silicon core fibers in order to reduce the oxygen content inside the silicon core. However, in general, as shown in this dissertation, YBCO is highly reactive, especially at high temperatures. For instance, YBCO can corrode platinum at high temperatures as reported in [72, 110, 111]. Hence, finding an effective barrier coating at such high temperatures is highly challenging. Therefore, another approach, which can be investigated, consists in using a laser-heated pedestal growth (LHPG) system to draw YBCO fibers from the molten YBCO state. The works in [112-114] have shown that it is possible to draw superconductive YBCO wires using laser floating zone melting. Furthermore, it was shown in [115] that, using the LHPG system, long lengths of sapphire fibers can be theoretically achieved. As such, this highlights the possibility of applying a similar process for drawing YBCO fibers. However, in general, pulled YBCO fibers would need to be heat-treated in order to regain their superconductive Y-123 phase after the melting process. This, hence, constitutes an additional challenge facing the process of pulling YBCO fibers using the LHPG system. However, possible ways to address this challenge could consist of installing an in-situ furnace unit with a thermal temperature gradient, which allows reducing the quenching rate of the pulled fiber, potentially allowing a recrystallization of the Y-123 phase. On the other hand, pulling YBCO fibers using the LHPG system faces an additional challenge stemming from the need for a protective coating to stabilize the pulled YBCO fiber chemically and mechanically. To this end, coating materials, which are stable up to the recrystallization temperature of the Y-123 phase, would be needed. In this regard, using a sol-gel dip-coating, which could be incorporated into the drawing process, could provide a useful approach to address this challenge.

In order to obtain a further understanding of the complex phase diagram of the YBCO-SiO_2 system, rapid thermal annealing methods would need to be performed on YBCO and fused silica at temperatures up to 2000°C. The most critical challenge is to find an appropriate glass-melting crucible, which would not be corroded by the YBCO. In general, platinum crucibles are used for glass melting. However, as discussed earlier in this chapter, YBCO corrodes platinum at elevated temperatures [72, 110, 111]. This further highlights the challenges in determining the thermodynamically stable phases of the YBCO-SiO_2 system at temperatures above 1000°C. Potential approaches to mitigate these challenges could include crucible-free heat-treatments using the aerodynamic levitation method [116, 117].

In summary, these two research directions remain challenging due to the strong reactivity of the YBCO compounds. Therefore, crucible free methods could introduce key advantages, which would allow advancing the research on YBCO at elevated temperatures. For instance, using the LHPG system to pull YBCO fibers could constitute the next step towards achieving commercially applicable long-scale superconductive YBCO fibers.

BIBLIOGRAPHY

1. Wu MK, Ashburn JR, Torng CJ, Hor PH, Meng RL, Gao L, et al. Superconductivity at 93 K in a new mixed-phase Y-Ba-Cu-O compound system at ambient pressure. Physical Review Letters. 1987;58(9):908-910.

2. Rupich MW, Li X, Thieme C, Sathyamurthy S, Fleshler S, Tucker D, et al. Advances in second generation high temperature superconducting wire manufacturing and R&D at American Superconductor Corporation. Superconductor Science and Technology. 2010;23(1):014015.

3. Goyal A, Paranthaman MP, Schoop U. The RABiTS Approach: Using Rolling-Assisted Biaxially Textured Substrates for High-Performance YBCO Superconductors. MRS Bulletin. 2011;29(08):552-561.

4. Homa D, Liang Y, Pickrell G. High-Temperature Superconducting Fiber. Journal of Superconductivity and Novel Magnetism. 2014;27(4):891-895.

5. Homa D, Liang Y, Pickrell G. Superconducting fiber. Applied Physics Letters. 2013;103(8):082601.

6. Homa D, Pickrell G, Kaur G. On the verge of high temperature superconducting fibers. Materials Letters. 2014;121:101-104.

7. Homa D, Liang Y, Hill C, Kaur G, Pickrell G. Superconducting tin core fiber. Applied Physics A. 2014;118(1):23-26.

8. Yan MF, Rhodes WW, Gallagher PK. Dopant effects on the superconductivity of $YBa_2Cu_3O_7$ ceramics. Journal of Applied Physics. 1988;63(3):821-828.

9. Fagan JG, Amarakoon VRW, Richmond-Hope J. The effects of impurity oxides on $YBa_2Cu_3O_{7-x}$ microstructure development. Physica C. 1994;225:240-252.

10. Komatsu T, Tanaka O, Matusita K, Takata M, Yamashita T. On the Reactions of Quenched BaYCuO Powders with Various Materials. Japanese Journal of Applied Physics. 1988;27(6):L1025-L1028.

11. Koinuma H, Fukuda K, Hashimoto T, Fueki K. Chemical Interaction between $Ba_2YCu_3O_{7-\delta}$ and Substrate Materials in the Solid State. Japanese Journal of Applied Physics. 1988;27:L1216-L1218.

12. Qiu CX, Shih I. Some properties of bulk Y‐Ba‐Cu‐O compounds containing SiO_2. Journal of Applied Physics. 1988;64(4):2234-2236.

13. Grigorov KG, Grigorov GI, Stoyanova MV, Chakalov RA, Vignes J-L, Langeron J-P, et al. Interdiffusion of Y-Ba-Cu oxides and SiO_2 substrate. Efficiency of titanium nitride barrier film. Vacuum. 1993;44:1119-1121.
14. Nakajima H, Yamaguchi S, Iwasaki K, Morita H, Fujimori H, Fujino Y. Interdiffusion and interfacial reaction between an YBa_2Cu3O_x thin film and substrates. Applied Physics Letters. 1988;53(15):1437-1439.
15. Li B, Williams ED. Stability of the $YBa_2Cu_3O_{7-x}$−Si interface. Journal of Materials Research. 1991;6(08):1634-1640.
16. Ziegler C, Frank G, Goepel W. Interface Properties of Thin $YBa_2Cu_30_{7-x}$ Films. Berichte der Bunsengesellschaft für physikalische Chemie. 1991;95:1404-1409.
17. Ziegler C, Frank G, Goepel W, editors. Passivation Layers on $YBa_2Cu_3O_{7-x}$ Thin Films. International Conference on Advanced Materials - ICAM 91; 1992; Straßbourg: North-Holland, Elsevier Science Publishers B.V.; 1992.
18. Ma QY, Yang ES, Chang CA. Rapid thermal annealing of YBaCuO thin films deposited on SiO_2 substrates. Journal of Applied Physics. 1989;66(4):1866-1868.
19. Taylor GF. A Method of Drawing Metallic Filaments and a Discussion of their Properties and Uses. Physical Review. 1924;23(5):655-660.
20. Grodkiewicz W. Fused silica fibers with metal cores. Materials Research Bulletin. 1975;10(10):1085-1090.
21. Morris S, Ballato J. Molten-core fabrication of novel optical fibers. American Ceramic Society Bulletin. 2013;92(4):24-29.
22. Ballato J, Hawkins T, Foy P, Kokuoz B, Stolen R, McMillen C, et al. On the fabrication of all-glass optical fibers from crystals. Journal of Applied Physics. 2009;105(5):053110.
23. Zheng S, Li J, Yu C, Zhou Q, Chen D. Preparation and characterizations of Nd:YAG ceramic derived silica fibers drawn by post-feeding molten core approach. Optics Express. 2016;24(21):24248-24254.
24. Auguste JL, Humbert G, Leparmentier S, Kudinova M, Martin PO, Delaizir G, et al. Modified Powder-in-Tube Technique Based on the Consolidation Processing of Powder Materials for Fabricating Specialty Optical Fibers. Materials (Basel). 2014;7(8):6045-6063.
25. Siegfried H. Festkörperphysik. 3 ed. München: Oldenbourg Verlag München; 2011.

26. Kleiner R, Buckel W. Superconductivity: an introduction. Weinheim: Wiley-VCH Verlag GmbH & Co. KGaA; 2016.
27. Meißner W, Ochsenfeld R. Ein neuer Effekt bei Eintritt der Supraleitfähigkeit. Naturwissenschaften. 1933;21(44):787.
28. Werfel FN, Floegel-Delor U, Rothfeld R, Riedel T, Goebel B, Wippich D, et al. Superconductor bearings, flywheels and transportation. Superconductor Science and Technology. 2012;25(1):014007.
29. Enss C, Hunklinger S. Low-Temperature Physics. Heidelberg: Springer 2005.
30. Kittel C. Introduction to Solid State Physics. 8th ed. Hoboken, NJ: Wiley; 2005.
31. Larbalestier DC, Jiang J, Trociewitz UP, Kametani F, Scheuerlein C, Dalban-Canassy M, et al. Isotropic round-wire multifilament cuprate superconductor for generation of magnetic fields above 30 T. Nat Mater. 2014;13(4):375-381.
32. Hernandez-Llambes JC, Hazelton D. Advantages of Second-Generation High Temperature Superconductors for Pulsed Power Applications. 2009 IEEE Pulsed Power Conference; Washington, DC, USA: IEEE; 2009.
33. Shiohara Z, Endo A. Crystal growth of bulk high T_c superconducting oxide materials. Materials Science and Engineering. 1997;R19:1-86.
34. Jianqing F, Yafeng L, Lian Z, Pingxiang Z, Xiaoyan X, Shaokai C, et al. The phase conversion of precursor powders for powder melting process $YBa_2Cu_3O_{7-x}$ superconductors. Journal of Materials Science: Materials in Electronics. 2008;19(11):1069-1072.
35. Bourdillon A, Bourdillon NXT. High Temperature Superconductors: Processing and Science. New York: Academic Press, Inc.; 1994.
36. Lay KW, Renlund GM. Oxygen Pressure Effect on the Y_20_3-BaO-CuO Liquidus. Journal of the American Ceramic Society. 1990;73(5):1208-12013.
37. Aselage TL. Occurrence of free CuO in $YBa_2Cu_3O_{6+\delta}$ and its effect on melting and solidification Physica A. 1994;233:292-300.
38. Eickemeyer J, Hühne R, Güth A, Rodig C, Gaitzsch U, Freudenberger J, et al. Textured Ni–9.0 at.% W substrate tapes for YBCO-coated conductors. Superconductor Science and Technology. 2010;23(8).
39. Solovyov V, Farrell P. Exfoliated YBCO filaments for second-generation superconducting cable. Superconductor Science and Technology. 2017;30(1).

40. Heaney PJ, Prewitt CT, Gibbs GV. Silica: Physical Behavior, Geochemistry and Materials Applications. Ribbe PH, editor. Washington D.C.: Mineralogical Society of America; 1994.
41. Exarhos GJ, Gruzdev VE, Menapace JA, Ristau D, Soileau MJ, Nürnberg F, et al. Metrology of fused silica. Laser-Induced Damage in Optical Materials 20162016.
42. Koike C, Noguchi R, Chihara H, Suto H, Ohtaka O, Imai Y, et al. Infrared Spectra of Silica Polymorphs and the Conditions of Their Formation. The Astrophysical Journal. 2013;778(1).
43. Hummels FA. Introduction to phase equilibria in ceramic systems. New York: M.Dekker; 1915.
44. Jaeger RE. Fiber Drawing Process: Characterization and Control. In: Bernard Bendow SSM, editor. Fiber Optics Advances in Research and Development. New York: Springer; 1979.
45. Morris S, Hawkins T, Foy P, Ballato J, Martin SW, Rice R. Cladding Glass Development for Semiconductor Core Optical Fibers. International Journal of Applied Glass Science. 2012;3(2):144-153.
46. Ballato J, Hawkins T, Foy P, Stolen R, Kokuoz B, Ellison M, et al. Silicon optical fiber. Optics Express. 2008;16(23):18675-18683.
47. Ballato J, McMillen C, Hawkins T, Foy P, Stolen R, Rice R, et al. Reactive molten core fabrication of glass-clad amorphous and crystalline oxide optical fibers. Optical Materials Express. 2012;2(2):153-160.
48. Ballato J, Hawkins T, Foy P, Yazgan-Kokuoz B, McMillen C, Burka L, et al. Advancements in semiconductor core optical fiber. Optical Fiber Technology. 2010;16(6):399-408.
49. Morris S, Hawkins T, Foy P, Hudson J, Zhu L, Stolen R, et al. On loss in silicon core optical fibers. Optical Materials Express. 2012;2(11):1511-1519.
50. James PF. Liquid-phase separation in glass-forming systems. Journal of Materials Science. 1975;10 1802-1825.
51. Seward TP, Uhlmann DR, Turnbull D. Phase Separation in the System BaO-SiO_2. Journal of the American Ceramic Society. 1968;51(5):278-285.
52. Seward TP, Uhlmann DR, Turnbull D. Development of Two-Phase Structure in Glasses, with Special Reference to the System BaO-SiO_2. Journal of the American Ceramic Society. 1968;51(11):634-643.

53. Gueguen Y, Houizot P, Célarié F, Chen M, Hirata A, Tan Y, et al. Structure and viscosity of phase-separated BaO-SiO_2 glasses. Journal of the American Ceramic Society. 2017;100(5):1982-1993.
54. Haller W. Rearrangement Kinetics of the Liquid—Liquid Immiscible Microphases in Alkali Borosilicate Melts. Journal of Chemical Physics. 1965;42(2):686-693.
55. James PF, McMillan PW. Quantitative measurements of phase separation in glasses using transmission electron microscopy. Part 2. A study of lithia-silica glasses and the influence of phosphorus pentoxide. Physics and Chemistry of Glasses. 1970;11(3):64-70.
56. Gadalla AMM, Ford WF, White J. Equilibrium Relationships in the System CuO-Cu_2O-SiO_2. Transactions of the British Ceramic Society. 1963;62:45-66.
57. Toropov NA, Bondar IA. Silicates of the rare earth elements. Bulletin of the Academy of Sciences of the USSR Division of chemical science. 1961;10(4):502-508.
58. Hageman VBM, Oonk HAJ. Liquid immiscibility in the SiO_2+MgO, SiO_2 +SrO, SiO_2+L_2O_3, and SiO_2+Y_2O_3 systems. Physics and Chemistry of Glasses. 1986;27(5):194-198.
59. Borghesi A, Pivac B, Sassella A, Stella A. Oxygen precipitation in silicon. Journal of Applied Physics. 1995;77(9):4169-4244.
60. Hu SM. Effects of ambients on oxygen precipitation in silicon. Applied Physics Letters. 1980;36(7):561-564.
61. Pagani M, Falster RJ, Fisher GR, Ferrero GC, Olmo M. Spatial variations in oxygen precipitation in silicon after high temperature rapid thermal annealing. Applied Physics Letters. 1997;70(12):1572-1574.
62. Hawkins GA, Lavine JP. The effect of rapid thermal annealing on the precipitation of oxygen in silicon. Journal of Applied Physics. 1989;65(9):3644-3654.
63. Vanhellemont J. Diffusion limited oxygen precipitation in silicon: Precipitate growth kinetics and phase formation. Journal of Applied Physics. 1995;78(6):4297-4299.
64. Gösele U, Tan TY. Oxygen Diffusion and Thermal Donor Formation in Silicon. Applied Physics A. 1982;28:79-92.
65. Liang Y. Fabrication and Characterization of Superconducting Core Fibers with Fused Silica Cladding. Blacksburg: Virginia Tech; 2014.
66. Aselage T, Keefer K. Liquidus relations in Y–Ba–Cu oxides. Journal of Materials Research. 1988;3(06):1279-1291.

67. Salem MKB, Hannachi E, Slimani Y, Hamrita A, Bessais L, Azzouz FB, et al. Effect of nanowires SiO_2 on superconducting properties of $YBa_2Cu_3O_{7-d}$ bulks. 2013. p. 73-76.
68. Ben Salem MK, Almessiere MA, Al-Otaibi AL, Ben Salem M, Ben Azzouz F. Effect of SiO_2 nano-particles and nano-wires on microstructure and pinning properties of $YBa_2Cu_3O_{7-d}$. Journal of Alloys and Compounds. 2016;657:286-295.
69. Gupta A, Deshpande AJ, Awana VPS, Balamurugan S, Sood KN, Kishore R, et al. Flux line motion in superconducting $(YBa_2Cu_3O_{7-d})_{1-x}/(SiO_2)_x$ composite systems in high magnetic fields. Superconductor Science and Technology. 2007;20(10):1084-1091.
70. Ben Salem MK, Hannachi E, Slimani Y, Hamrita A, Zouaoui M, Bessais L, et al. SiO_2 nanoparticles addition effect on microstructure and pinning properties in $YBa_2Cu_3O_y$. Ceramics International. 2014;40(3):4953-4962.
71. Murakami M, Morita M, Doi K, Miyamoto K, Hamada H. Microstructural Study of the Y-Ba-Cu-O System at High Temperatures. Journal of Applied Physics. 1989;28(3):L399-L401.
72. Murakami M. Melt processed high-temperature superconductors. Murakami M, editor. Singapur: World Scientific Publishing Co Pte Ltd; 1992.
73. Kim NK, Drozdyk L, Payne DA, Friedmann TA, Wright WH, Ginsberg DM. Preparation, Crystallization and Properties of Rapidly Solidified $YBa_2Cu_30_{7-delta}$. Materials Letters. 1987;5(10):387-390.
74. Komatsu T, Imai K, Matusita K, Ishii M, Takata M, Yamashita T. Crystalline Phases in Superconductor Ba-Y-Cu-O with High T_c Prepared by Melting Method. Japanese Journal of Applied Physics. 1987;26(8):L1272-L1273.
75. McKittrick J, Sasayama S, McHenry ME, Kalonji G, O'Handley RC. Melting and solidification behavior of $YBa_2Cu_3O_{7-x}$. Journal of Applied Physics. 1989;65(9):3662-3666.
76. Cupid DM, Seifert HJ. Thermodynamic Calculations and Phase Stabilities in the Y-Si-C-O System. Journal of Phase Equilibria and Diffusion. 2007;28(1):90-100.
77. Williams RS, Chaudhury S. Chemical Compatibility of High-T_c Superconductors with Other Materials. California Univ., Los Angeles. Dept. of Chemistry.: Office of Naval Research; 1988.
78. Xia L, Liu Z, Taskinen PA. Equilibrium study of the Cu–O–SiO_2 system at various oxygen partial pressures. Journal of Chemical Thermodynamics. 2016;98:126-134.
79. Lambert U, Eysel W. New Copper (II)-Rare Earth (III) Compounds I. Ternary Systems CuO-M_2O_3-TO_2. Powder Diffraction. 1986;1(2):45-50.

80. Dickinson CF, Heal GR. Solid-liquid diffusion controlled rate equations. Thermochimica Acta. 1999;340-341:89-103.
81. Joo J, Singh JP, Warzynski T, A. G, Poeppel RB. Role of Silver Addition on Mechanical and Superconducting Properties of High-T_c Superconductors. Applied Superconductivity. 1994;2(6):401-410.
82. Congreve JVJ, Shi Y, Dennis AR, Durrell JH, Cardwell DA. The successful incorporation of Ag into single grain, Y–Ba–Cu–O bulk superconductors. Superconductor Science and Technology. 2018;31(3).
83. Sheahen TP. Introduction to High-Temperature Superconductivity. Wolf S, editor. New York: Plenum Press; 1994.
84. CrysAlisPro Software System. v1.171.40.53 ed. Oxford, UK: Rigaku Corporation; 2019.
85. Ziegler C, Baudenbacher F, Karl H, Kinder H, Goepel W. Interface analysis of the system Si/$YBa_2Cu_aO_{7-x}$. Fresenius Journal of Analytical Chemistry. 1991;341:308-313.
86. Kominsky D. Development of Random Hole Optical Fiber and Crucible Technique Optical Fibers [Dissertation]. Blacksburg: Virginia Polytechnic Institute and State University; 2005.
87. Frantz JD, Mysen BO. Raman spectra and structure of BaO-SiO_2, SrO-SiO_2 and CaO-SiO_2 melts to 1600°C. Chemical Geology. 1995;121:155-176.
88. Mao Y, He J, Sun X, Li W, Lu X, Gan J, et al. Electrochemical synthesis of hierarchical Cu_2O stars with enhanced photoelectrochemical properties. Electrochimica Acta. 2012;62:1-7.
89. Sander T, Reindl CT, Giar M, Eifert B, Heinemann M, Heiliger C, et al. Correlation of intrinsic point defects and the Raman modes of cuprous oxide. Physical Review B. 2014;90(4).
90. Simo A, Polte J, Pfander N, Vainio U, Emmerling F, Rademann K. Formation mechanism of silver nanoparticles stabilized in glassy matrices. Journal of the American Chemical Society. 2012;134(45):18824-18833.
91. Abe Y, Hosono H, Lee WH, Kasuga T. Superconducting ceramics of $Bi_2Sr_2Ca_1Cu_2O_x$ prepared by heating in a vacuum-sealed vessel. Applied Physics Letters. 1992;60(18):2300-2302.
92. Jung I-H, Decterov SA, Pelton AD. Critical Thermodynamic Evaluation and Optimization of the MgO-Al_2O_3, CaO-MgO-Al_2O_3, and MgO-Al_2O_3-SiO_2 Systems. Journal of Phase Equilibria & Diffusion. 2004;25(4):329-345.
93. Burnett DG, Douglas RW. Liquid-liquid phase separation in the soda-lime-silica system. Physics and Chemistry of Glasses. 1970;11(5):125-135.

94. Mao H, Selleby M, Fabrichnaya O. Thermodynamic reassessment of the Y_2O_3–Al_2O_3–SiO_2 system and its subsystems. Calphad-Computer Coupling of Phase Diagrams and Thermochemistry. 2008;32(2):399-412.
95. Zheng H, Colby MW, Mackenzie JD. Control and effects of Cu(I) and Cu(II) ions in Bi-Ca-Sr-Cu-0 glasses. Journal of Non-Crystalline Solids. 1991;127:143-150.
96. Sato R, Komatsu T, Kuken Y, Matusita K, Sawada K, Hiraoka M. Effect of Cu^+/Cu^{2+} ratio on the thermal stability and crystallization in $Bi_2Sr_2CaCu_2O_x$ glass. Journal of Non Crystalline Solids. 1993;152:150-156.
97. Sato R, Komatsu T, Matusita K. Effect of Cu^+ content on properties of $Bi_2Sr_2CaCu_2O_x$ glass. Journal of Non Crystalline Solids. 1993;160:180-182.
98. Komatsu T, Matusita K. High-T_C superconducting glass-ceramics. Thermochimica Acta. 1991;174:131-151.
99. Khaled J, Watanabe R, Sato R, Komatsu T. Implications of Cu valence on the structure of Bi-based superconducting precursor glasses. Journal of Non Crystalline Solids. 1997;222:175-181.
100. Sato R, Komatsu T, Matusita K. Crystallization mechanism in $Bi_2Sr_2CuO_x$ glass. Journal of Non Crystalline Solids. 1991;134:270-276.
101. De Guile MR, Bansal NP, Kim CJ. Superconducting Glass-Ceramics in the Bi-Sr-Ca-Cu-O System. Journal of American Ceramic Society. 1990;73(5):1165-1171.
102. Liu Z, Carlberg T. Reactions between liquid silicon and vitreous silica. Journal of Materials Research. 1991;7(02):352-358.
103. Berke H. The invention of blue and purple pigments in ancient times. Chemical Society Reviews. 2007;36(1):15-30.
104. Hoff HA, Rubinstein M, Osofsky MS, Singh AK, Richards LE, Lechter WL, et al. Color Indicator of Cuprate Superconductivity Observed by Polarized Light Microscopy. Journal of Superconductivity. 1989;2(3):351-359.
105. Hoff HA, Singh AK, Wallace JS, Lechter WL, Pande CS. Optical Differentiation of Orthorhombic Superconductors such as $YBa_2Cu_3O_7$ from Their Tetragonal Precursor Material. Journal of Superconductivity. 1988;1(1):35-44.
106. Schmid H, Burkhardt E, Walker E, Brixe W, Clin M, Rivera J-P, et al. Polarized light and X-ray precession study of the ferroelastic domains of $YBa_2Cu_3O_{7-\delta}$. Zeitschrift fur Physik B: Condensed Matter. 1988;72:305-322.

107. Hoff HA, Osofsky MS, Lechter WL, Pande CS, editors. The color of polarization in cuprate superconductors. Advances in Materials Science and Applications of High Temperature Superconductors; 1990 Jan 01,1991; NASA Goddard Space Flight Center: United States; 1990.
108. Hoff HA, Lechter WL, Osofsky MS, Candela GA. Microanalysis of Cuprate Superconductors Using the Color of Polarization. MRS Proceedings. 2011;169:361-364.
109. Nordstrand EF, Dibbs AN, Eraker AJ, Gibson UJ. Alkaline oxide interface modifiers for silicon fiber production. Optical Materials Express. 2013;3(5).
110. Calestani G, Rizzoli C, Andreetti GD. Synthesis and crystal structure of $Y_2Ba_3Cu_2PtO_{10}$. Solid State Communications. 1988;66(2):223-226.
111. Scheel HJ, Licci F. Crystal growth of $YBa_2Cu_3O_{7-x}$. Journal of Crystal Growth. 1987;85(4):607-614.
112. Jiang M, Huang JG, Wang YZ, Zhang C, Zeng DC, Wang X, et al. Solidification characteristics of textured 123 phase in YBCO by laser floating zone leveling (LFZL) method. Journal of Crystal Growth. 1993;130:289-393.
113. Sun JZ, Feigelson RS, Gazit D, Fork D, Geballe TH, Kapitulnik A. Properties of High-T_c Oxide Fibers from Laser Heated Pedestal Growth. IEEE Transactions on Magnetics. 1989;25(2):2014-2016.
114. Jiang XP, Huang JG, Yut Y, Jiang M, Qiao GW, Ge YL, et al. The crystal growth of Y-Ba-Cu-O by laser floating zone melting. Superconductor Science and Technology. 1988;1:102-106.
115. Liu B, Yu Y, Bera S, Buric MP, Chorpening B, Ohodnicki PR, et al. Study of molten zone profile and defect formation during laser heated pedestal growth. Micro- and Nanotechnology Sensors, Systems, and Applications XI2019.
116. Pack A, Kremer K, Albrecht N, Simon K, Kronz A. Description of an aerodynamic levitation apparatus with applications in Earth sciences. Geochemical Transactions. 2010;11:4.
117. Benmore CJ, Weber JKR. Aerodynamic levitation, supercooled liquids and glass formation. Advances in Physics: X. 2017;2(3):717-736.

APPENDIX

Appendix A: EDS line-scan of as-drawn YBCO+15 wt.-% Ag_2O borosilicate fiber core of partial molten core material

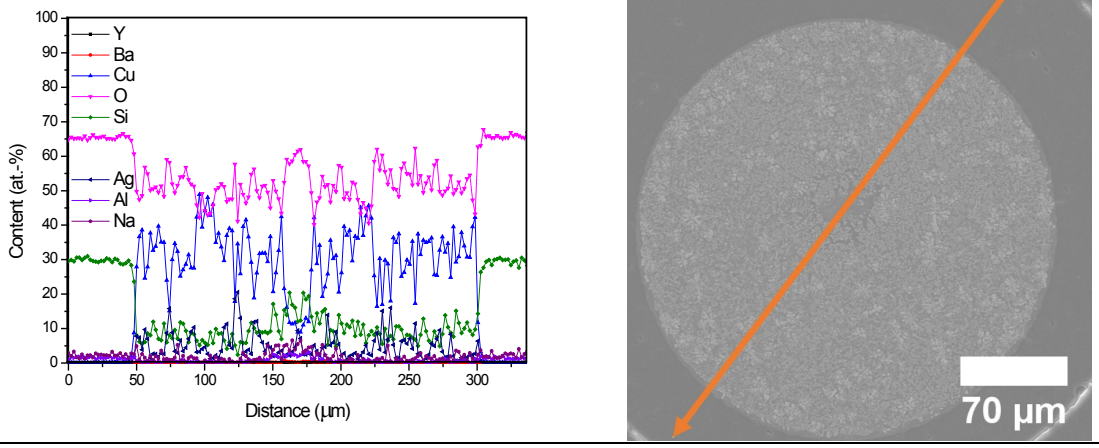

Appendix B: EDS mappings of YBCO/SiO_2 pellets heat-treated between 900°C and 1200°C for 30 min dwelling time in air

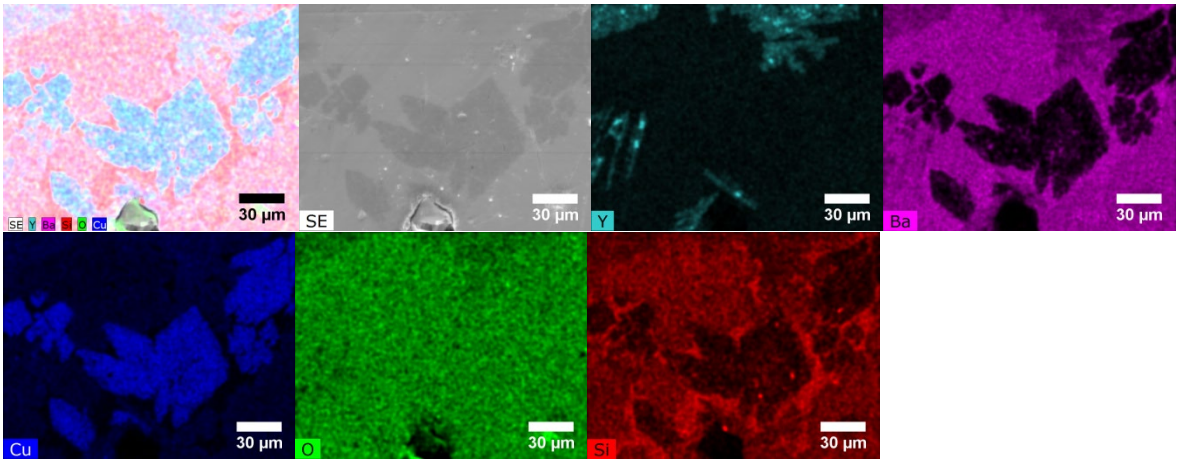

1100°C-30 min 20 at.-% SiO_2

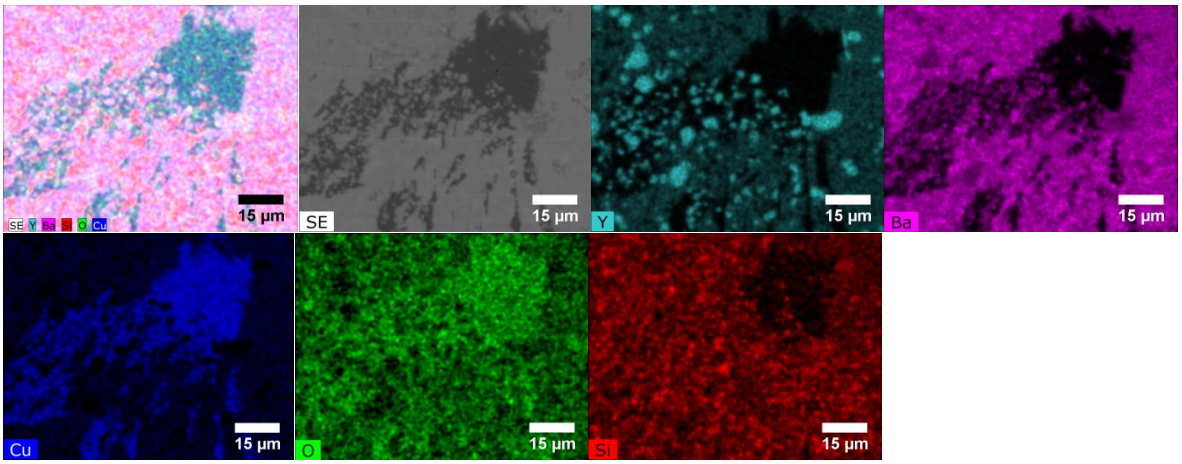

1200°C-30 min 20 at.-% SiO_2

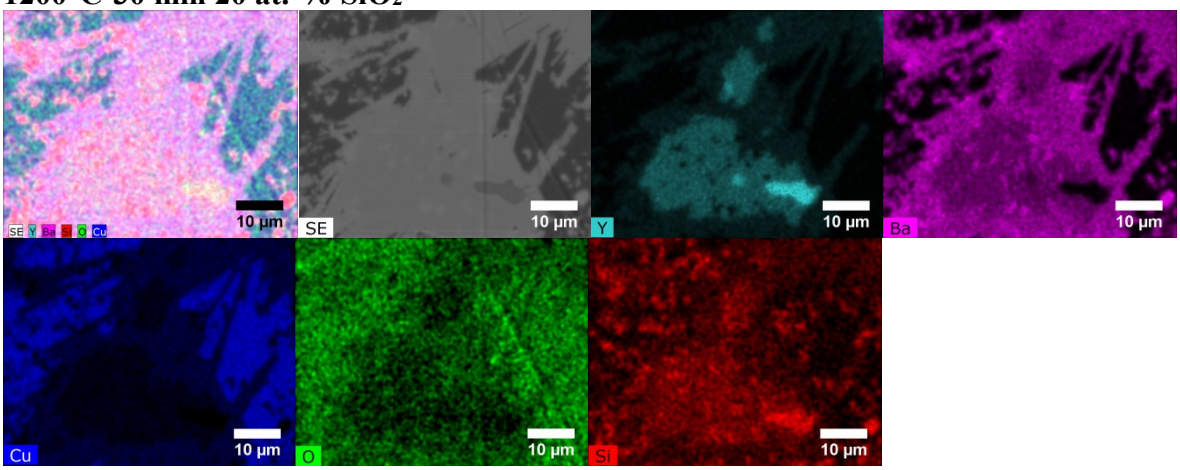

900°C-30 min 33.33 at.-% SiO_2

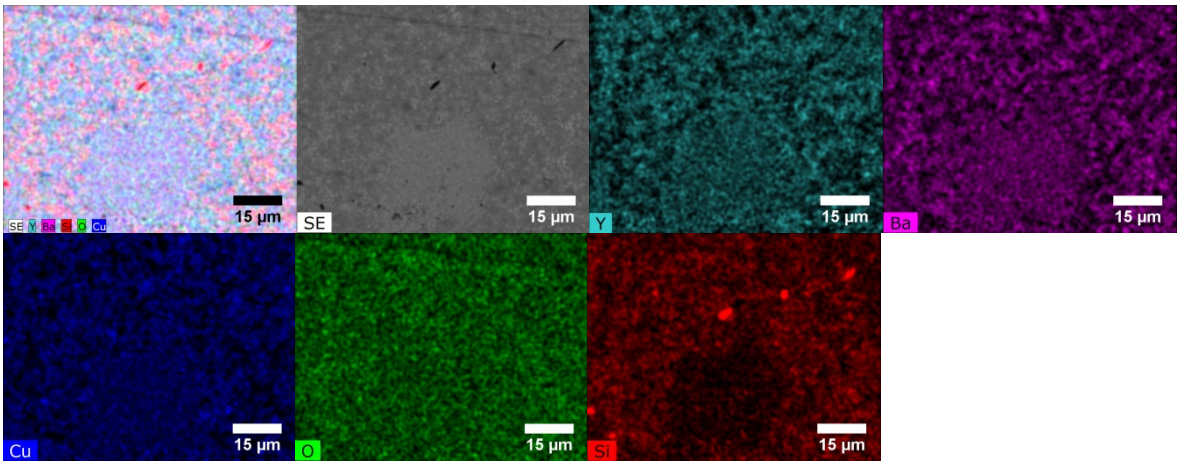

1000°C-30 min 33.33 at.-% SiO_2

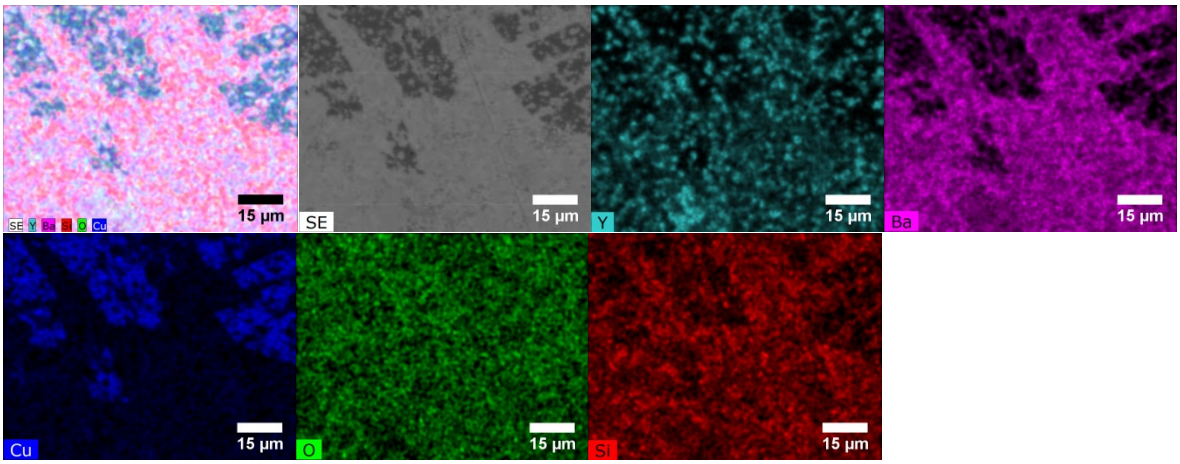

1100°C-30 min 33.33 at.-% SiO_2

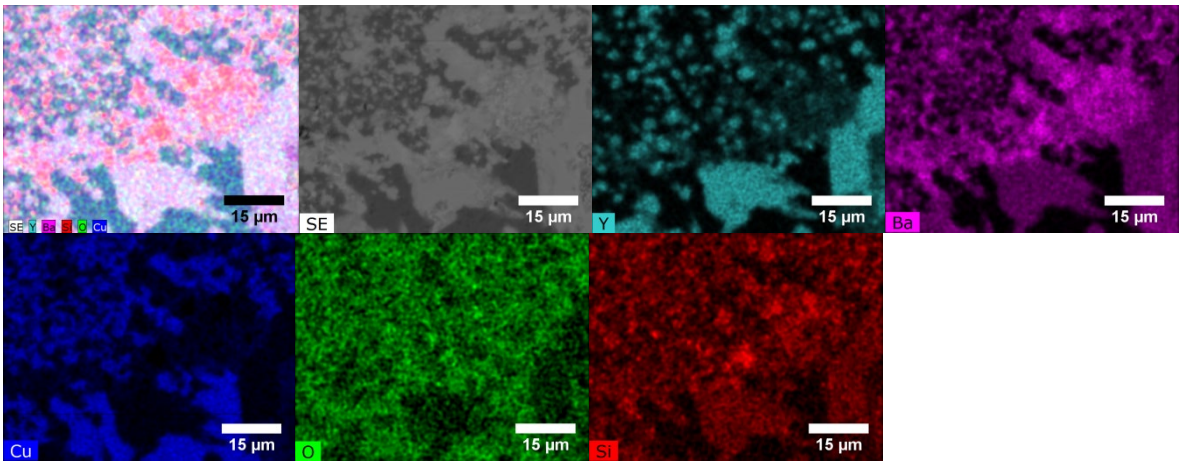

1200°C-30 min 33.33 at.-% SiO_2

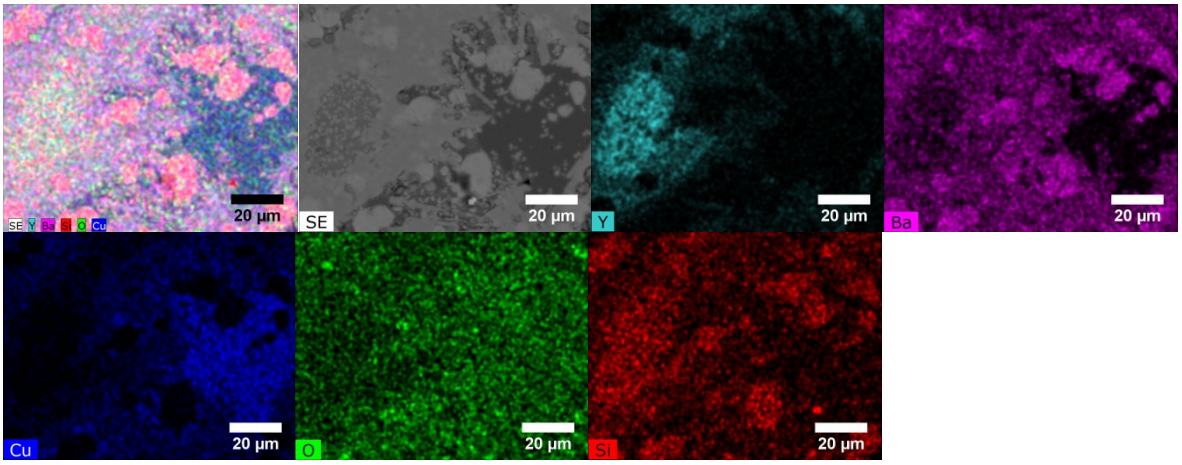

900°C-30 min 50 at.-% SiO_2

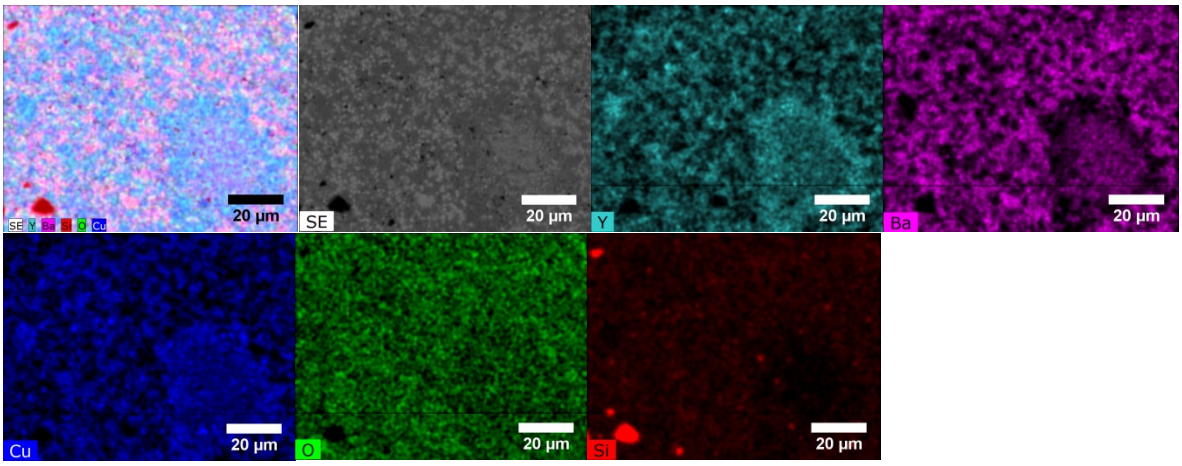

1000°C-30 min 50 at.-% SiO_2

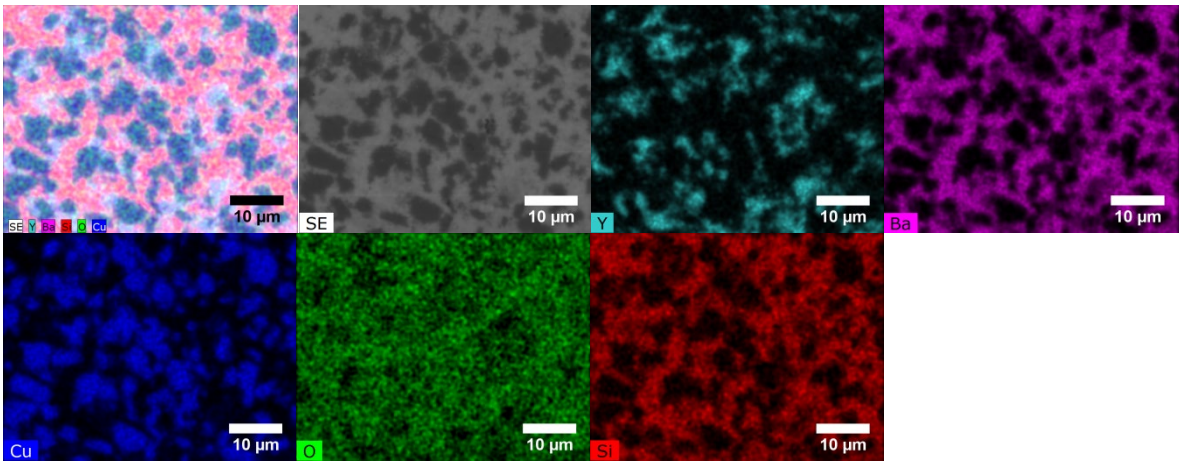

1100°C-30 min 50 at.-% SiO_2

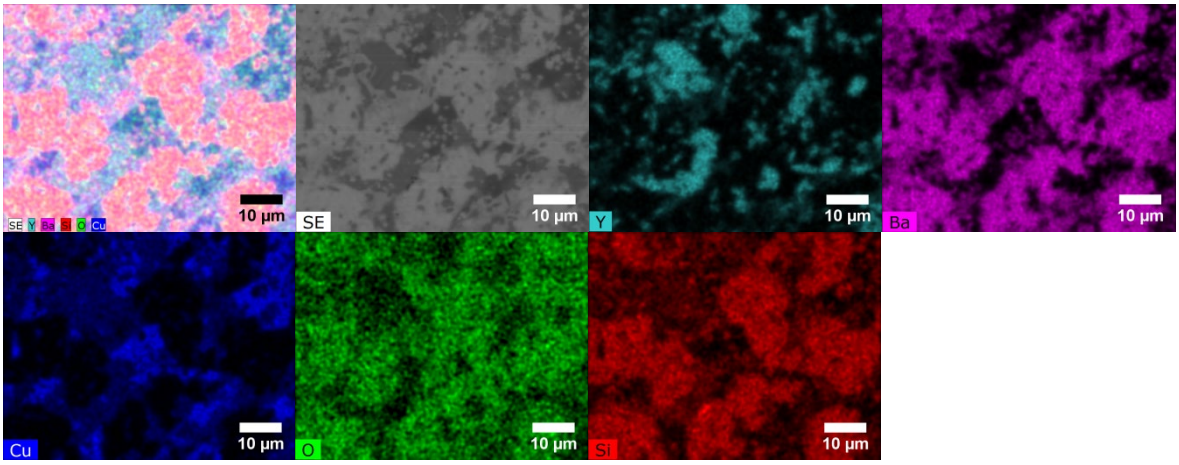

1200°C-30 min 50 at.-% SiO_2